OPTICAL REFLECTIVITY AND AUGER SPECTROSCOPY OF TITANIUM AND TITANIUM-OXYGEN SURFACES

A THESIS
Presented to
The Faculty of the Division of Graduate Studies
By
William Edgar Wall, Jr.

In Partial Fulfillment
of the Requirements for the Degree
Doctor of Philosophy
in the School of Physics

Georgia Institute of Technology
August 1978

OPTICAL REFLECTIVITY AND AUGER SPECTROSCOPY OF TITANIUM AND TITANIUM-OXYGEN SURFACES

Approved:

James R. Stevenson, Chairman

Uzi Landman

Edwin J. Scheibner

Date Approved by Chairman 8/28/78

ACKNOWLEDGMENTS

During the course of this work, a number of people have made valuable contributions that the author wishes to acknowledge. Dr. James R. Stevenson, who served as Thesis Advisor, provided valuable discussions and, through his considerable experience, important insights into many of the experimental problems encountered. Dr. M. W. Ribarsky aided in the analysis of the data and also was involved in valuable discussions along with Dr. K. O. Legg, who provided his expertise in experimental surface physics. James W. Larsen worked with the author in the construction of some of the apparatus and in making many of the early measurements. Bruce Biskey and Samuel Formby aided in the design and construction of the computer interfaces. Dr. I. R. Gatland developed the optical analysis computer program, and Ronald Yanda performed many of the computations. Ms. Kathy Massett expertly typed the final manuscript. To these people the author expresses his deep graditude.

However, above all the author wishes to thank his wife, Laura, for her support and encouragement which made this work possible, and for her assistance in the preparation of the manuscript and illustrations.

The author also wishes to acknowledge the Air Force Office of Scientific Research and the Energy Research and Development Administration for their financial support.

TABLE OF CONTENTS

LIST OF TABLES

LIST OF ILLUSTRATIONS

SUMMARY

The response of a material to electromagnetic radiation may be described in terms of the frequency dependent complex index of refraction or equivalently in terms of the complex dielectric constant. These quantities, known as optical constants, are related to the electronic structure of the material at the atomic level. In solids the optical constants may be calculated from the reflectance of the solid by means of the Kramers-Kronig dispersion formulae if the reflectance is known over a wide spectral range. Reflectance measurements are sensitive to the surface condition of the material under investigation; in highly reactive metals, the formation of oxide layers may qualitatively as well as quantitatively affect the value of reflectance measurements.

The transition metal titanium, though increasingly important commercially, is not well understood in terms of its electronic properties. Experimentally, it is difficult to study due to its high reactivity with oxygen and nitrogen. Two experimental developments of the last decade, Auger electron spectroscopy (AES) and synchrotron radiation, have been combined with an ultra-high-vacuum apparatus to allow optical measurements over a wide spectral range while monitoring and controlling the surface environment of the sample. An automated computer-based data acquisition system has been developed to allow fast optical and AES measurements, insuring the stability of the surface during the measurement period.

Using this apparatus the reflectances of both atomically clean

and *in situ* oxidized titanium surfaces have been measured over a photon energy range of 2 to 25 eV. From these data the optical constants have been calculated and then related to theoretical calculations of the electronic structure of titanium and titanium oxide. By correlating the AES data with the optical data, two structures previously reported in the optical constants of titanium have been shown to be due to surface oxygen contamination. The optical constants of the clean surface are in qualitative agreement with theoretical models, but quantitative agreement must await refinement of the model. The energy loss function calculated from the optical constants of clean titanium is in good quantitative agreement with the energy loss spectrum measured directly using the AES apparatus, confirming the validity of both the experimental and calculational technique. These results have yielded values for both the bulk and surface plasmon energies.

Dramatic changes have been observed in the vacuum ultraviolet reflectance of titanium as it is oxidized. Both AES and optical measurements suggest that the oxide layer formed under exposure to low concentrations of oxygen or under oxygen ion bombardment is TiO rather than TiO_2 which forms with exposure to higher concentrations. Quantitative agreement in the location of structure exists between the experimental data and the calculated electronic structure of TiO. The success in the identification of the absorbed surface layer and the agreement with theory demonstrates the usefulness of this technique in the study of surfaces.

CHAPTER I

INTRODUCTION

Perspective

Optical measurements are an important method in the study of the electronic properties of a material. Historically, optical spectroscopy of isolated atoms, which yielded sharp emission and absorption lines that could be measured with great accuracy, was carried out in quantity during the last century and early part of this century. These studies provided much of the impetus for the development of quantum theory. The application of quantum theory to solids showed that the discrete energy levels of isolated atoms are spread into quasi-continuous bands due to the interaction of the electronic orbitals. The resulting broad optical structure of solids, however, could not be interpreted until band structure calculations became available in the 1950's. Since then a considerable amount of experimental data on the simple metals have been reported in the literature. Band structure calculations have been carried out and their electronic properties are reasonably well understood. From optical measurements, the complex index of refraction $\tilde{n}$ or the complex dielectric constant $\tilde{\varepsilon}$ may be determined. The imaginary part of $\tilde{\varepsilon}$ provides information on interband transitions, density of electronic states of the bands as well as the relative location of bands to the Fermi energy. The optical properties of metals are dominated by the free electrons in the metal, and information on the collective behavior of the free electrons may be determined from the real part of the

dielectric constant.

Because of the high opacity of metals in much of the spectral range, most optical measurements are performed using reflection techniques. Such measurements are naturally sensitive to the condition of the surface of the metal; and interpretation of the resulting measurements in terms of the bulk electronic properties depends on how well the surface region approximates the bulk properties. Most previous optical studies of metals have given only limited attention to the problem of surface conditions. However, in the last few years the strides in experimental surface physics now allow accurate measurement of surface properties and the preparation of atomically clean surfaces [1]. At the same time, the development of synchrotron radiation as a light source in the VUV has opened up a new region of the spectrum for optical measurements. Combining the techniques of surface physics with the use of synchrotron radiation would allow the measurement of the optical properties over a wide spectral range with the assurance that the measured values truly represent the material under investigation.

As mentioned before, the electronic properties of simple metals are rather well understood, however, this is not the case for the transition metals. Theoretical treatments have been hampered by the existance of the non-localized d electrons while experimental studies were generally avoided since the few existing results did not agree well with simple theory. More recently, progress in band structure calculations of transition metals [2-4] has spurred interest in optical measurememts [5-7] of these metals.

The Research

The transition metal titanium is the ninth most abundant element on earth and is widely used in alloys where light weight and strength are required. Despite its abundance and wide use, its electronic properties have been the object of only a few theoretical or experimental studies, and they are not well understood. Titanium presents a problem experimentally since it is highly reactive with oxygen and is the only element that will burn in nitrogen [8]. The oxidation process itself has been a field of considerable activity due to the importance of corrosion in commercial and military use of the metal [9]. Additionally, the oxides of titanium are currently being investigated for use in energy conversion devices [10]. A better understanding of the electronic structure of titanium and its oxides may further these applications as well as adding to the basic understanding of transition metals.

We have therefore undertaken an optical study of titanium with the following goals: the development of an experimental apparatus capable of optical measurements on well characterized surfaces; the measurement of the optical properties of clean titanium, which are then related to its electronic structure; determination of the effect of an oxide layer on the optical properties of titanium; and finally, interpretation of these optical properties in terms of the electronic structure of the layer.

The experimental apparatus uses a near-normal incidence reflectance technique with both conventional and synchrotron radiation as the source. Auger electron spectroscopy (AES) coupled with UHV techniques and *in situ* surface treatment facilities allows determination and modification of the sample surface composition. Rapid automated acquisition

of data insures compositional stability during measurements.

The optical properties of the clean surface are related to the $3d^2 4s^2$ valence structure of titanium and to the related energy loss spectra. The effects of both natural and in situ grown oxides on the optical properties are measured. The results, together with AES measurements, allow a determination of the chemical composition of the surface region, as well as the assignment of observed optical structure to specific interband transitions.

Review of the Literature

Only three theoretical studies of the electronic structure of titanium have been made. A partial band structure calculation by Mattheiss [11] using the augmented-plane-wave (APW) method with a $3d^3 4s^1$ valence configuration was published in 1964. A complete calculation for both the $3d^3 4s^1$ and $3d^2 4s^2$ configurations of titanium using the APW method was published in a series of three papers by Welch and Hygh [12-14] between 1970 and 1974. Previously (1967), a calculation using the cellular method was completed by Altman and Bradley [15]. They assumed a range of valancies from Ti^{+1} to Ti^{+4}. All of the above calculations were performed ab-initio and have not been fit to any experimental data.

The results of the above calculations all show a double peaked d band superimposed on the s band. The Fermi energy lies somewhere within the d band region with all calculations showing unoccupied d bands within 1-2 eV above the Fermi level. Hygh and Welch calculated the full-width-at-half-maximum (FWHM) of the occupied d bands to be 1.1 and 1.4 eV for exchange coefficients of 3/4 to 1, respectively. Altman and Bradley

calculated the density of states for Ti^{+2}, Ti^{+3}, and Ti^{+4} for which the FWHM has been estimated to be 6.5, 3.5, and 2.0 eV, respectively. Eastman [16] has measured the photoemission of titanium in the valence region, from which the FWHM of the d band has been calculated to be 2.0 eV with peaks 0.7 and 1.2 eV below the Fermi level. Comparing the shapes of the density of states calculations with the photoemission data shows that the best agreement with experiment is obtained by Welch and Hygh's exchange 1 calculation which exhibits peaks at 0.5 and 1.2 eV while Altman and Bradley's Ti^{+2} calculation showed approximately the right shape but was wide with peaks occurring at 1.1 and 3.4 eV.

Experimental optical measurements on titanium have been performed by several groups with a number of different techniques. Room temperature ellipsometric measurements over the range of .06-5 eV were made by Kirillova, et al. [17,18] (1962) using samples mechanically polished in acid. Mash and Motulevich [19] also have ellipsometrically measured the optical constants of titanium, but between the range of 0.1 and 3 eV on electropolished samples. Hass and Bradford [20] measured the reflectance of evaporated titanium films between 0.1 and 12.5 eV. They also made ellipsometric measurements in the visible to study the formation of an oxide. Their apparatus, however, was not ultra high vacuum. Johnson and Christy [21] measured both reflection and transmission of titanium between 0.5 and 6.5 eV using evaporated films. The measurements were made in a nitrogen atmosphere. Lynch, et al. [17] have made the most recent study using synchrotron radiation in the VUV. Their measurements extend from 0.15 to 30 eV and were made on electropolished samples. While these measurements were performed under high vacuum conditions,

the sample was exposed to the air for approximately 30 minutes prior to evacuation. A comparison of these results are shown in Figure 1. In the visible region of the spectrum, all of the measurements agree within ~10% in magnitude with general agreement in the location of structure. In the UV and VUV, the discrepancies are greater with variations of up to 20% in the magnitude of the reflectance and some slight differences in the location of structure. We note that structure in the reflectance persists to energies of 25 eV in the data of Lynch, et al.

Smith [22] has measured the optical constants of titanium at two wavelengths in the visible using ellipsometry on an atomically clean surface monitored by Auger spectroscopy. This has been the only study other than ours on atomically clean titanium. In a second paper, Smith [23] has studied the oxidation of titanium using the same techniques. Kucirek [24] has also studied the oxidation of titanium ellipsometrically, and by developing a family of curves for oxide layers of different thicknesses and making measurements in two different media, he has extrapolated his results to obtain the optical constants of clean titanium. The values obtained by Smith and Kucirek do not agree with each other.

The oxides of titanium which exist in states of TiO_x from TiO to TiO_2 have not been studied extensively optically. Limited studies in the infrared and visible [25,26] have been made, and several photoemission studies [27,28] of the oxides are reported. Theoretically, bandstructures have been calculated for only TiO. Fischer [29] has interpreted his x-ray data in terms of a molecular orbital calculation, while band calculations have been made by Ern and Switendick [30] (1965) and Jennison and Kunz [31] (1977). Qualitatively, they all predict a mixture of s and

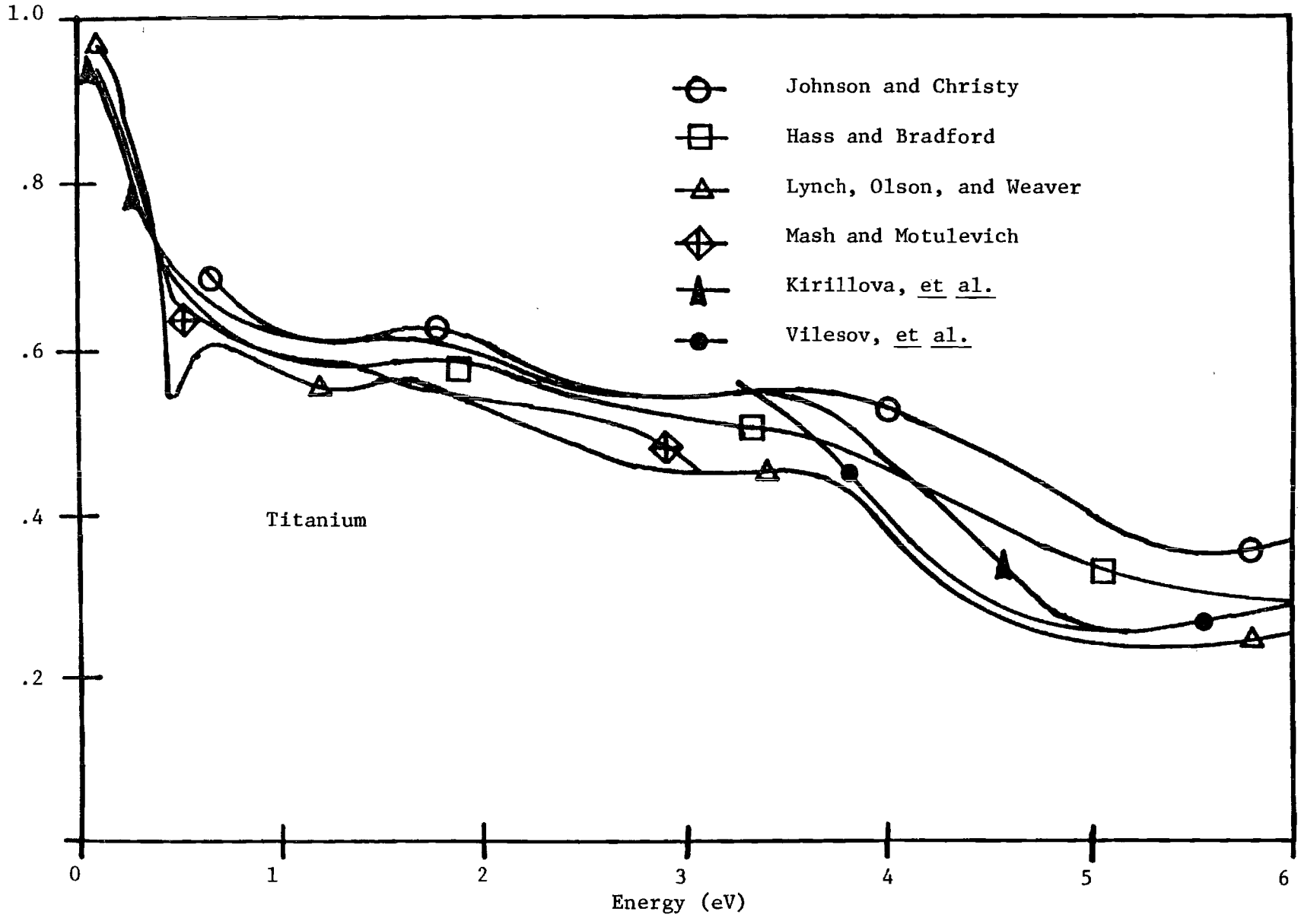

Figure 1. Reflectance of Titanium From Other Studies

d bands near the Fermi energy while the oxygen 2p bands lie about 10 eV below the Fermi level and the oxygen 2s bands lie more than 20 eV below the Fermi level.

CHAPTER II

THEORY

In this chapter, we describe the optical properties of a solid through a set of macroscopic frequency dependent optical constants and show how these constants may be determined from experimental reflectance measurements. The optical constants are then related to the microscopic theory of metals using a semiclassical approach that is consistant with the one electron band theory of solids. The effects of the surface condition of the metal, especially dielectric films, on the reflectance is discussed. Finally, an elementary theory of Auger electron spectroscopy is presented to aid in the understanding of this technique as a monitor of surface contamination.

Optical Constants

Classically, the propagation of electromagnetic waves through a medium is governed by Maxwell's equations which are written as follows, following Ziman [4],

$$\nabla \times \vec{H} = \frac{(1+4\pi\alpha)}{c} \frac{\partial \vec{E}}{\partial t} + \frac{4\pi\sigma}{c} \vec{E} \quad , \quad \nabla \cdot \vec{E} = 0$$

$$\nabla \times E = - \frac{\mu}{c} \frac{\partial \vec{H}}{\partial t} \quad , \quad \nabla \cdot \vec{H} = 0 \qquad (2\text{-}1)$$

The quantities which describe the properties of the medium are the polarizability α, which is a measure of the internal electrical polarization of

the material; the permeability μ, which is a measure of the magnetic polarization of the material; and the conductivity σ, a measure of the real currents created by the electric field. In solids, these coefficients are, in general, tensor quantities due to the anisotropy of the solid. For the purpose of simplicity, however, we treat them as scalar quantities in this discussion. As a further simplification, we consider only nonmagnetic materials setting $\mu = 1$.

Eliminating the magnetic field in (2-1), we arrive at the differential equation

$$\nabla^2 \vec{E} = \frac{(1+4\pi\alpha)}{c^2} \frac{\partial^2 \vec{E}}{\partial t^2} + \frac{4\pi\sigma}{c^2} \frac{\partial \vec{E}}{\partial t} \quad . \tag{2-2}$$

The solution to this differential equation may be written in the form

$$\vec{E} = \vec{E}_o \exp[i(\vec{K} \cdot \vec{r} - \omega t)] \quad . \tag{2-3}$$

Substituting (2-3) into (2-2) yields

$$-\vec{K} \cdot \vec{K} = \frac{(1+4\pi\alpha)}{c^2} \omega^2 - \frac{4\pi\sigma}{c^2} i\omega$$

or that the propagation constant

$$|K| = \frac{\omega}{c} \left(1 + 4\pi\alpha + i \frac{4\pi\sigma}{\omega}\right)^{1/2} \quad . \tag{2-4}$$

We now define the complex dielectric constant

$$\tilde{\varepsilon} \equiv \varepsilon_1 + i\varepsilon_2 = 1 + 4\pi\alpha + i\,\frac{4\pi\sigma}{\omega} \quad . \tag{2-5}$$

The complex dielectric constant $\tilde{\varepsilon}$, which is a function of the frequency ω both explicitly and implicitly, contains all the information necessary for understanding the propagation of electromagnetic radiation in a medium. Both α and σ are also functions of the frequency.

Alternatively, we note that radiation in a medium may also be characterized by the real index of refraction n and the extinction coefficient k. The index of refraction is defined as the ratio of the velocity of the radiation in free space to the phase velocity in the medium while the extinction coefficient is defined such that the amplitude of the radiation is attenuated by a factor of $\exp(2\pi k)$ over a distance of one free space wavelength. Thus, we can write our wave equation as

$$\vec{E} = \vec{E}_o \exp[i\omega(\frac{nr}{c} - t)]\exp(-\frac{k\omega r}{c}) \quad . \tag{2-6}$$

Defining now the complex index of refraction

$$\tilde{n} = n + ik \tag{2-7}$$

we can write (2-6) as

$$\vec{E} = \vec{E}_o \exp[i\omega(\frac{\tilde{n}r}{c} - t)] \quad . \tag{2-8}$$

Comparing (2-8) with (2-3) shows that the propagation constant $|\vec{K}|$ is just

$$|\vec{K}| = \frac{\omega}{c} \tilde{n} \tag{2-9}$$

Substituting (2-5) into (2-4) and comparing with (2-9) yields the result

$$\tilde{\varepsilon} = (\tilde{n})^2 \tag{2-10}$$

or

$$\varepsilon_1 = n^2 - k^2 \qquad \text{and} \qquad \varepsilon_2 = 2nk \quad . \tag{2-11}$$

Therefore, we see that the complex dielectric constant $\tilde{\varepsilon}$ and the complex index of refraction $\tilde{n}$ are equivalent descriptions of the optical properties of a material. As an aid to the physical interpretation of $\tilde{\varepsilon}$ and $\tilde{n}$ we note that the power dissipated in the material by Joule heating is the $\mathrm{Re}[\vec{J}\cdot\vec{E}]$ where J is the current density given by

$$\vec{J} = \frac{i\omega}{c} \tilde{\varepsilon} \vec{E} \quad ; \tag{2-12}$$

and the fraction of the power absorbed is

$$a = \frac{\mathrm{Re}(\vec{J}\cdot\vec{E})}{n|\vec{E}|^2} = \frac{2k\omega}{c} = \frac{\omega}{nc} \varepsilon_2 \quad . \tag{2-13}$$

Thus, the imaginary parts of $\tilde{\varepsilon}$ and $\tilde{n}$ are directly proportional to the absorption coefficient of the material.

Normal Incidence Reflectance

At the free space-solid interface radiation will be reflected in

accordance with Fresnel's equations for the complex index of refraction [32]:

$$\text{(TE polarization)} \quad \frac{\tilde{E}_r}{\tilde{E}_1} = \frac{\cos\theta - \tilde{n}\cos\phi}{\cos\theta + \tilde{n}\cos\phi} \tag{2-14}$$

and

$$\text{(TM polarization)} \quad \frac{\tilde{E}_r}{\tilde{E}_1} = \frac{-\tilde{n}\cos\theta + \cos\phi}{\tilde{n}\cos\theta + \cos\phi} \tag{2-15}$$

where

$\tilde{E}_r$ = electric field magnitude of reflected wave

$\tilde{E}_1$ = electric field magnitude of incident wave

θ = angle of incidence

ϕ = angle of transmission

At normal incidence the two equations give the same result

$$\frac{\tilde{E}_r}{\tilde{E}_i} = \frac{1-\tilde{n}}{1+\tilde{n}} \quad . \tag{2-16}$$

This ratio is in general complex and we define the reflection coefficient

$$\tilde{r} = \frac{\tilde{E}_r}{\tilde{E}_1} = \frac{1-\tilde{n}}{1+\tilde{n}} = re^{i\theta} \tag{2-17}$$

where r is the magnitude of the reflection coefficient and θ is the phase

change on reflection. However, the quantity that is measured experimentally is not $\tilde{E}$ but the energy flux $\sim\tilde{E}\cdot\tilde{E}^*$. We therefore define the reflectance

$$R = \frac{\tilde{E}_r \cdot \tilde{E}_r^*}{\tilde{E}_1 \cdot \tilde{E}_1^*} = \tilde{r}\cdot\tilde{r}^* = r^2 \qquad (2\text{-}18)$$

which is the experimentally measured quantity. We see from Equation (2-17) that a knowledge of $\tilde{r}$ determines the optical constants $\tilde{n} = n + ik$. Measurement of the reflectance R does not determine $\tilde{r}$ since the phase information θ is lost. The phase information may be recovered by the use of a Kramers-Kronig dispersion relationship, which is a general relationship connecting the real and imaginary parts of the response function of any linear and causal system [34]. In general, for a response function

$$A(\omega) = A'(\omega) + iA''(\omega) \quad . \qquad (2\text{-}19)$$

The Kramers-Kronig relationships are

$$A'(\omega) = \frac{2}{\pi} P \int_0^\infty \frac{\omega' A''(\omega')\,d\omega'}{(\omega')^2 - \omega^2} \qquad (2\text{-}20)$$

and

$$A''(\omega) = -\frac{2\omega}{\pi} P \int_0^\infty \frac{A'(\omega')\,d\omega'}{(\omega')^2 - \omega^2} \qquad (2\text{-}21)$$

where P indicates the principal part of the integral. Returning to the reflection coefficient we may write $\tilde{r}$ in the form of (2-19) by taking the

complex logarithm

$$\ln(\tilde{r}) = \ln(r) + i\theta = \frac{1}{2}\ln(R) + i\theta \tag{2-22}$$

and substituting into equation (2-21) yielding

$$\theta(\omega) = -\frac{\omega}{\pi} P \int_0^\infty \frac{\ln[R(\omega')]}{(\omega')^2 - \omega^2}\, d\omega' \tag{2-23}$$

which may be rewritten [33] as

$$\theta(\omega) = -\frac{1}{2\pi} \int_0^\infty \frac{d \ln[R(\omega')]}{d\omega'} \ln\left|\frac{\omega'+\omega}{\omega'-\omega}\right| d\omega' . \tag{2-24}$$

This integral may be computed numerically if $R(\omega)$ has been measured over a sufficiently wide range of ω [34]. With $\tilde{r}$ determined, the optical constants may be calculated by solving (2-17) for n and k and substituting (2-18) yielding

$$n = \frac{1-R}{1+R-2\sqrt{R}\cos\theta} \tag{2-25}$$

and

$$k = \frac{\sqrt{R}\sin\theta}{1+R-2\sqrt{R}\cos\theta} . \tag{2-26}$$

The Optical Properties of Metals

In this section we relate the macroscopic complex dielectric

constant $\tilde{\varepsilon}(\omega)$, which describes the optical properties of a material, to the electronic band structure of metals. In order to better understand the physical processes, we will separate the contributions to $\tilde{\varepsilon}(\omega)$ into two parts: that part due to the free electrons in the metal and that part due to interband transitions. The Drude-Zener theory of metals [35] provided the first theory and considered only the free electron contributions to $\tilde{\varepsilon}(\omega)$. We make use of this description, modified for band effects, to discuss the free electron contribution. Interband transitions are treated based on an independent particle, quantum mechancial model [36]. Collective effects, including interaction with the lattice, are ignored; however, these effects are discussed in a qualitative manner. The final results have the same form as the collective theory of Bohm and Pines [37].

Following the theory of Drude and Zener, the conduction electrons are considered to be free and noninteracting. The equation of motion for an electron under the influence of an oscillating electric field $\vec{E}_o e^{i\omega t}$ is

$$\frac{d^2\vec{r}}{dt^2} + \gamma \frac{d\vec{r}}{dt} = - \frac{e\vec{E}_o e^{i\omega t}}{m} \qquad (2\text{-}27)$$

where the magnetic effects are ignored and γ is a damping factor attributable to interactions with the lattice. The solution to this equation is

$$\vec{r} = \frac{e\vec{E}_o e^{i\omega t}}{m(\omega^2 - i\omega\gamma)} . \qquad (2\text{-}28)$$

Differentiating, we determine the velocity to be

$$\vec{v} = \frac{-e(\gamma - i\omega)E_o e^{i\omega t}}{m(\omega^2 + \gamma^2)} . \tag{2-29}$$

Now the current density for N electrons is given by

$$\vec{J} = Ne\vec{v} \tag{2-30}$$

and substituting (2-29) into (2-30) yields

$$\vec{J} = -Ne^2 \frac{(\gamma - i\omega)}{m(\omega^2+\gamma^2)} \vec{E}_o e^{i\omega t} . \tag{2-31}$$

The conductivity is defined by $\vec{J} = \sigma\vec{E}$ and we recognize the conductivity to be

$$\sigma = \frac{-Ne^2(\gamma - i\omega)}{m(\omega^2+\gamma^2)} . \tag{2-32}$$

The Drude theory for dc conductivity yields [38]

$$\sigma = \frac{Ne^2\tau}{m} \tag{2-33}$$

where τ is the relaxation time. The results of (2-32) should reduce to (2-33) when $\omega = 0$; doing so we identify

$$\gamma = \tau^{-1} . \tag{2-34}$$

After making the above identification, we substitute (2-32) into our expression for $\tilde{\varepsilon}$, yielding

$$\tilde{\varepsilon} = 1 + 4\pi\alpha - \frac{4\pi Ne^2}{m}\left(\frac{1}{\omega^2 + \tau^{-2}}\right) + i\,\frac{4\pi Ne^2}{m\omega}\left(\frac{\tau^{-1}}{\omega^2 + \tau^{-2}}\right) \quad . \tag{2-35}$$

The last two terms of (2-35) are the conduction band contribution to the complex dielectric constant. Separating $\tilde{\varepsilon}$ into the contributions of the conduction band and interband transitions we may write

$$\tilde{\varepsilon} = \tilde{\varepsilon}^b + \tilde{\varepsilon}^c \quad , \tag{2-36}$$

where b refers to interband transitions and c refers to the conduction band, or from (2-35) and (2-5)

$$\varepsilon_1 = \varepsilon_1^b - \frac{4\pi Ne^2}{m}\left(\frac{1}{\omega^2 + \tau^{-2}}\right) \tag{2-37}$$

$$\varepsilon_2 = \varepsilon_2^b + \frac{4\pi Ne^2}{m}\,\frac{1}{\omega}\left(\frac{\tau^{-1}}{\omega^2 + \tau^{-2}}\right) \tag{2-38}$$

The experimental range investigated in this work included photon energies above 2 eV only, or $\omega = E/h \sim 10^{15}$/sec while the inverse relaxation time τ^{-1} is of the order 10^{13}/sec [34]. We therefore ignore τ^{-2} in the denominator of (2-37) and (2-38) since it is much smaller than ω^2. At this point we introduce a new quantity, the free electron plasma frequency ω_p defined by

$$\omega_p^2 \equiv \frac{4\pi Ne^2}{m} \quad . \tag{2-39}$$

If we assume that the only contribution to the optical properties of a metal are due to the free electrons, equivalently that α in (2-35) is zero, then we may rewrite (2-37) and (2-38) as

$$\varepsilon_1 = 1 - \frac{\omega_p^2}{\omega^2} \tag{2-40}$$

and

$$\varepsilon_2 = \frac{\tau^{-1}\omega_p^2}{\omega^3} \quad . \tag{2-41}$$

This simplified form illustrates the basic optical properties of a metal and the physical significance of the plasma frequency. A quick calculation shows that $\omega_p \sim 2 \times 10^{15}$/sec which lies in the ultraviolet region of the spectrum. The absorption, proportional to ε_2, is very high at low frequencies, but drops toward zero as ω increases. For $\omega < \omega_p$, ε_1 is negative; since $\varepsilon_1 = n^2 - k^2$, n must be near zero, with k increasing as ω approaches zero. From (2-17) and (2-18), the reflectance in terms of n and k is

$$R = \frac{(n-1)^2 + k^2}{(n+1)^2 + k^2} \tag{2-42}$$

which tends to R = 1 for small values of n. The plasma frequency, ω_p, separates the region of high reflectivity from the region of transparency. This behavior is illustrated in Figure 2. The behavior of the optical

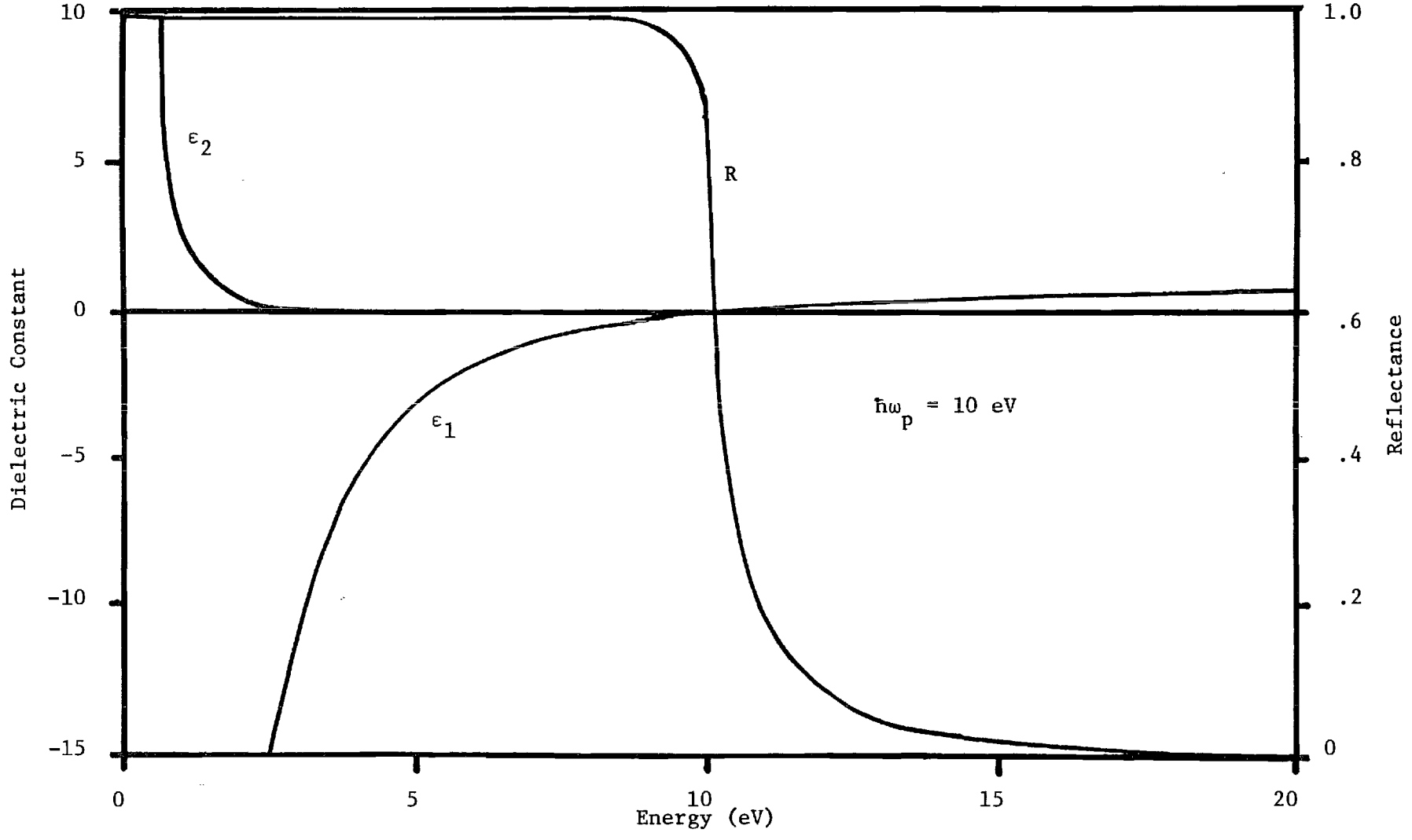

Figure 2. Optical Constants and Reflectance for the Free Electron Model with $\hbar\omega_p$ = 10 eV

constants about the plasma frequency is the result of the collective oscillation of the free electrons [39]. This is a longitudinal oscillation known as a plasmon that occurs when

$$\tilde{\varepsilon}_{long}(\omega,\vec{q}) = 0 \quad . \tag{2-43}$$

The complex optical dielectric constant is transverse but for wavelengths longer than atomic distances [35]

$$\tilde{\varepsilon}_{long}(\omega,\vec{q}) = \tilde{\varepsilon}_{trans}(\omega,\vec{q}) \quad . \tag{2-44}$$

Since electromagnetic radiation is transverse, there should be no coupling to the plasmon; however, a small coupling due to interaction with the lattice does occur [35]. Fast electrons entering a metal can excite plasmon oscillations and lose an amount of energy equal to ω_p. This loss can be related to the dielectric constant through the energy loss function [40]

$$-\mathrm{Im}\left(\frac{1}{\tilde{\varepsilon}}\right) = \frac{\varepsilon_2}{\varepsilon_1^2 + \varepsilon_2^2} \tag{2-45}$$

which has a maximum near the point where $\varepsilon_1 = 0$,

Up to this point only the case of free electrons have been considered; if the conduction electrons are instead described by Bloch functions, then an expression for the conductivity and hence $\tilde{\varepsilon}$ can be derived based on the one electron, band theory of solids [36]. The

result, as given by Cohen [41], is similar to equations (2-40) and (2-41) except that the electron mass in equation (2-39) is replaced by an effective electron mass as modified by the band shape and expressed as

$$(m^*)^{-1} = (4\pi^3 N_c^3 \hbar^2)^{-1} \int d^3k \, \frac{1}{3} \nabla_k^2 H \tag{2-46}$$

where H is the electron energy and the integration is over the filled portion of the conduction band. Thus, the effect of m* will be to raise or lower the effective plasma frequency with respect to the free electron plasma frequency.

Consider now the effects of interband transitions on the optical constants. The first order dipole transition probability per unit time is given by Bassani and Parravicini [42] as

$$P_{vk\to ck} = \frac{2\pi}{\hbar} \left(\frac{eA_o}{mc}\right)^2 \left|\vec{e}\cdot M_{cv}(\vec{k})\right|^2 \delta(E_c(\vec{k}) - E_v(\vec{k}) - \hbar\omega) \tag{2-47}$$

where $\vec{e}\cdot M_{cv}(\vec{k}) = \langle \psi_{ck} | \vec{e}\cdot\vec{p} | \psi_{vk} \rangle$. In (2-47) we assume that the momentum of the photon is small compared to the electron momentum so that only "vertical" transitions in an energy band diagram are possible. These are known as direct transitions. The total number of transitions per unit time per unit volume is obtained by summing over all empty bands, filled bands, and spin states while integrating over occupied k space yielding

$$W(\omega) = \frac{2\pi}{\hbar}\left(\frac{eA_o}{mc}\right)^2 \sum_{v,c} \int \frac{2d^3k}{(2\pi)^3} \left|e\cdot M_{cv}(\vec{k})\right|^2 \delta(E_c(k) - E_v(k - \hbar\omega) \quad . \tag{2-48}$$

The absorption of radiation is the ratio of the energy absorbed per unit

time per unit volume to the flux in that volume. The energy density $U(\omega)$ in terms of the vector potential is

$$U(\omega) = \frac{n^2\omega^2}{2\pi c^2} A_o^2 \tag{2-49}$$

yielding an absorption of

$$a = \frac{\hbar\omega W(\omega)}{(c/n)U(\omega)} = \frac{2\,\hbar c W(\omega)}{\omega n A_o^2} , \tag{2-50}$$

and then from (2-13) we have

$$\varepsilon_2(\omega) = \frac{nc}{\omega} a = \frac{2\pi\hbar c^2 W(\omega)}{\omega^2 A_o^2} . \tag{2-51}$$

Substituting (2-48) into (2-51) yields the expression for ε_2 resulting from interband transitions

$$\varepsilon_2^b(\omega) = \frac{4\pi^2 e^2}{m^2\omega^2} \sum_{v,c} \int_{BZ} \frac{2d^3k}{(2\pi)^3} \left| e\cdot M_{cv}(k) \right|^2 \delta(E_c(k) - E_v(k) - \hbar\omega) . \tag{2-52}$$

The interband contribution to ε_1 can be obtained by Kramers-Kronig inversion; putting ε_2^b into (2-20) yields

$$\varepsilon_1^b(\omega) = 1 + \frac{2}{\pi} P \int_o^\infty \omega' \varepsilon_2^b(\omega') \frac{1}{(\omega')^2 - \omega^2} d\omega' . \tag{2-53}$$

Substituting (2-52) into (2-53) then gives

$$\varepsilon_1^b(\omega) = 1+\frac{8\pi c^2}{m^2}\sum_{v,c}\int_{BZ}\frac{2d^3k}{(2\pi)^3}\frac{|e\cdot M_{cv}(k)|^2}{[E_c(k)-E_v(k)]/\hbar}\frac{1}{[E_c(k)-E_v(k)]^2/\hbar^2-\omega^2} \tag{2-54}$$

To simplify the notation, the interband oscillator strength density is defined, following Sutherland [43], to be

$$f_{cv}(k) = \frac{2\hbar}{m}\frac{|e\cdot M_{cv}(k)|^2}{[E_c(k)-E_v(k)]} \tag{2-55}$$

which we note is a positive quantity; therefore, (2-54) becomes

$$\varepsilon_1^b(\omega) = 1 + \frac{4\pi e^2}{m}\sum_{v,c}\int_{BZ}\frac{2d^3k}{(2\pi)^3}f_{cv}(k)\frac{1}{[E_c(k)-E_v(k)]^2/\hbar^2-\omega^2} \tag{2-56}$$

Substituting (2-39), (2-46) and (2-56) into (2-37) produces the total real dielectric constant

$$\varepsilon_1 = 1 - (\frac{\omega_p^*}{\omega})^2 + \frac{4\pi e^2}{m}\sum_{v,c}\int_{BZ}\frac{2d^3k}{(2\pi)^3}f_{cv}(k)\frac{1}{[E_c(k)-E_v(k)]^2/\hbar^2-\omega^2} \tag{2-57}$$

where ω_p^* is the band modified plasma frequency. The largest contribution of the interband term to ε_1 occurs at energies of $h\omega$ near transition energies where the denominator of the interband term approaches zero; however, the value of ε_1 is modified by the interband term even outside the frequency span of the interband transitions. Following Cohen, this effect may be more clearly seen using the following approximation: replace the denominator in the interband term $(\omega^2-[E_c(k)-E_v(k)]^2/\hbar^2)$ by ω^2 for $\omega^2 >> [E_c(k)-E_v(k)]^2/\hbar^2$ and by $-[E_c(k)-E_v(k)]^2/\hbar^2$ for $\omega^2 << [E_c(k)-E_v(k)]^2/\hbar^2$.

The result is

$$\varepsilon_1 = 1 + \frac{4\pi e^2}{m} \sum_{\substack{v,c \\ \hbar\omega<E_c-E_v}} \int_{BZ} \frac{2d^3k}{(2\pi)^3} \frac{f_{cv}(k)}{[E_c(k)-E_v(k)]^2/\hbar^2}$$

$$-[\omega_p^* + \frac{4\pi e^2}{m} \sum_{\substack{v,c \\ \hbar\omega>E_c-E_v}} \int_{BZ} \frac{2d^3k}{(2\pi)^3} f_{cv}(k)]/\omega^2 \qquad (2\text{-}58)$$

which may be written in the form

$$\varepsilon_1 = A - \frac{B}{\omega^2} \, . \qquad (2\text{-}59)$$

The plasma resonance condition is

$$\tilde{\varepsilon} = \varepsilon_1 = 0 \qquad \text{or} \qquad \omega^2 = \frac{B}{A} \, . \qquad (2\text{-}60)$$

The result from (2-58) indicates that interband transitions at energies less than $\hbar\omega_p^*$ tend to raise the effective plasma frequency while transitions at energies greater than $\hbar\omega_p^*$ tend to lower the effective plasma frequency. In transition, metals such as titanium the d bands, and s and p bands overlap, with many low lying interband transitions. While these transitions may extend close to the free electron plasma frequency ω_p rendering our approximation in (2-57) inaccurate, the general result of increasing the plasma frequency holds since the sign of the components of the denominator remain the same even though their magnitude is different.

Returning now to the imaginary part of $\tilde{\varepsilon}$, we define the optical joint density of states to be

$$J_{cv}(h\omega) = \int_{BZ} \frac{2d^3k}{(2\pi)^3} \delta[E_c(k) - E_v(k) - \hbar\omega] \quad . \tag{2-61}$$

The joint density of states may be thought of as the sum of all pairs of states (one empty, one occupied) having an energy difference of $h\omega$ and the same k value. We now also make the assumption that the oscillator strengths defined in (2-55) are independent of k [35]. Using (2-55) and (2-61), we may now rewrite (2-52) as

$$\varepsilon_2^b(\omega) = \frac{2\pi^2 e^2}{m\omega} \sum_{v,c} f_{cv} J_{cv}(h\omega) \quad . \tag{2-62}$$

From (2-38), (2-39), (2-46), and (2-62), the total imaginary component of the dielectric constant is

$$\varepsilon_2 = \frac{\tau^{-1}(\omega_p^*)^2}{\omega^3} + \frac{2\pi^2 e^2}{m\omega} \sum_{v,c} f_{cv} J_{cv}(h\omega) \quad . \tag{2-63}$$

The first term is due to absorption caused by scattering of the conduction electrons, while the second term is due to interband absorption. The first term is important only at low frequencies and may be neglected in the frequency range of this work. Note that the second term only contributes to ε_2 at the frequencies of interband absorption.

The model used to this point has included only direct transitions where electron momentum is conserved. Experimental data for metals have indicated that momentum conservation may not be an important selection

rule [35]. One possible mechanism is electron-phonon interactions where phonons carry any excess momentum and very little energy from the electrons. This effect allows transitions from one energy to another without moving vertically in an energy band diagram. In the extreme case this results in replacing the optical joint density of states in (2-63) with the convolution of the density of states of the occupied and vacant bands. Therefore, for the case of indirect transitions

$$\varepsilon_2 = \frac{\tau^{-1}(\omega_p^*)^2}{\omega^3} + \frac{2\pi^2 e^2}{m\omega} \sum_{v,c} f_{cv} \int N_c(E) N_v(E-\hbar\omega)\, dE \qquad (2\text{-}64)$$

where N_c and N_v are the density of states for the vacant and occupied bands.

Surface Effects

The calculation of the normal incidence reflectance earlier in the chapter assumed that the bulk properties of the solid extended to the interface and that the surface itself contributed nothing to the optical properties of the material. A real surface, however, has a number of properties that may affect the measured reflectance. The termination of the lattice at the surface can cause relaxation of the surface atoms away from the bulk or in the extreme case produce a reconfiguration of the surface atoms. This spatial reordering of the surface plus the fact that the abrupt termination of the material may leave bonds "dangling" in space will alter the electronic structure of the surface enough to produce new electronic surface states which may be reflected in the optical constants. We may estimate the effect of the surface

region using a simple classical model. For a material of extinction coefficient k, the strength of the electric field at a depth x is

$$E(x) = E_o \exp[-2\pi kx/\lambda] \tag{2-65}$$

where E_o is the field strength just inside the surface. From equation (2-47) the probability of an interband transition is proportional to E^2. If we assume that the ratio of the number of transitions occuring in a region dx at depth x to the total number of transitions is the fractional contribution of the region dx to the optical constants, then the fractional contribution, F, of a surface region of thickness x_0 to the optical constants is given by

$$F = \frac{\int_o^{x_o} E^2_{(x)}\,dx}{\int_o^{\infty} E^2_{(x)}\,dx} = 1 - e^{-4\pi kx_o/\lambda} \tag{2-66}$$

using (2-65) for $E_{(x)}$. As an upper limit we choose $x_0 = 30$ A, corresponding to a surface layer of seven to ten monolayers. In Table 2-1, F has been calculated for several values of k and for several photon energies spanning the range of our investigation. The results indicate that the contributions may be significant, especially for absorbing media at high photon energies.

Another effect is the existence of collective surface oscillations equivalent to the plasmon in the bulk and known, therefore, as the surface plasmon. Ritchie [44] has shown that the plasmon frequency for a plane

Table 2-1. Fractional Contribution of a 30A Surface Layer to the Total Measured Optical Constants for Several Photon Energies and Extinction Coefficients. The First Column (k*) Uses Values of k Computed From the Drude-Zener Theory with $\hbar\omega_p = 10$ eV.

Photon Energy $\hbar\omega$	Extinction Coefficient k			
	k*	.1	1	5
2 eV	.26	.006	.06	.27
4 eV	.25	.012	.12	.46
10 eV	.08	.03	.27	.79
20 eV	.01	.06	.47	.96

surface is related to the bulk plasmon frequency ω_p by the simple relation

$$\omega_s = \omega_p/\sqrt{2} \quad . \tag{2-67}$$

However, the surface plasma oscillation is normal to the surface and, like the bulk plasmon, does not couple strongly to normal incidence transverse radiation. Surface roughness increases the coupling [45] and decreases in reflectance have been reported at the surface plasmon frequency [46,47].

Surface contamination may also have a significant effect on the measured optical constants of a material. In particular, we consider the effect of a thin dielectric film such as an oxide layer on a metal surface. Following McIntyre [48], the normal incidence reflection coefficient for a three phase system with film thickness d is

$$\tilde{r}_{123} = \frac{\tilde{r}_{12} + \tilde{r}_{23} e^{i(4\pi\tilde{n}_2 d/\lambda)}}{1 + \tilde{r}_{12}\tilde{r}_{23} e^{i(4\pi\tilde{n}_2 d/\lambda)}} \tag{2-68}$$

where the overall reflectance is

$$R_{123} = |\tilde{r}_{123}|^2 \tag{2-69}$$

and the subscripts indicate: 1 - ambient medium, 2 - surface film, and 3 - substrate. We now assume that the dielectric film thickness d is much less than the wavelength allowing us to express the reflection

coefficient r_{123} in terms of the film-free reflection coefficient r_{13}. To first order in d/λ,

$$r_{123} = r_{13}[1 + i \frac{4\pi d n_1}{\lambda} (\frac{\tilde{\varepsilon}_2 - \tilde{\varepsilon}_3}{\tilde{\varepsilon}_1 - \tilde{\varepsilon}_3})] \quad . \tag{2-70}$$

Calculating R_{123} and neglecting terms of d^2/λ^2, we have

$$R_{123} = R_{13}[1 - \frac{8\pi d n_1}{\lambda} \mathrm{Im}(\frac{\tilde{\varepsilon}_2 - \tilde{\varepsilon}_3}{\tilde{\varepsilon}_1 - \tilde{\varepsilon}_3})] \quad . \tag{2-71}$$

Setting $\tilde{\varepsilon}_1 = 1$, and rationalizing yields

$$R_{123} = R_{13}\{1 - \frac{8\pi d}{\lambda} \frac{[\varepsilon_2''(1-\varepsilon_3') - \varepsilon_3''(1-\varepsilon_2')]}{(1-\varepsilon_3')^2 + \varepsilon_3''^2}\} \tag{2-72}$$

where we have separated the real and imaginary parts of the dielectric constant using the notation $\tilde{\varepsilon} = \varepsilon' + i\varepsilon''$.

In order to examine the implications of (2-72), we consider a simple microscopic model of a dielectric and the resulting optical constants. The fundamental difference between a metal and a dielectric is the lack of free electrons in the dielectric due to the fermi level occurring between bands. Bands below the fermi level are completely full while bands above are empty. Neglecting phonon absorption in the infrared, the optical properties are dominated by interband transitions which occur only above a certain threshold energy equal to the minimum energy gap between the occupied and vacant bands. Below this photon energy the

material is transparent. Equations (2-52) and (2-56) for the optical constants due to interband transitions may be used to describe the optical properties of a dielectric. For a single absorption band the imaginary part of the dielectric constant peaks at the absorption band energy while the real part peaks at a slightly lower energy and has a minimum at a slightly higher energy as shown in Figure 3. The reflectance, also shown in Figure 3, peaks near the minimum in the real part of the dielectric constant.

Using the above model for a dielectric film and the Drude-Zener model for the metal substrate, the behavior of equation (2-72) may be examined. First, the visible and near UV region of the spectrum is considered. We consider this region to be below the substrate plasma frequency and also below the onset of interband absorption in the dielectric. In this region $\varepsilon_2'' = 0$ while $\varepsilon_2' > 1$ and $\varepsilon_3'' > 0$; therefore, the net effect of the dielectric film will be the lowering of the reflectance in this region. At an energy above the substrate plasma energy and slightly below a film absorption band $\varepsilon_2'' > 0$ and $\varepsilon_2' > 1$ while $0 < \varepsilon_3' < 1$ and $\varepsilon_3'' > 0$ but small. Now the contribution of the film to the reflectance is more negative, with both terms in the numerator adding constructively and the denominator being smaller than before. However, at energies slightly above the dielectric absorption band ε_2' exhibits a minimum and is less than one. The two terms in the numerator tend to cancel, and if the minima in ε_2' is sufficiently deep the second term may dominate the first causing a net increase in the reflectance. As the film becomes thicker, equation (2-72) becomes less accurate and equations (2-68) and (2-69) must be used. For an absorbing film, we note that the reflectance R_{123}

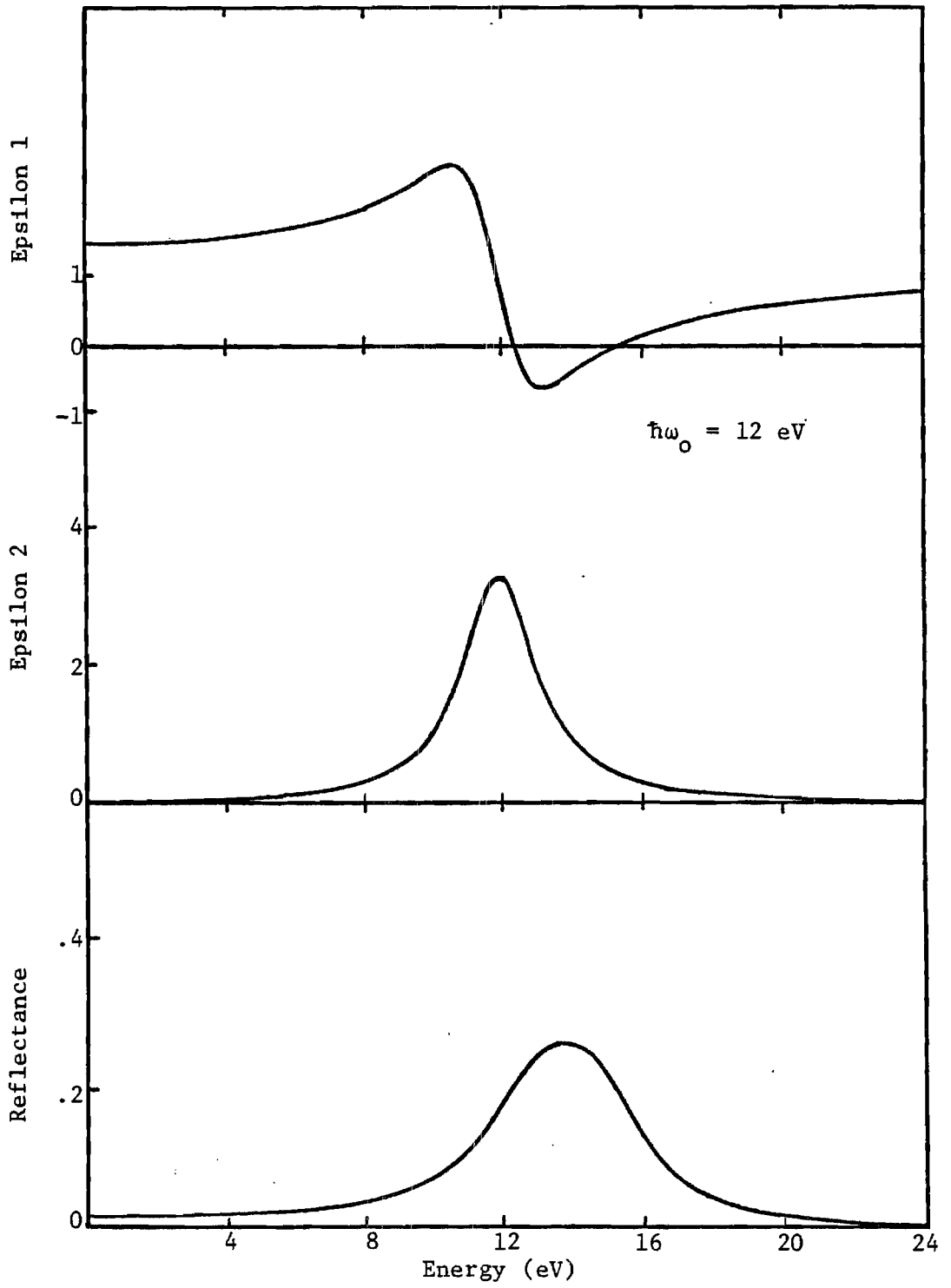

Figure 3. Optical Constants and Reflectance for a Single Oscillator Dielectric

approaches R_{12} as the film becomes thicker.

A final effect of a dielectric film is the lowering of the surface plasmon frequency. The inclusion of a dielectric film modifies [49] equation (2-67) such that

$$\omega_s = \omega_p/\sqrt{1+\varepsilon} \tag{2-73}$$

where ε is the dielectric constant of the film.

The above treatment of a dielectric film on a metal substrate has certain limitations since the model neglects variations in composition of the layer that might be expected in multi-oxide systems and also neglects the physical interaction between the layer and the substrate. The former situation may be approximated through a multi-layer treatment where a mean dielectric constant for the surface layer is defined [48].

$$\langle\tilde{\varepsilon}_s\rangle = \frac{1}{d}\int_o^d \tilde{\varepsilon}_s(z)dz \quad . \tag{2-74}$$

The latter problem is similar to the previously discussed effect due to the reordering of the clean surface. The presence of the absorbed layer may modify the substrate surface properties enough to change the optical properties of the substrate. No simple solution to this problem has been found since it is not possible to experimentally identify the various sources of the changes in the optical constants as a dielectric film is deposited on a substrate. These layer-substrate interface effects are just included in the mean surface dielectric constant $\langle\tilde{\varepsilon}_s\rangle$.

Auger Electron Spectroscopy

The importance of the surface region to the measured optical properties of a metal requires that in any successful experiment the chemical composition of the surface must be accurately known. Auger electron spectroscopy (AES) provides a tool that meets all of the experimental requirements for in-situ measurement of surface composition. The following discussion provides an elementary basis for understanding of the technique.

The basic processes of AES are the ionization of atomic core levels in the material under analysis by an electron beam and the energy analysis of Auger electrons emitted from the sample as a result of the ionization. When a core vacancy is created by ionization of an atom in the solid, an electron from a higher energy state fills the vacancy immediately. The energy released by this transition may be in the form of a photon or it may be given to another electron. This second or Auger electron may then have enough energy to escape the solid. It will have an energy equal to the energy difference of the transition involved minus the energy required for escape, and is characteristic of the element involved. This process is known as the Auger process. The energy of an Auger electron may be estimated in the following manner. In Figure 4, the hypothetical energy levels for solid titanium are shown referenced to the Fermi energy $E_F = 0$. The valence bands (V) are relatively broad in comparison to the tightly bound core levels which shift little from their free atom values. The core levels are labeled by x-ray convention. Consider an L level ionization event to occur. An electron dropping from the M level releases an energy of $E_L - E_M$ where the energies are the single

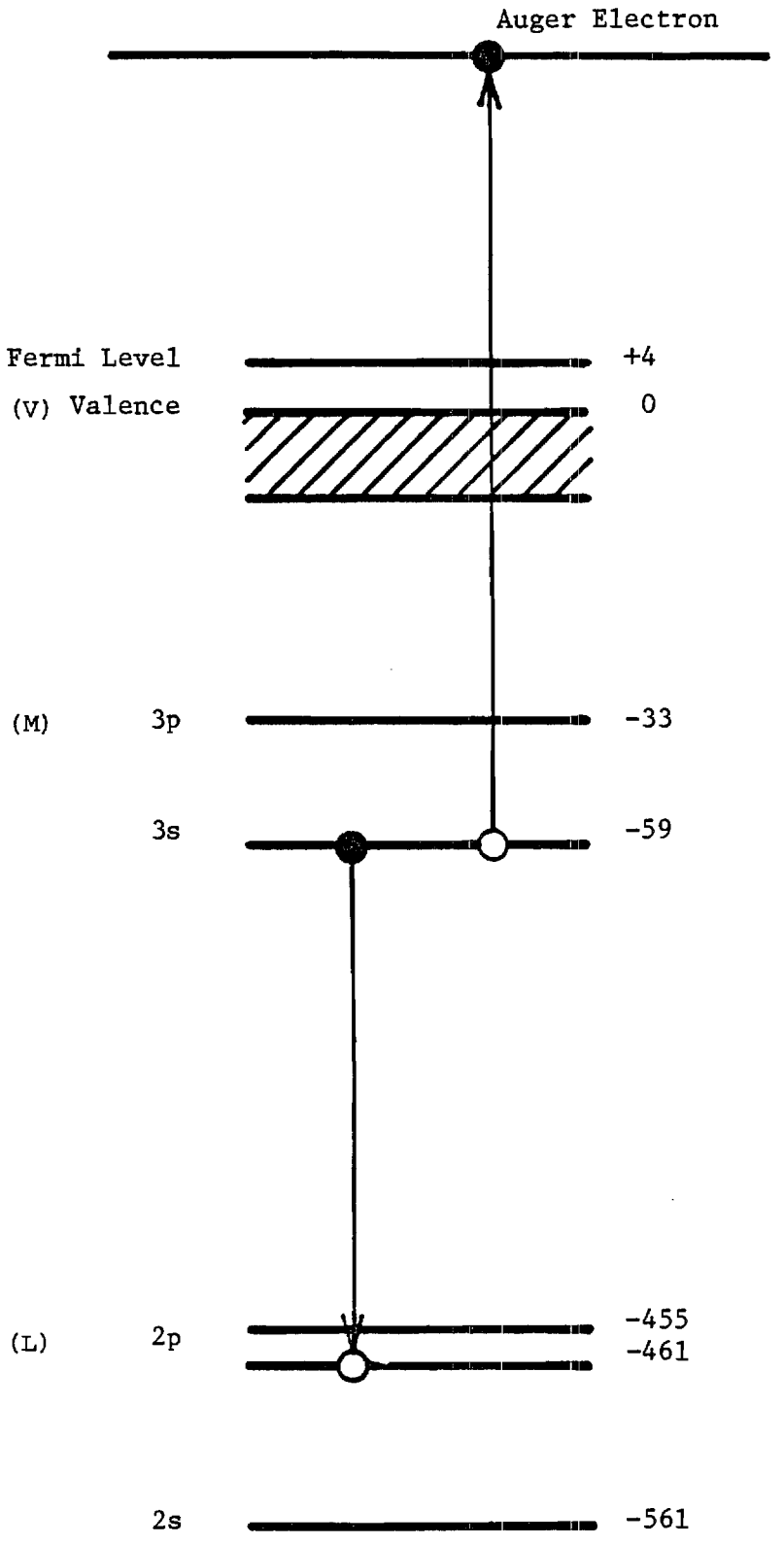

Figure 4. The Auger Process in Titanium

ionization potentials for the atom. The ejected M electron must expend an energy of $E'_M + \phi$ to escape the atom where ϕ is the work function and E'_M is the ionization energy of the now doubly ionized atom and is approximately equal to the ionization energy of the next heavier element [50]. Therefore, the energy of the Auger electron from an atom of atomic number z is approximately given by

$$E_{wxy}(z) = E_w(z) - E_x(z) - E_y(z+\Delta) - \phi \qquad (2\text{-}75)$$

where w is the first level ionized, x is the level that fills the vacancy in w, and y is the source of the Auger electron; Δ is the correction to the atomic number due to double ionization and is approximately one. The Auger electron energies are thus characteristic of the element from which they arise. We note that transitions involving the valence band will reflect the valence band density of states. Also, since chemical bonding will affect the valence band levels, energy shifts can give information on chemical environment [50].

The usefulness of AES as a monitor of surface composition arises from the short mean free path of electrons in the energy range of Auger electrons. Plasma losses and interband absorption cause many Auger electrons to be removed from the observed Auger peaks and instead contribute to the overall background. Empirically determined escape depth data has been used to generate a univeral escape depth curve [51]. In the range of common Auger electron energies, escape depths range from 5A to 20A.

The Auger electron spectrum is superimposed on a large secondary

electron background. The secondary distribution in general has two distinct peaks: a sharp peak produced by elastically reflected primary electrons at the primary electron beam energy and a broader peak at very low energies produced by a cascade effect as the primary beam produces electrons through ionization of the material, which in turn produce more electrons of lower energy through subsequent ionizations. A lower magnitude slowly varying background connects the two peaks. In addition to the Auger peaks in the electron distribution, smaller peaks produced by single and multiple plasmon and interband absorption losses appear at discrete energies below the Auger and the primary elastic peaks.

CHAPTER III

APPARATUS

The requirement of performing optical reflectance measurements over a wide photon energy range on well characterized clean metal surfaces and on in situ grown oxide-metal surfaces provides an interesting challenge to the experimenter. Characterization of the surface is accomplished by monitoring surface chemical composition via Auger electron spectroscopy (AES), while maintaining the sample under stringent ultra high vacuum conditions. Early in this work, measurements were made using apparatus developed by Ellis [52]. This apparatus consists of an ultra high vacuum reflectometer with a spherical grid electron analyzer for AES. Although many useful measurements were made using this apparatus, it was inadequate in a number of respects for measurements on highly reactive titanium surfaces. The major deficiencies were the lack of surface treatment facilities within the vacuum system, the inability to perform optical measurements and AES without lengthy delays between measurements, and the inability to maintain stringent vacuum conditions. As a solution to these problems, a new apparatus was developed featuring: (1) an improved sample chamber and vacuum system, (2) a sample treatment system for cleaning and oxidizing the sample, (3) a computer based data acquisition system for both the optical and Auger spectrometers. Before describing the individual parts of the apparatus in detail, a brief overview of the system follows. The central part of the apparatus, shown schematically in Figure 5, is the ultra high vacuum sample chamber, where the

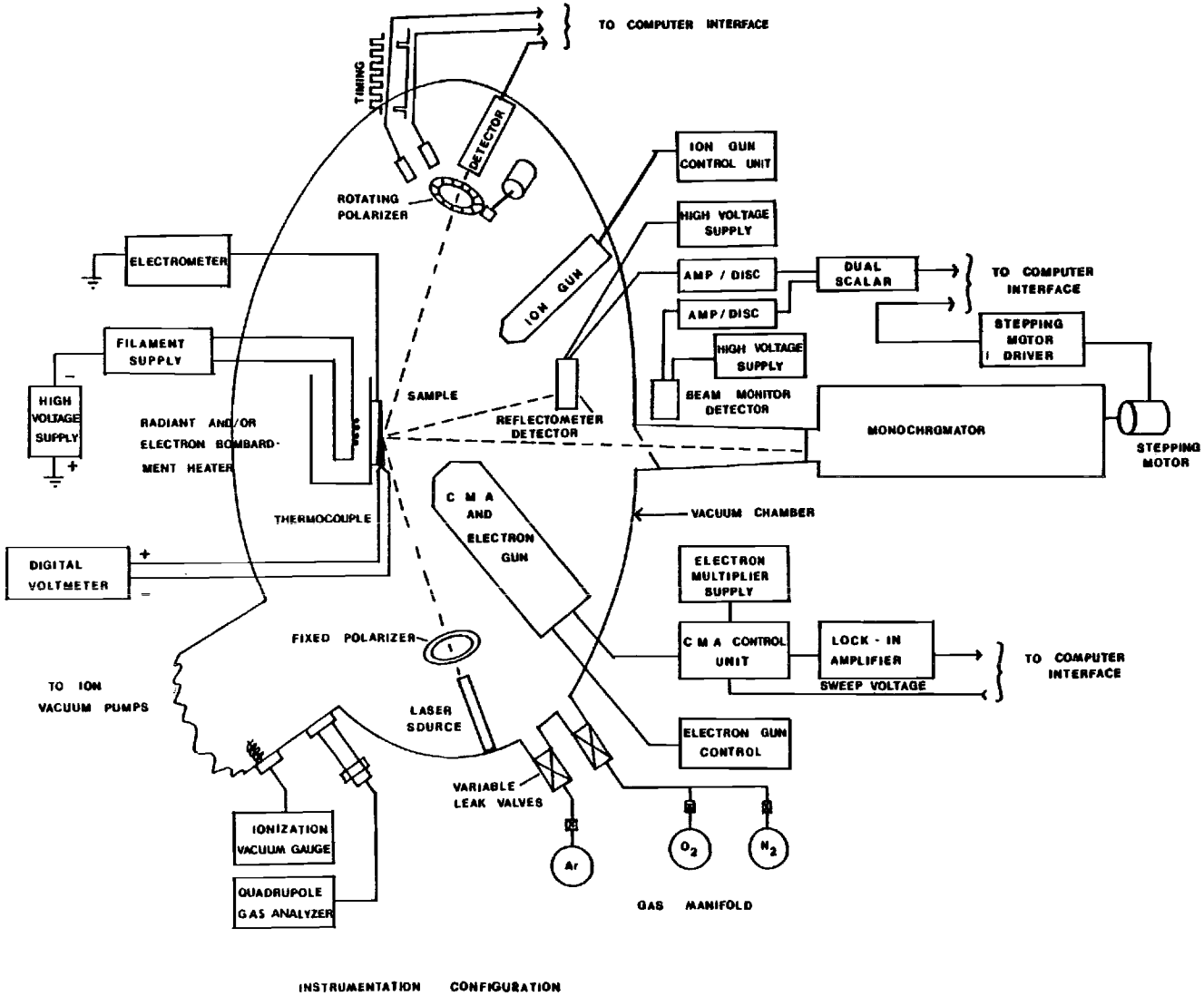

Figure 5. Sample Chamber and Instrumentation

sample is held in the center of the chamber by a high precision manipulator. The chamber has been designed such that both optical reflectance and Auger electron spectroscopy (AES) data may be collected without moving the sample. Reflectance measurements are made with a movable detector within the sample chamber that can rotate about the sample. AES data is collected by a cylindrical mirror analyzer (CMA) located within the chamber. Also within the chamber is an electron bombardment sample heater and an ion gun for sample surface treatment. The chamber is pumped by ion and cryogenic sublimation pumps. A gas manifold for the controlled introduction of high purity gases and a residual gas analyzer is also attached. The monochromator for the reflectance measurements is attached to the sample chamber through an intensity monitor and filter chamber. All of the instrumentation associated with both the reflectometer and Auger spectrometer is controlled by a minicomputer allowing rapid and near simultaneous collection of both types of data. All of the equipment and instrumentation is designed so as to be transportable since the entire experiment is periodically taken to the University of Wisconsin Syncrotron Radiation Center (UWSRC) to make use of syncrotron radiation as the light source in the extreme ultraviolet.

Light Sources and Monochromators

In order to make reflectance measurements over a photon energy range from 2 eV to 50 eV, several light sources must be used. In the visible region of the spectrum (2-3 eV), a 250 W tungsten halogen lamp (Sylvania 250 Q/CL) controlled by a variable voltage transformer is used as the light source. The lamp is used without any focusing optics and

is simply mounted approximately 3 cm in front of the monochromator entrance slit. At wavelengths shorter than 4000 A (approximately 3 eV), light output drops below usable level.

From 3 eV to 11 eV, a hydrogen discharge lamp (McPherson model 630) is used as the source. The lamp is of an open capillary tube design mounting directly to the entrance slit of the monochromator. A continuous flow of hydrogen is maintained by an oil diffusion pump on the monochromator. By differentially pumping the lamp through the entrance slit, an operating pressure of one to two torr may be maintained in the lamp while keeping the monochromator pressure near 10 millitorr. From 3 eV to 8 eV, the hydrogen continuum [53] provides the light source; and from 8 eV to 11 eV, the many lined hydrogen spectrum is used. The ultra high vacuum requirement of the sample chamber dictates the use of a window between the monochromator with a 10^{-2} T pressure and the sample chamber's 10^{-10} T. The cutoff wavelength of the lithium floride window at 1050 A (11.7 eV) is the shortest of any known mechanically rigid material [53] and is the limiting factor in the use of the hydrogen discharge lamp. The lamp is powered by an adjustable regulated DC power supply in series with a current limiting ballast. Typical operating parameters are 800 volts potential between the lamp electrodes and a discharge current of 400 ma. The lamp is water cooled.

The previously mentioned monochromator used with these light sources is a modified General Electric GEI-44854 1 meter normal incidence vacuum monochromator. For wavelengths shorter than 2000 A, the monochromator must be evacuated due to strong atmospheric absorption. This is accomplished by a 300 L/sec oil diffusion pump (CVC type MCF-300)

backed by a mechanical fore pump (Welch model R-1397). The monochromator was modified for this work by removing the drive system and directly coupling a 2000 step per revolution stepping motor (Responsyn HDM-150-2000-8) to the lead screw that rotates the grating. This stepping motor, which is computer controlled, was chosen for two reasons: electrical compatability with a stepping motor driven monochromator used when visiting the UWSRC; and the large number of steps per revolution yielded an acceptable value for the number of steps per Angstrom. For the grating most frequently used (600 lines/mm, 1500 A blaze), the drive arrangement produced in the linear approximation 400 A per revolution or 0.2 A per step. The direct coupling arrangement used minimized backlash in the system; and the error generated in resetting the monochromator to a particular wavelength, approaching from either direction, was less than the 4 A resolution of the monochromator with 250 μ slit widths. The low inertial load of the lead screw allowed full speed starting and stopping of the stepping motor with no overrun. The span of the monochromator is limited by the travel of the lead screw. To prevent the motor from overdriving and damaging the lead screw or the grating mount, two microswitches were mounted adjacent to the lead screw. Triggered by the travel of the lead screw, an overrange or underrange condition provides a stop signal to the stepping motor controller. Using the above mentioned grating, the span of the monochromator is 0-6000 A. The entire monochromator table assembly was supported above the floor by four scissors type automobile jacks, allowing adjustment of the exit slit height and angle to match the sample chamber. Both entrance and exit slits were fixed at 250 micrometer widths, and coupled to the lamp and beam monitor via

O-ring seals. A detailed description of the optics of the monochromator is given by Zivitz [33].

For photon energies greater than 11 eV where windowless operation is mandatory, both the monochromator and light source must be ultra high vacuum compatible. Currently, only one source meets this criterion--synchrotron radiation.

The source of synchrotron radiation used in this work is Tantalus I, the 240 MeV electron storage ring at the University of Wisconsin Synchrotron Radiation Center. Briefly, in storage rings electrons are accelerated centripetally in a magnetic field by the $\vec{v} \times \vec{B}$ force, causing them to radiate in a continuum from the far infrared to the extreme ultraviolet. In order to maintain a stable orbit, radiation energy losses are compensated for by boosting the electron's energy in a radio frequency cavity. The radiation is directed in a narrow cone along the electrons instantaneous velocity vector; thus observing in the orbital plane of a storage ring, one would see a bright point of light at the tangent point of the circular orbit. The radiation is strongly polarized with the electric vector in the plane of the orbit. Radiation intensity is directly proportional to the storage ring beam current. The wavelength at which maximum intensity occurs is a function of the beam energy. In the case of Tantalus I, maximum intensity occurs near 260 A with usable intensity from approximately 50 A to the infrared. Typical beam currents at the time of injection were near 100 ma. The current decays to about 20 ma over a period of several hours due to electron scattering with residual gas in the storage ring and electron-electron interactions. In Figure 6, light from the storage ring is directed by grazing incidence

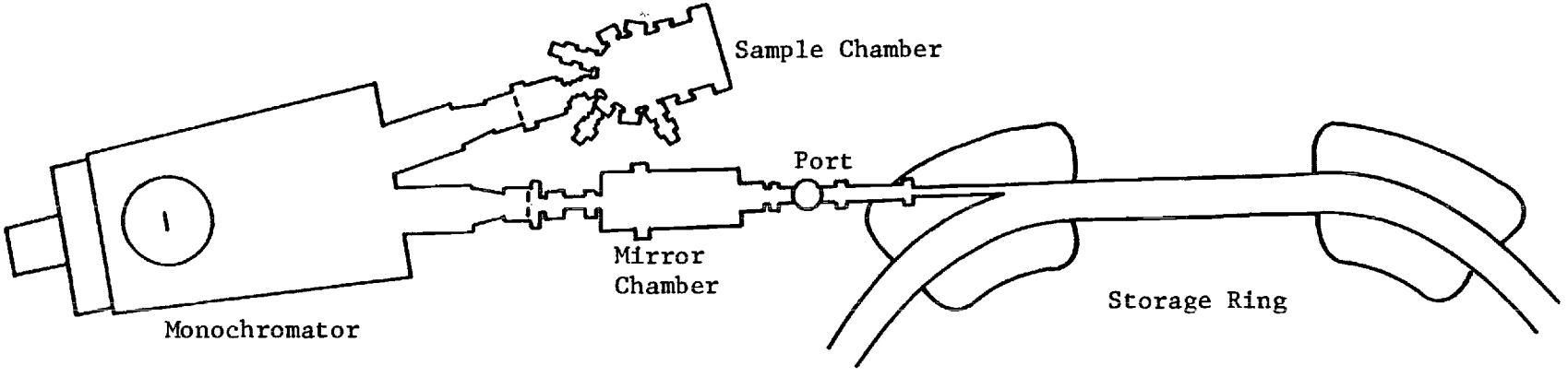

Figure 6. Experimental Arrangement Used at UWSRC

mirrors through UHV tubing and focused on the entrance slit of the monochromator. The monochromator used is a 1 m normal incidence instrument designed by Pruett and Lien of UWSRC [54]. Wavelength selection was accomplished by rotating the grating via a stepping motor. A second stepping motor provided linear focusing of the grating. In practice, a median setting for the focus control was sufficient for each wavelength region investigated. The monochromator range was from 0-2500 A, though low reflectivity and scattering of the grating limits the shortest wavelength investigated to 250 A. Sliding valves with quartz windows were built into the monochromator at the slits to facilitate coupling and alignment of the users experiment while maintaining vacuum in the monochromator and mirror chambers. Pressure in the monochromator was limited to 10^{-8} Torr due to the use of O-ring seals and the inability to adequately bake the system. A more detailed description of the storage ring facilities is given by Ellis [52].

The Beam Intensity Monitor

A potential source of major error in reflectance measurements are the fluctuations with time in the intensity of the source. The fluctuations may be long term, such as the monotonic decay of intensity in the electron storage ring due to loss of electrons to scattering processes; or short term, such as "flicker" instabilities in the hydrogen lamp discharge. Previous experimenters [33,52] minimized this problem through the use of regulated power supplies for the sources; hoping that short term instabilities would "average out;" and in the case of synchrotron radiation, normalizing the measurements to the storage ring beam current. However, problems persisted; slight sagging of an incandescent filament,

or movement of the electron beam in the storage ring could produce changes of several percent in the measurements. Similarly, when using the many lined hydrogen spectrum, variations of several orders of magnitude existed between being "on" an emission line and being "off" it. When comparing reflected intensities with previously measured incident intensities, a slight error in the positioning of the monochromator would produce large errors in the measurement.

The most promising solution to these intensity fluctuation problems is to continuously monitor a portion of the light entering the sample chamber after it exits from the monochromator. Such a device was constructed. Machined from a single piece of type 304 stainless steel, the body of the intensity monitor is shown in Figure 7. One end of the monitor has a 6 inch flat vacuum flange compatible with the O-ring seals on both monochromators; the other end has a 2-3/4 inch knife edge type UHV flange with tapped 1/4-28 bolt holes. The optical path is a 3/4 inch diameter bore between the front and rear flanges. Midway between these flanges a 1-1/4 inch bore intersects the optical path at right angles. A 2-3/4 inch UHV flange located at the bottom of the 1-1/4 inch bore allows a filter holder assembly to insert low pass filters in the optical path. A recessed 2-3/4 inch UHV flange is recessed in the top of the machine monitor for mounting a window just above the optical path. Located just below the window and in the optical path is an aluminum plate, mounted at a 45° angle. At a point in the plate that is the center of the optical path, a .035 inch aperture allows a portion of the light to pass through the monitor and into the sample chamber. This aperture acts as a collimator, limiting the size of the light beam falling on the sample. The

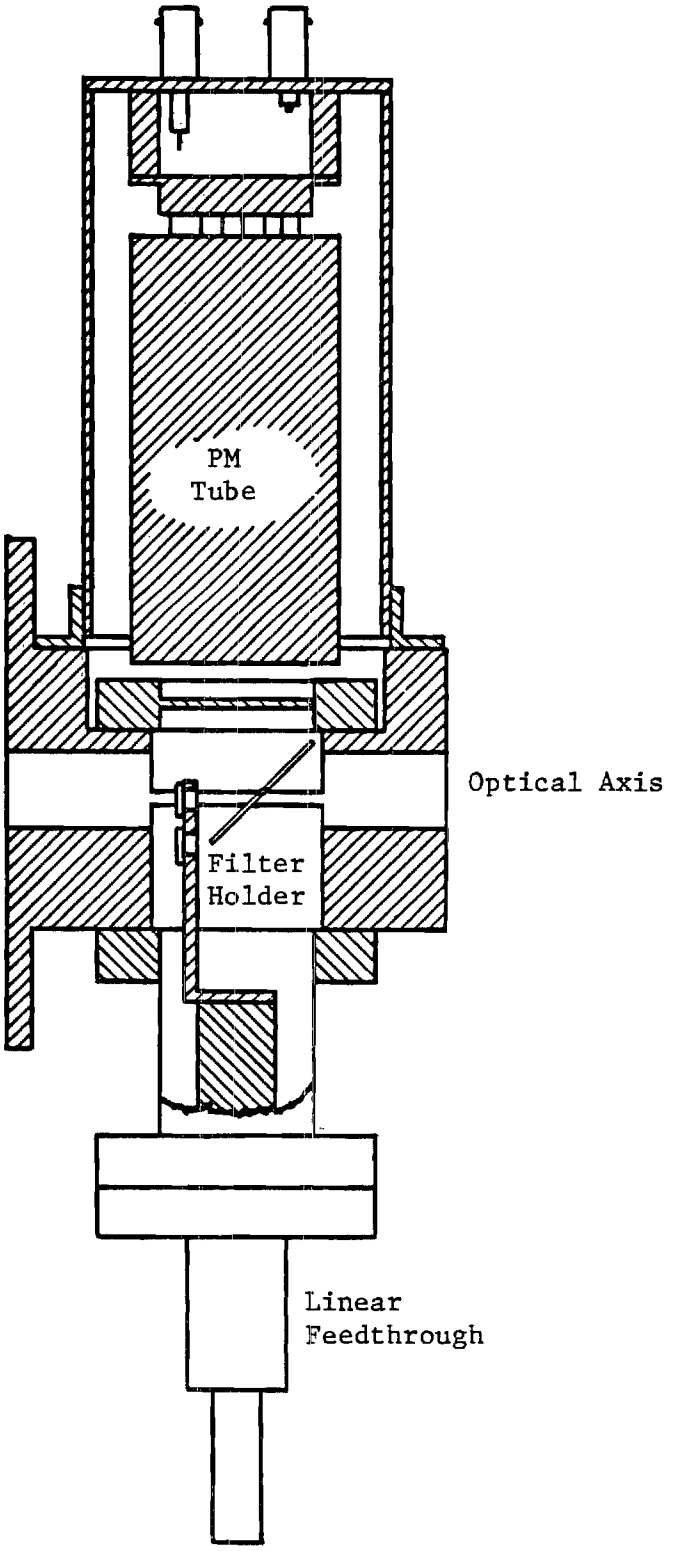

Figure 7. Cutaway View of the Intensity Monitor

top portion of the plate that intercepts the remainder of the light is coated with the phosphor sodium salycilate ($N_aC_7H_5O_3$). Ultraviolet light from the monochromator is wavelength shifted to the visible by the phosphor where it may be detected by a photomultiplier tube mounted above the window. In the case of visible light from the monochromator, the phosphor simply acts as a diffuser, reflecting light to the photomultiplier tube. The phosphor coated plate is made of aluminum because sodium salycilate breaks down in the presence of iron [55], eliminating stainless steel from use here. The aperture plate is located approximately 7.5 cm from the exit slit. The ruled area of the gratings on both monochromators is 96 mm by 56 mm and if fully illuminated by the source, an area of ~ 7 mm x 4 mm will be illuminated on the aperture plate. The area of the aperture itself is 0.62 mm^2, yielding a ratio of light monitored to light transmitted of 45 to one. The photomultiplier tube (EMI 9502S) is in an aluminum housing that threads onto the main body of the monitor, viewing the aperture plate through a 2-3/4 inch Varian viewing port. The distance between the photomultiplier tube and the aperture plate is one inch. Two 1 cm diameter by 2 mm thick filters, one of quartz and the other of lithium fluoride, are epoxied to a 5/8 inch by 2 inch filter holder. The filter holder is mounted to a linear motion feedthrough (Ultek 282-6100) that allows either of the filters to be inserted into the beam just forward of the aperture plate. The filters are used for eliminating high order light from the monochromator, with the LiF filter having a cutoff of 1050 A and the quartz filter, 1600 A. The monitor chamber connects to the sample chamber via a bellows type flexible UHV coupling. When operating in the extreme UV, the windowless region, the

monitor chamber is pumped by both the sample chamber and the monochromator; at longer wavelengths a LiF window is placed between the flexible coupling and sample chamber, leaving the monochromator to pump the monitor chamber.

The Sample Chamber

The sample chamber, constructed entirely to type 304 stainless steel, was designed by J. Larsen and the author, and manufactured by the Ultek Corporation. The basic shape of the chamber, shown in Figure 8, is an 8 inch diameter elbow having 10 inch O.D. knife edge UHV flanges. The reflectometer apparatus mounts on a ten inch flange that mates with the top of the elbow. A Varian high precision sample manipulator is mounted on the reflectometer flange holding the sample centered vertically in the sample chamber, approximately 6-1/2 inches below the top flange. Seven 1-1/2 inch ports with 2-3/4 inch flanges spaced 30° apart are welded into the chamber such that center lines drawn through each port intersect at the sample position. The sample to flange distance is 5 inches. Below the sample a 4 inch port with a 6 inch flange, for mounting the CMA, is welded into the chamber 19° off the vertical axis with its center line also intersecting the sample position. A 6 inch port connecting to the vacuum pumps, with two 1-1/2 inch ports on either side, is welded into the bottom arm of the elbow. The 10 inch flange at the "rear" of the elbow is blanked off, reserved for future additions to the system such as LEED apparatus.

The seven 1-1/2 inch ports allow great flexibility in the experimental arrangement. The central port couples to the intensity monitor,

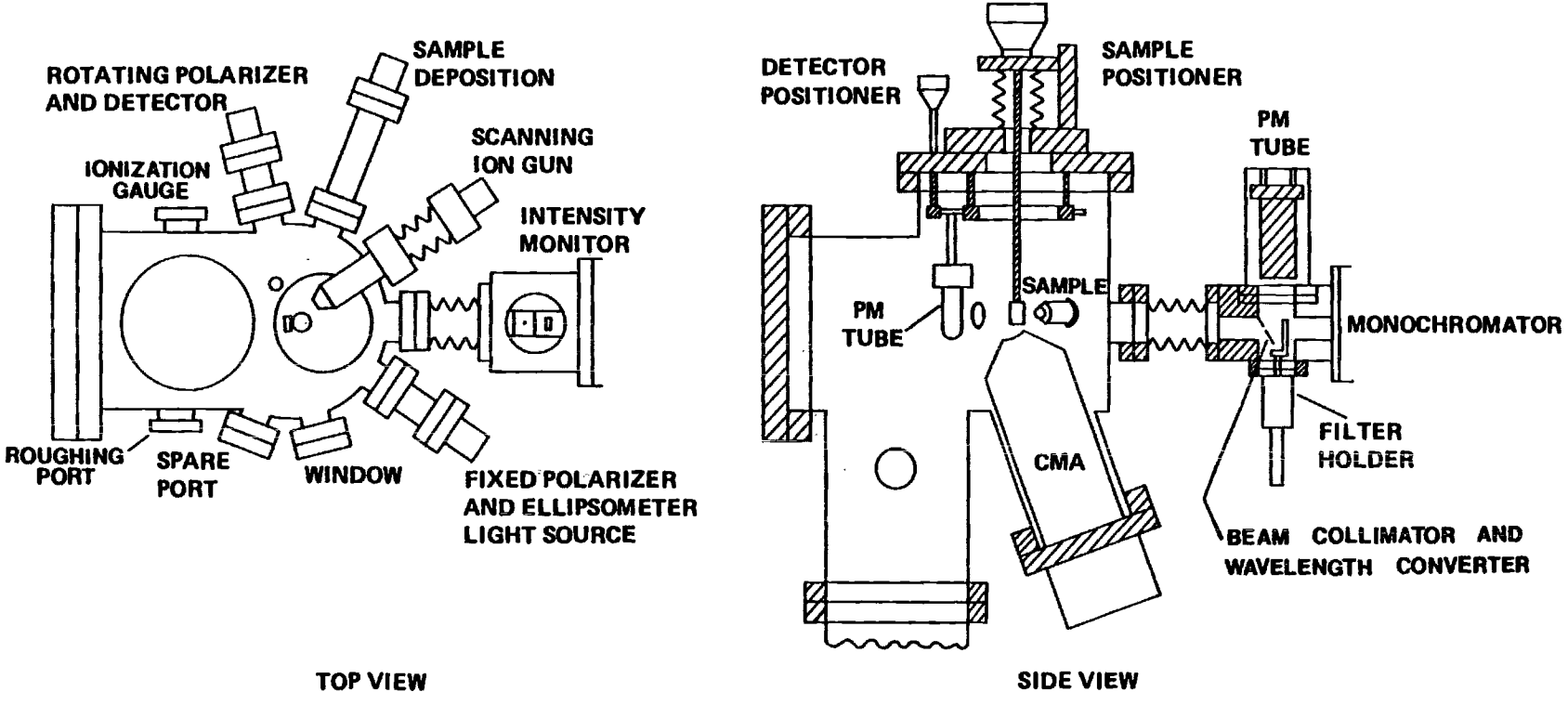

Figure 8. Sample Chamber Cross Section View

providing the light source for the reflectometer. A 3 KeV ion bombardment gun (Varian model 981-2043) is mounted in an adjacent port. An extension to the port is necessary since the gun is six inches long and the reflectometer requires a clearance of 3-1/4 inch radius around the sample. Two ports 120 degrees apart are reserved for the future addition of an infrared/visible ellipsometer. Another port connects to a residual gas analyzer (Varian UGA-100 Quadrupole). Windows are fitted to the remaining two ports allowing visual alignment of the sample. The high purity gas manifold and an ion vacuum gauge are attached to the two 1-1/2 inch ports on the pumping port.

The sample chamber is pumped by two 140 L/sec differential diode ion pumps (Ultek 206-1500), and a titanium sublimation pump (Ultek 214-0410) surrounded by a liquid nitrogen cooled shroud (Ultek 214-2001). The two ion pumps are mounted on opposing sides of a standard 6 inch vacuum "cross" with the sublimation pump protruding into the cross from the third port. A 4-1/2 inch circular baffle was cut from .030 inch stainless steel sheet and spot welded using four equally spaced mounting tabs one inch above the cylindrical sublimation pump shroud. The baffle and cross eliminate a line of sight path between the pumps and sample chamber, which is connected through a 6 inch gate valve (Varian 951-5076) to the fourth port of the cross. The lack of a line-of-sight path minimizes sample chamber contamination due to titanium sputtering in the pumps. The pumps are mounted on a heavy steel plate base described by Ellis [52] with the sample chamber supported by the pump assembly. A carbon vane rotary pump (Gast 0322-V103-G8D) along with two liquid nitrogen cooled sorption pumps (Varian 941-6501), all mounted on a

portable cart serve as an oil free roughing pump. The roughing system connects to the sample chamber through a stainless steel flexible hose and a gold sealed UHV valve attached to the gas manifold.

The sample chamber and pump assembly are wrapped with ten 290 watt heating tapes in addition to separate heaters for the ion pumps. These heaters, controlled by a variable voltage transformer, allow baking the system to above 250°C. A timer on the control unit provides for overnight baking with automatic shutoff in time for the system to cool for next morning operation.

The Reflectometer

An optical detector that can be rotated about the sample at a fixed radius forms the basis of the reflectometer. The reflectometer assembly shown in Figure 9 is constructed on a 10 inch O.D. blank Varian conflat flange (Model 954-5084). A four inch hole is cut through the center of the flange to allow clearance for the sample manipulator and related components. An UHV seal designed to mate with the 6 inch O.D. flange on the sample manipulator is machined in the top of the reflectometer flange. Four lengths of 3/4 inch O.D. S.S. tubing which have miniconflat flanges welded on one end were then welded into four holes machined in the reflectometer flange. The holes are equally spaced on a circle and at an angle of 27° outward from the flange center line. The angular cut was necessary for the mini flanges to clear the sample manipulator on top and the chamber walls on the bottom. Five support rods are welded to the bottom of the reflectometer flange. Four of the rods support the rotatable detector mount and the fifth rod supports the drive

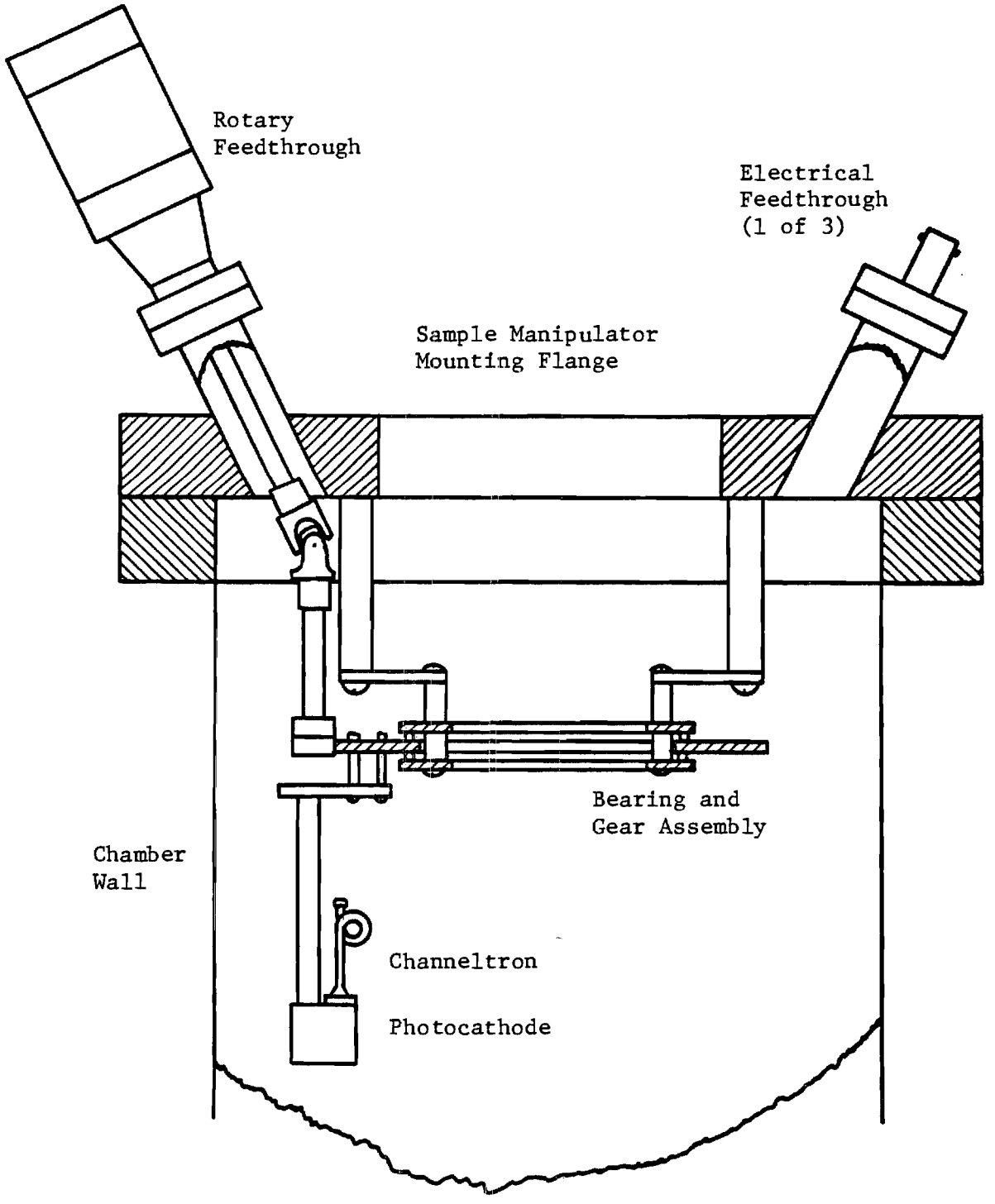

Figure 9. The Reflectometer With a Single Detector Mounted

assembly. A five inch diameter gear with a three inch bore is sandwiched between a pair of 3-3/8 inch diameter, 2-1/2 inch bore, flat rings. Both the gear and rings have 3-3/16 inch mean diameter bearing races machined in their opposing surfaces; each race is filled with a full complement of gold coated, 1/8 inch diameter, stainless steel balls. Eight spacers, fitting through the bore of the gear, hold the entire assembly together. The rings are attached to the four support rods on the reflectometer flange by mounting brackets. The five inch gear is a 48 pitch, 14° pressure angle, 1/8 inch thick spur gear with three equally spaced pairs of tapped 6-32 holes on a 2-1/8 inch radius from the center for the mounting of detectors. The gear is machined of type 6061 aluminum which was used in this instance because of difficulty in maching a stainless steel gear of these dimensions. Type 6061 aluminum is generally approved for UHV applications [56]. The balls in the bearings were gold coated by evaporation to minimize the possibility of vacuum welds during rotation. The five inch gear is driven by a 1/2 inch diameter, 3/16 inch thick pinion on the lower end of a 1/4 inch diameter shaft which is supported by a pair of 1/2 inch O.D. ball bearings mounted to the fifth support rod. The upper end of the shaft couples to an UHV rotary motion feedthrough (Varian 954-5146) mounted on one of the four miniconflat flanges. The two shafts are coupled through a universal joint to allow rotation through the 27° angle made by the shafts. All components, except for the five inch gear, are constructed on types 304, 316, or 441 stainless steel. Standard UHV construction and cleaning practices were followed including heliarc welding, with all welds made on the vacuum side of vacuum-air interfaces wherever possible.

Two detectors are mounted below the five inch gear so that their photosensitive surfaces are 6-1/2 inches below the reflectometer flange in the horizontal plane of the light from the monochromator, and approximately 1-3/4 inches from the sample. As shown in Figure 10, each detector may be rotated into position for measuring either the incident beam intensity (sample lifted out of the beam path) or reflected beam intensity. The finite size of the detectors and beam limit the "near normal incidence reflectivity" to 5°-7° off normal. The divergence of the light beam, after passing through the collimating aperture, produces a spot size of approximately 4 mm diameter at the sample and 4.5 mm at the detector. Since rotation is centered around the sample surface, the light path is the same length for both incidence and reflectance measurements.

While several different detectors were tried during the course of this work, the most satisfactory was found to be a miniature side window photomultiplier (Hamamatsu R889 photomultiplier, which is a 1/2 inch diameter, 2-1/2 inch long, 9 stage tube with a multialkali ($Na\text{-}K\text{-}S_b\text{-}C_s$) photocathode) for use in the visible and near UV. The active area of the photocathode is a rectangle 4 mm wide by 23 mm high. The large vertical dimension of the cathode increases the tolerance in the vertical positioning of the detector, an adjustment that must be made within the vacuum system. The tube features a UV transmitting glass envelope giving a spectral response extending from 1850A to 8500A. The resistive voltage divider chain for the tube is constructed from Corning thin film glass resistors (PVV60 1M ± 1%) with nickel leads that are spot welded together to form the chain. These resistors, proven to have excellent UHV characteristics, are mounted just above the tube in the vacuum system.

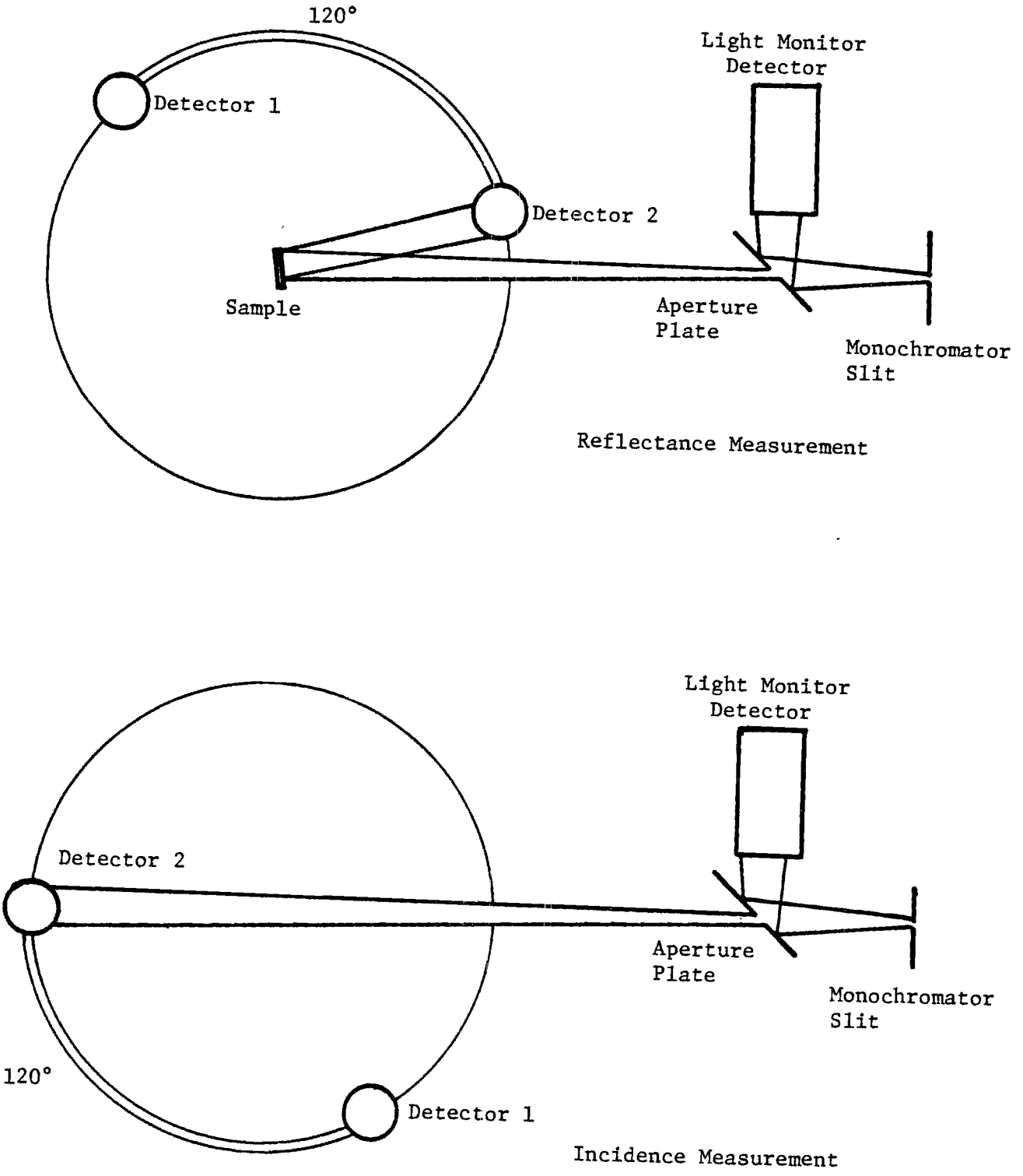

Figure 10. Reflectometer Optical Path

The large resistance value for the divider chain limits the power dissipation of the chain to ~100 milliwatts, minimizing heating of the PM tube and subsequent increase in dark current. The smaller divider chain current does not appreciably affect the linearity of response of the tube since it is utilized in the single photon counting mode. The tube and resistor chain are supported by .065 inch stainless steel rods, also serving as electrical leads, mounted to a stainless steel plate by ceramic insulators. Four bolts adjust the height of the plate, while attaching it to the rotating gear assembly. Electrical connections are made by flexible copper leads insulated by woven fiberglass sleeves to feedthroughs mated with the three remaining miniconflat flanges.

For detection of photons with wavelengths shorter than the cutoff of the PM tube, a nude nickel photocathode is coupled to a channel electron multiplier (channeltron). The channeltron (Galileo Model 4028C) is a spiraled, hollow, glass tube coated on the inside with a partially conducting tungsten film. One end of the tube has an eight mm diameter cone while the other end has an electron collecting cap. The tungsten surface has a secondary electron yield factor of greater than one, so that an electron entering the cone of a properly biased channeltron produces a cascade of electrons at the collector. The channeltron has a gain of 10^8. Work by Ellis [52] and earlier work by the author [57] used the channeltron without a separate photocathode using the channeltron cone as the photocathode. Two problems with this arrangement suggested a change: First, the work function of tungsten produced a long wavelength limit of ~1700A leaving a gap in the measurements between 1700A and the 1850A cutoff for the PM tube; and secondly, the geometry of the cone

produced a spatially nonuniform distribution in the photoemission sensitivity of the detector, providing a source of error in the intensity measurements due to the positioning of the detector. The solution to these problems was the construction of a separate photocathode from nickel sheet. Nickel was selected for the stability of the surface under repeated exposure to the atmosphere, high photoemissivity extending to wavelengths as long as 2500A [58], and easy fabrication of the cathode. The nickel cathode shown in Figure 11 was designed to improve its efficiency by providing a "light trap," while keeping the construction simple. An aperture in the top of the closed cathode allows the channeltron cone access to the photoemitted electrons. The cone is kept at ground potential while the cathode is biased at -300V providing a potential gradient attracting electrons into the cone. A glass ring insulates the cone from the cathode. Light enters the cathode through a one cm square opening in the side of the cathode. The opening is covered with a 100 mesh tungsten grid to provide an equipotential surface within the cathode. Multiple light reflections within the cathode improve the overall efficiency of the unit. The cathode and channeltron are spot welded to stainless steel support rods that serve as the electrical connections to the detector. The support rods are mounted through ceramic insulators to a stainless steel plate, which in turn is bolted to the rotating gear assembly as previously described.

In operation, the PM tube is used in the spectral region from 6000Å to 2000Å, and the channeltron from 2000Å to 300Å, or shorter. One serious shortcoming of this detector arrangement is the upper temperature limit of 50°C for the PM tube. Above this temperature the cesium

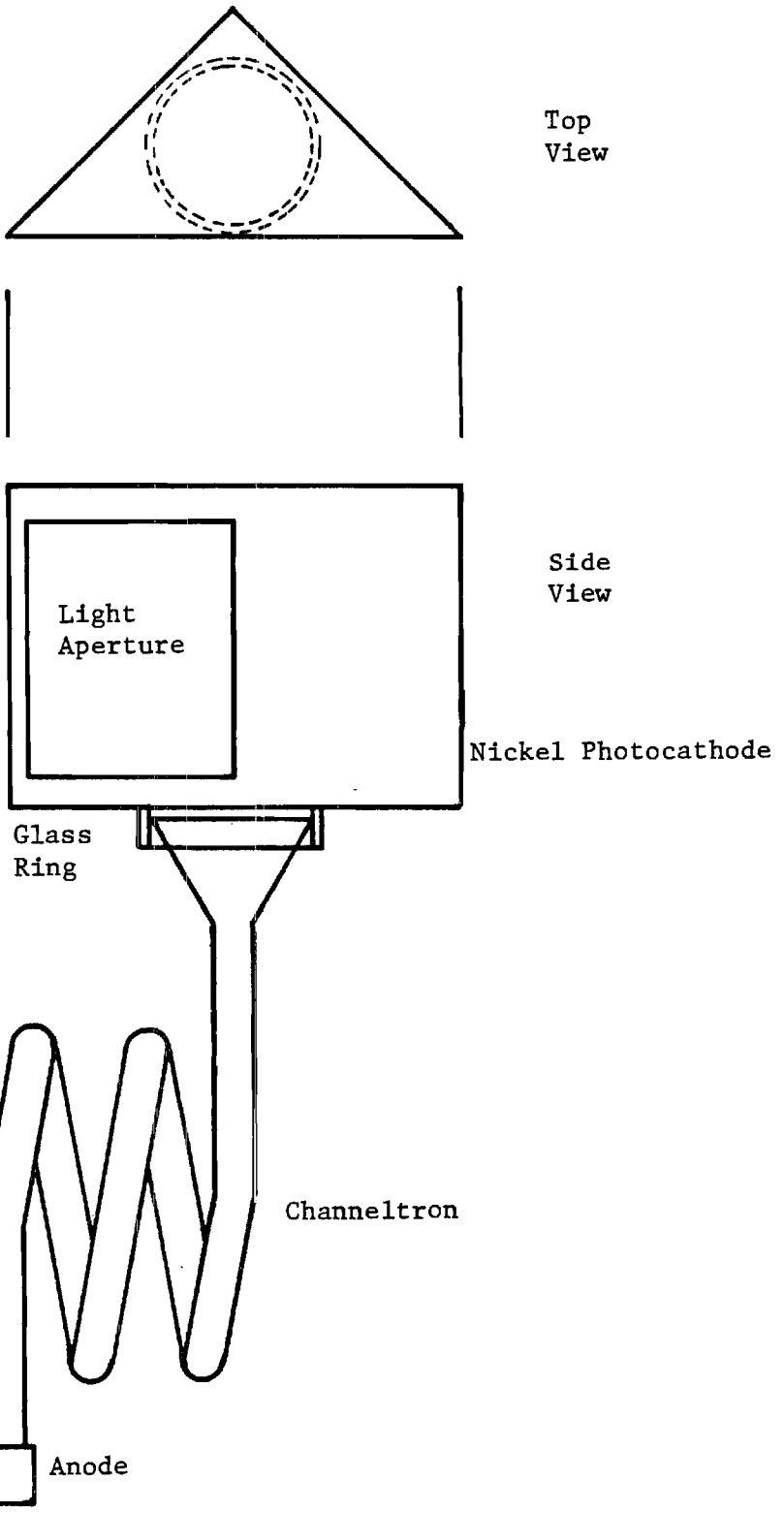

Figure 11. Nickel Photocathode and Channeltron

in the photocathode sublimes, rendering the tube useless. This temperature limit prevents adequate baking of the vacuum system with the reflectometer installed. In practice, many measurements were limited to above 2000Å, using only the channeltron in the vacuum system. When both detectors are used, the system is first baked without the reflectometer installed; the system backfilled with dry nitrogen; and then the reflectometer is installed and the system repumped. Under fully baked conditions, ultimate system pressure is approximately 5×10^{-11} Torr, while with the system "pre-baked" the pressure may be an order of magnitude higher.

The Auger Spectrometer

The heart of the Auger spectrometer is a Physical Electronics Corporation cylindrical mirror analyzer (CMA) model 10-155 with built-in axial 5 KeV electron gun. A CMA is a bandpass electron energy analyzer that consists of two concentric conducting cylinders. A variable voltage source provides a potential difference between the two cylinders. As shown in Figure 12, electrons emitted from the sample (located near one end of the cylinders) and having a kinetic energy of ~1.76 times the potential difference on the cylinders will be focused on an electron multiplier axially mounted near the far end of the cylinder. Only electrons within a very narrow range of energies will travel a trajectory leading to the electron multiplier. Varying the cylinder, potential changes the energy of the accepted electrons in a linear manner. The bandwidth of the analyzer is a function of the size of the detector aperture, the exactness of the geometry of the cylinders, and the

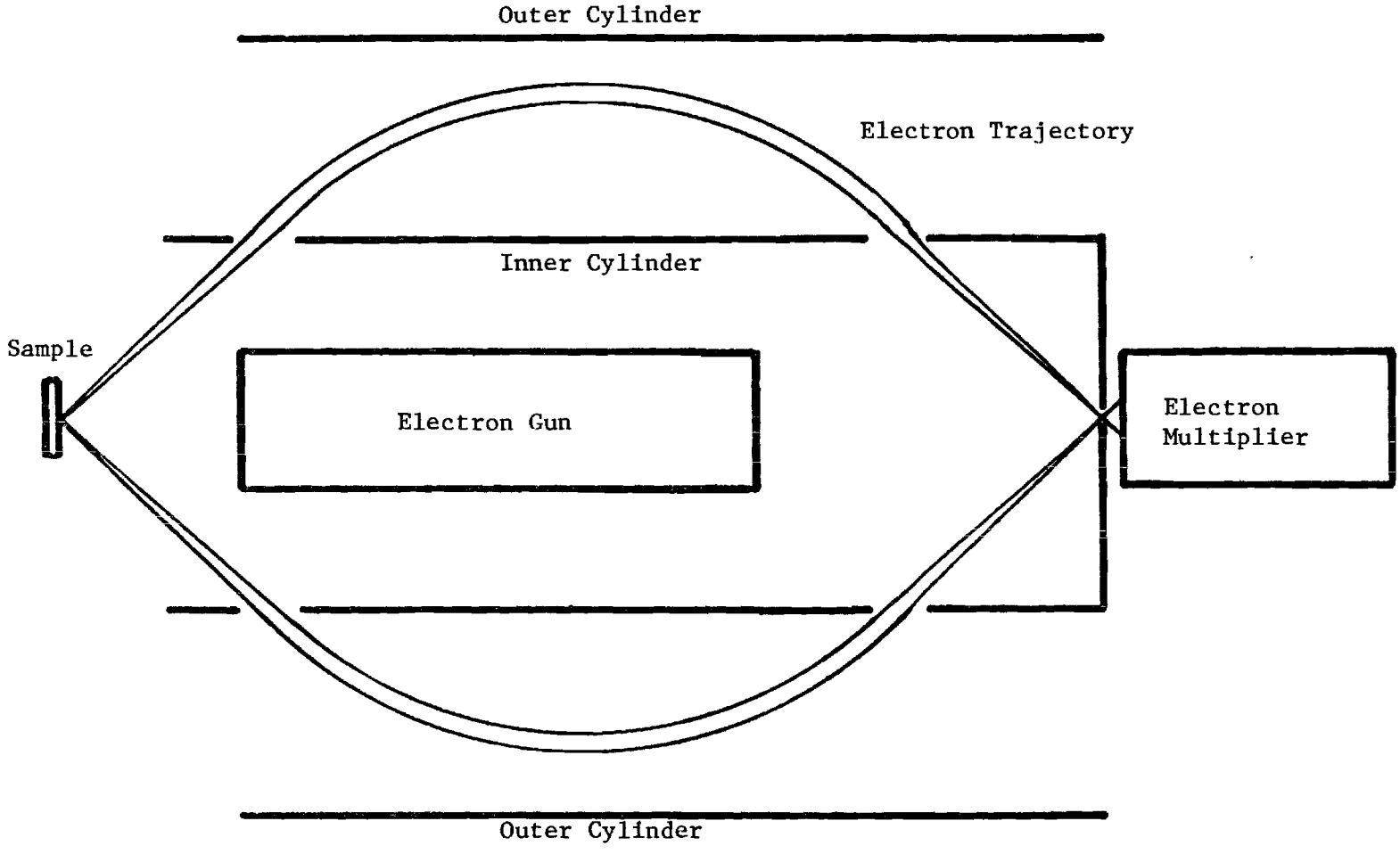

Figure 12. Cylindrical Mirror Analyzer Optics

position and effective source size of the sample. The CMA used in this work has a passband width of less than 0.6% of the passband energy with a transmission coefficient of 10%. An electrostatic and magnetic shield surrounds the CMA. The positioning of the sample is critical since it affects both the energy calibration and resolution of the CMA. The sample is centered 6.5 mm in front of the aperture in the conical shield of the CMA. The close proximity of the CMA to the sample coupled with the requirement that optical and Auger measurements be made with minimum equipment reconfiguration or sample movement dictates that the CMA must be located at an angle far from the sample normal to insure that the incident and reflected light is not intercepted by the CMA shield. Therefore, the CMA is mounted below the sample, making a 19° angle with the sample surface in the direction of the monochromator entrance. The entrance aperture of the CMA forms a hollow, cone-shaped acceptance region for electrons that is centered on the sample face. The cone's angle is 42.3° from the CMA axis and about 6° wide. As illustrated in Figure 13, part of the acceptance cone is occluded by the sample surface; with only 224° of the 360° cone visible, the effective transmission of the CMA is reduced from 10% to 6.2%. A second effect of the shallow angle is to reduce the average angle of emission of the detected electrons, increasing their effective depth in the sample which increases the relative surface sensitivity of the process [51]. A third effect is a loss of resolution due to the increase in size of the electron excited region of the sample along the CMA axis due to the shallow angle that the electron beam makes with the surface. When optical measurements are not being made, the sample may be rotated, aligning its normal with

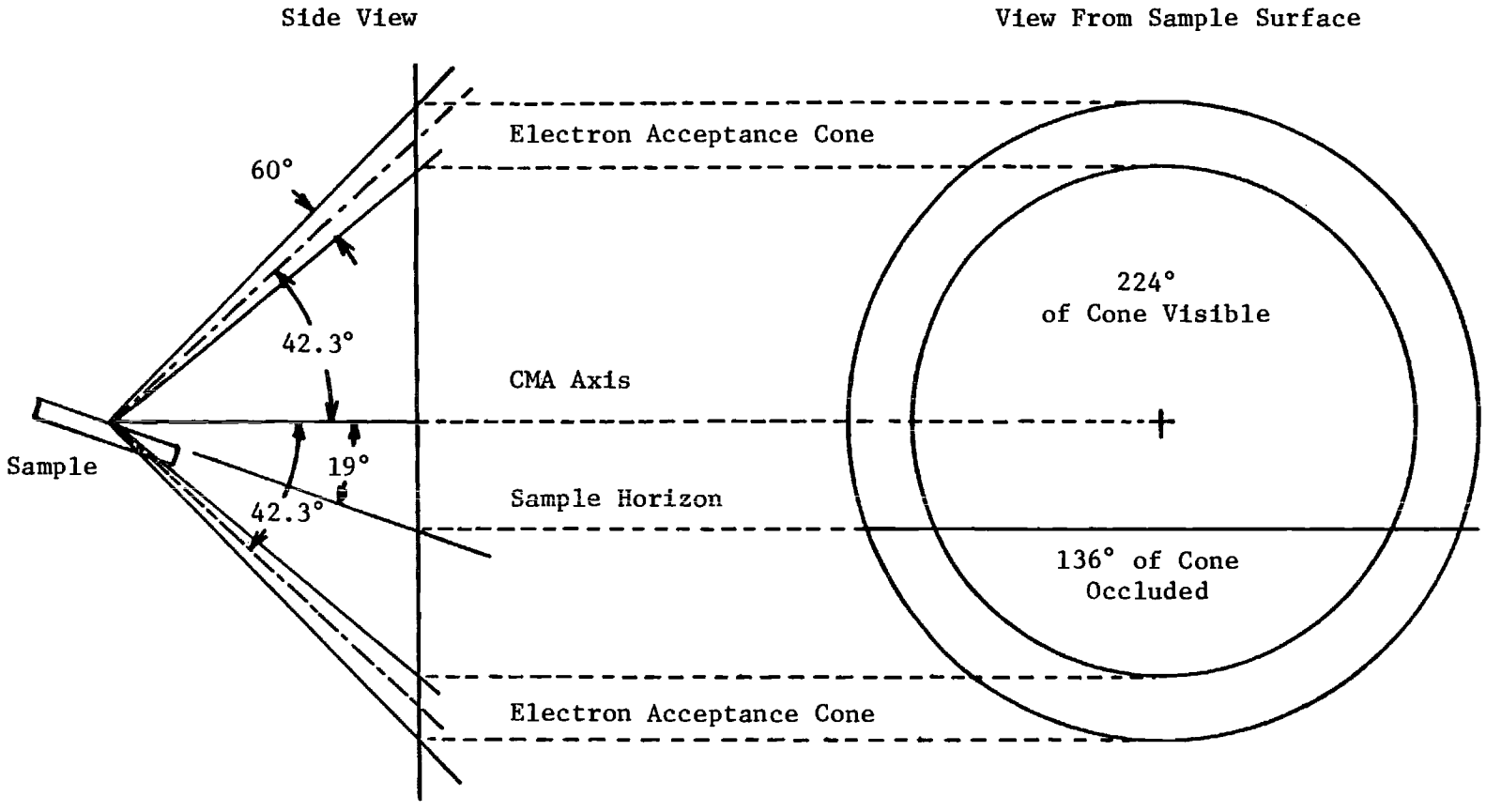

Figure 13. Occlusion of the CMA Acceptance Cone

the CMA axis, to improve the resolution and transmission of the system.

The Sample Manipulator

Positioning of the sample is accomplished with a Varian high precision manipulator (Model 521-0523). The manipulator provides translation along the x, y, and z axes with a repeatability of 0.1 mm for x and y, and 0.5 mm along the z axis. The manipulator also has the capability of a 360° rotation about the z axis with a resolution of 0.1°. The manipulator is built into a 6 inch O.D. UHV flange with six mini-conflat flanges for electrical feedthroughs. The manipulator mounts to a mating seal cut into the center of the reflectometer assembly.

Two types of sample holders attach to the manipulator mounting shaft. The most flexible mount is the Varian flip mechanism assembly which provides for a 100° rotation about an axis perpendicular to the z axis. This assembly has a built-in indirect resistance type sample heater and sample mount. The addition of a chromel-alumel thermocouple to the side of the sample mount is the only modification to the unit. The only disadvantage of this assembly is the required configuration of the sample--a 6.2 mm diameter disc with a 7.8 mm diameter lip for mounting. The total thickness of the sample is 1.5 mm with the lip extending to half that thickness. The small sample size introduces difficulty in the system alignment because the light beam from the monochromator is nearly the same size; however, with five degrees of freedom in the manipulator, the sample can be aligned under vacuum.

The second mounting arrangement is for larger samples, holding up to 2 cm diameter samples on the front of a small molybdenum box

containing a tungsten filament. The filament is electrically isolated from the sample (and box) allowing a negative potential on the filament for electron bombardment of the sample. A chromel alumel thermocouple mounts to the edge of the sample. Sample temperatures of 700°C can be obtained using this method. This mount has no provisions for rotation perpendicular to the vertical, therefore, the sample must be aligned prior to placing it in the vacuum system.

The Gas Manifold

Controlled amounts of high purity gases may be introduced into the vacuum system for reaction with the sample by use of a gas manifold shown schematically in Figure 14. The manifold connects to the vacuum system through a standard 1-1/2 inch O.D. UHV cross. Two of the ports on the cross mate to two variable leak valves (Varian 951-5100) which connect to two independent gas lines. One gas line is attached to an argon bottle, used for surface sputter cleaning; the other line connects to an oxygen bottle, a nitrogen bottle, and, through a valve, to a spare bottle position. The gases used are Matheson Research grade (N-99.9995%, O-99.99%, Ar-99.9995%) in #7 cylinders (lab bottle size), initially pressurized to 225 lbs/in^2. Another valve in each gas line connects to a common port for roughing and purging the gas lines. The gas lines are 1/4" O.D. stainless steel tubing with stainless steel fittings and valves. The valves have diaphragm seals, eliminating leaks around the stem packing. Prior to use, the lines are evacuated by the roughing pump system; the leak valves may then be opened to the sample chamber to further purge the lines. Closing the leak valve and opening the appropriate

cylinder valve for a short period of time pressurizes the gas line. A regulator is not used between the cylinder and leak valve since the leak valve can withstand up to 500 lbs/in^2 inlet pressure. The use of greater-than-atmospheric pressure in the gas line minimizes inward leaks of contaminants into the system. Two separate gas lines are more convenient and provide faster turn-around times since surface sputter cleaning is often used prior to introduction of reactive gases.

Connected to the third port on the manifold cross is a standard 1-1/2 O.D. UHV "Tee" with a 20L/sec triode ion pump (Varian 911-4030) on one port and a gold sealed UHV valve on the other. The valve is used as the roughing port for the sample chamber. The ion pump provides a small amount of continuous pumping during exposure of the sample to gases; by maintaining a continuous flow during exposure, the purity of the gas may be maintained since contaminants outgassing from the vacuum system are continuously pumped away.

Instrumentation

Instrumentation for both the reflectometer and Auger spectrometer is controlled by a DEC PDP-8/L minicomputer using interfaces and software developed during this work. The PDP-8/L is a one address, 12 bit, parallel computer with an internal 4096 work (4K) memory. An external 4K of memory with memory controller (DEC MC8/L) provides a maximum memory capability of 8K. The memory cycle time is 1.6 microseconds, with each computer instruction requiring one, two, or three memory cycles, depending on function. The limited memory of 8K necessitates the development of the control program in assembly language in order to conserve memory for both the program and data storage. The control program is

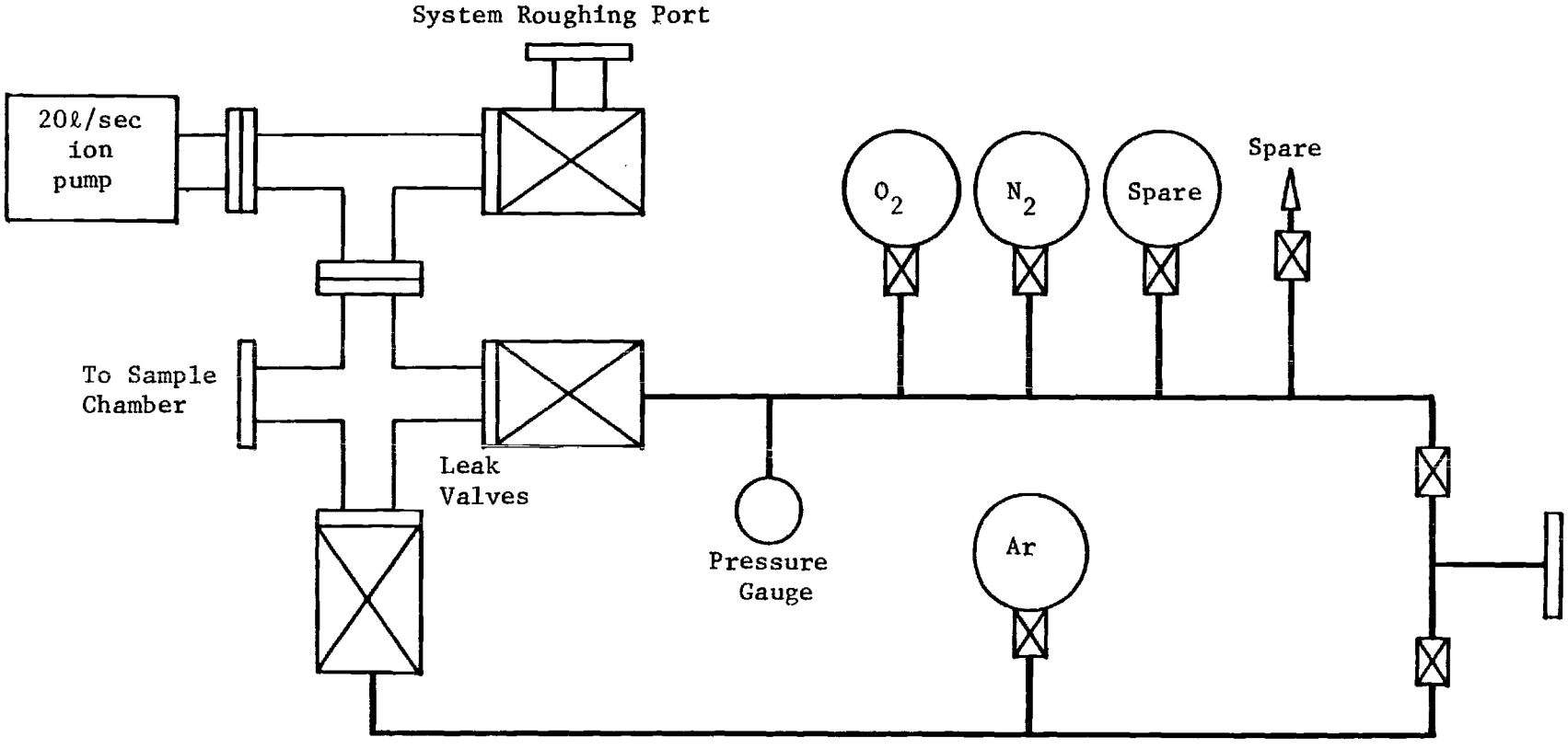

Figure 14. High Purity Gas Manifold

written in modular form allowing easy program modification. The system is task oriented, completely command initiated, and device interrupt driven. All idle time is used for the scope display. A flexible command decoder initiates all data collection and processing routines. If routines do not interfere with each other, more than one routine may be active at any time. A complete description of the software is presented in Appendix B.

The computer communicates with external devices through a positive logic TTL compatible input/output bus system. Each device controlled by the computer is connected in parallel on the "bus." Computer generated device selection codes are decoded by individual interface circuits that serve as a buffer between the computer and each piece of apparatus under control. Each interface is unique depending on the function and control requirements of each piece of apparatus. A block diagram showing the connections of the various pieces of apparatus to the computer is shown in Figure 15, and is described in detail in the following paragraphs. The computer is equipped with a standard teletypewriter for communication with the operator. Collected data may be printed or punched on paper tape using this device. Two additional output devices (a Tektronics 604 display scope and a Hewlett Packard 7004B point plotter) provide graphical display of data; both are driven by a single interface described in Appendix A.

The reflectometer and beam monitor detectors are both operated in the single photon counting mode. At low light levels, each detected photon produces an avalanche of electrons that appear at the output of the detector as a current pulse of 5-30 nsec. duration. For the

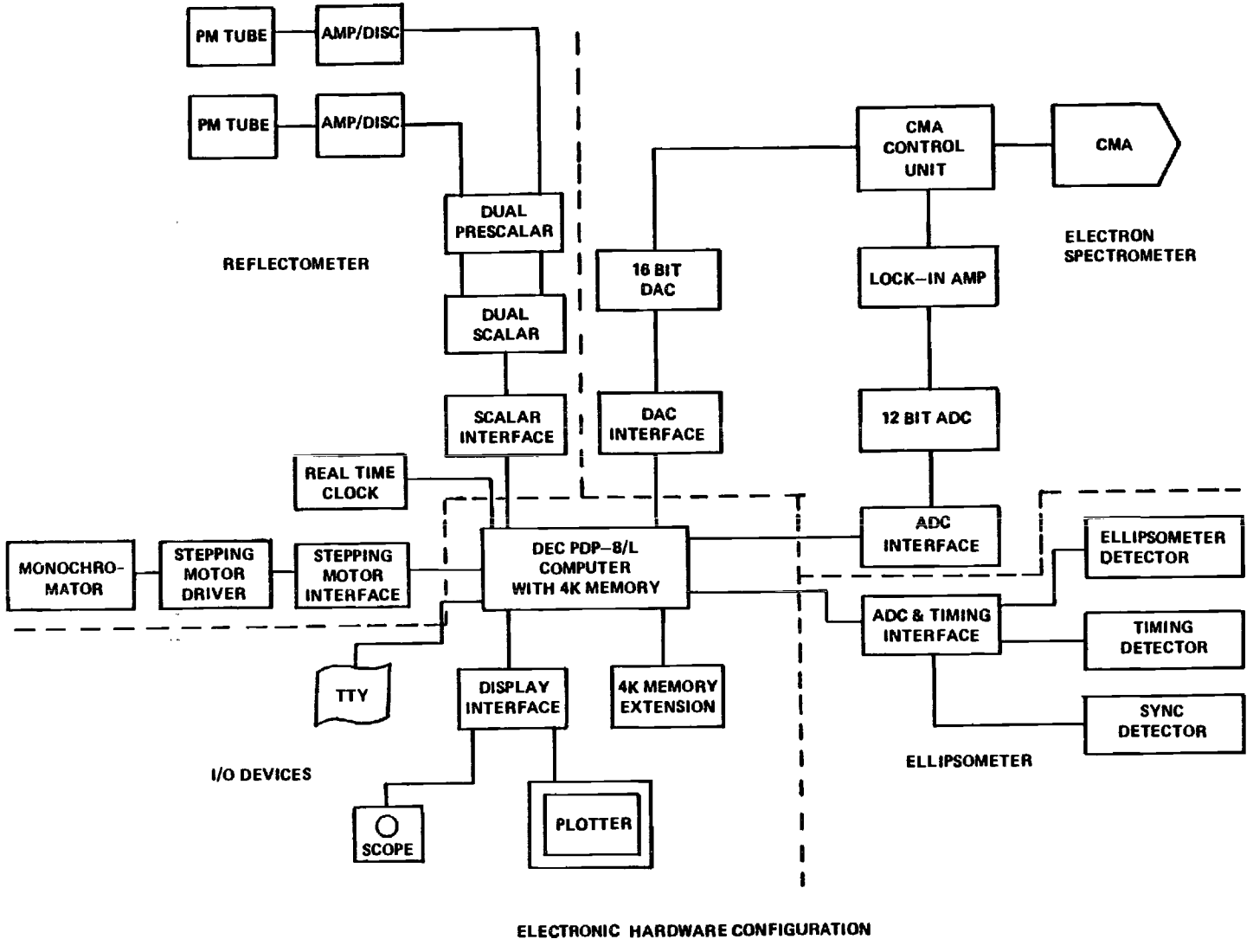

ELECTRONIC HARDWARE CONFIGURATION

Figure 15. Computer and Instrumentation Configuration

photomultiplier detectors, the outputs are fed directly to Ortec Model 9302 amplifier-discriminators. When using the channeltron detector, an Ortec Model 113 pre-amplifier modified by the addition of a high voltage coupling circuit was connected between the detector and amplifier-discriminator. The combination amplifier-discriminator allows detection of individual photons while discriminating against pulses of lower amplitude such as thermal electrons originating from the dynode surfaces and leakage currents occuring over insulating surfaces in the detector. However, thermal electrons originating at the photocathode are detected as photons. The pulse pair resolution of the 9302 is less than 10 nsec, allowing counting rates of up to 100 MHz. Nonlinearity in the counting rate of the system due to pulse overlap is given by [59]:

$$\text{Error} = \frac{R_1 - R_0}{R_1} = 1 - e^{-R_1 t_r} \qquad (3\text{-}1)$$

where

R_1 = actual count rate

R_0 = measured count rate

t_r = pulse resolution.

Limiting the overall count rate to 1 MHz keeps the nonlinearity to less than 1%. The output of each 9302, one for the reflectometer detector and one for the beam monitor, is connected to an Ortec Model 715 dual counter. The model 715 has two separate counting channels, each having preset maximum count that disables both counters when either counter reaches its maximum. Each counter has a resolution time of 100 nsec.

limiting the overall count rate of the system. An Ortec Model 9310 dual pre-scaler can be connected between the discriminator outputs and counter inputs providing an extra decade of counting. Although this first decade cannot be read, it restores the overall speed of the system to 1 MHz, and provides an increase by a factor of 10 in the number of photons counted. The actual value of the count in this first decade is insignificant, since the statistical uncertainty in photon counting follows the Poisson distribution and is $\sqrt{N}$ where N is the total count [59]. The Model 715 is designed to operate in an automatic data printing system and as such has control input and output signals plus a BCD data bus available. A computer interface designed to emulate the Ortec printing control allows reading of the counters by the computer. The interface is described in Appendix A.

The monochromator stepping motor is driven by a solid state stepping motor driver (Responsyn LD-8-5 and D-4-5) providing a sequential eight phase bidirectional output. The driver requires either a "forward" or a "reverse" pulse to move the stepping motor one step in the appropriate direction. The pulse is a negative-going TTL compatible pulse of at least one μsec duration. The directional pulses are provided by the computer through an interface described in Appendix A. The repetition rate for the pulses is set via a timer on the interface and is approximately 1000 pulses/sec providing a maximum rate of motion of 200Å/sec for the monochromator.

A third interface required for the reflectance measurements is a real time clock described fully in Appendix A. The AC line frequency is sampled such that it provides a "tick" to the computer 120 times per

second. Computer software then keeps track of the elapsed time during the photon counting period for thermal noise corrections to the total count as described below.

Prior to making a reflectance measurement, the thermal noise count rate for the detectors is measured with the light source off. The computer enables both counters and starts the real time clock; after one minute has elapsed, both counters are read and the resulting noise counts are stored in memory.

A typical measurement sequence would consist of the control program calculating a new position for the monochromator and executing the move; resetting and enabling the scalers; resetting and enabling the real time clock; finally entering the wait mode. When either of the scalers reach a preset maximum, both scalers are disabled, the clock is disabled and the scalers and clock are read. The time from the clock is multiplied by the previously measured noise count rate for each detector; and the resulting values are subtracted from the appropriate count. The ratio of the noise corrected values is then computed and stored for further processing.

A reflectance spectrum is measured by first moving the sample from the beam and rotating the reflectometer detector until it intercepts the beam. Using the appropriate "incident run" command, the response ratios of the two detectors for each data point are stored in one of four memory arrays. The sample is then aligned in the beam and the reflectometer detector rotated to intercept the reflected beam. The appropriate "reflectance run" command measures the combined sample reflectance and PM tube response ratio and then calculates the ratio of

value with the value stored during the incidence run, yielding for each data point the sample reflectance as given by the following relationship:

$$\text{Reflectance} = \left[\frac{B_R - T_R B_N}{A_R - T_R A_N}\right] \Big/ \left[\frac{B_I - T_I B_N}{A_I - T_I A_N}\right] \qquad (3\text{-}2)$$

where

A = count from scalar A

B = count from scalar B

T = time period count was accumulating

R = reflectance measurement

I = incident measurement

N = noise measurement

The CMA in the Auger spectrometer is controlled by a Physical Electronics Model 50-510 electronics system which provides for manual operation of the spectrometer. The integral electron gun is powered by a Physical Electronics Model 11-010 supply. A small 30 KHz a.c. signal is superimposed on the d.c. voltage applied to the CMA cylinders by the electronics system. The output of the CMA electron multiplier is then synchronously detected by a PAR HR8 lock-in amplifier, providing a direct measure of the differential of the electron distribution N(E) which inhances the relative amplitude of the Auger transitions by suppressing the slowly varying but large secondary electron background. Automated selection of the CMA passband energy is accomplished through a d.c. control voltage applied to the multiplex input of the 50-150. The control voltage is generated by a 16 bit digital-to-analog converter, yielding a

smallest step of less than 0.1 eV. Output of the lock-in amplifier is digitized by a 12 bit analog-to-digital converter. Both converters are controlled by the computer through interfaces described in Appendix A. Data may then be collected as the differential of the number of electrons versus energy.

The control program allows up to seven energy windows to be scanned. The width of each window is an input parameter, determining the resolution of the data, since each window has a fixed number (64) of data points. The system may also be used in a "windowless" mode producing a continuous spectrum of 512 data points. Scanning takes place at a constant rate of 1000 data points per second allowing 1 msec for recovery of the DAC and associated electronics. Windows are scanned sequentially; after scaning all windows, the process is repeated, continually averaging the current data with the previous data using the following relationship:

$$\bar{X}_i = \frac{(i-1)\bar{X}_{i-1} + X_i}{1}$$

where

X_i = i^{th} measurement

$\bar{X}_i$ = average value after i^{th} measurement

$\bar{X}_{i-1}$ = average value after $(i-1)^{th}$ measurement

An averaging period of 20 sweeps (approximately 10 seconds) produces data of good quality which is not significantly improved by further averaging.

Subsequent to data collection, peak-to-peak amplitude of the Auger

transitions within each window may be calculated on command. For any given transition, peak-to-peak height will be proportional to elemental concentration. When operating in depth profile mode, a complete data collection routine will occur followed by the calculation and printing of peak-to-peak heights for each window. The system then waits for a specified length of time and repeats the process. If the sample is being simultaneously sputtered at a constant rate, then the results are a printout of relative elemental concentration versus depth.

CHAPTER IV

EXPERIMENTAL PROCEDURE

During the course of this work, both optical and AES measurements were made on titanium during three different phases of the experiment. The first set of measurements were made on the sample immediately after initial preparation and insertion in the vacuum system, and are referred to as initial surface measurements. The second set of measurements occurred during and immediately after a surface cleaning procedure that removed surface contamination from the sample; the last measurement in this sequence is referred to as the clean surface measurement. The final sequence of measurements occurred first after repeated exposure to oxygen and then after oxygen ion bombardment; this set of data is called the oxidized surface measurements. The optical and AES measurement procedures were identical during all three phases and will only be described once.

The low energy measurements (2 eV - 11 eV) were made at Georgia Tech, while the high energy measurements (> 6 eV) were made at the UWSRC. A great effort was made to duplicate the experimental conditions and procedures for these measurements in order to facilitate correlation of the two sets of data. Deviations from identical procedure at the two sites will be noted in the discussion. Alignment of both the AES and optical spectrometer is discussed along with the operational procedure for each technique. Following the discussion of AES and optical

spectroscopy procedures, sample preparation, vacuum procedures; and sample cleaning and oxidation procedures are discussed.

Reflectance Measurements

Prior to the measurement of the sample reflectance, the optical path must be aligned, the monochromator calibrated, and the relative response of the reflectometer detector and beam monitor detector measured. Alignment of the optical path from the source to the monochromator is accomplished by adjusting the effective source position to maximize the first order intensity at the beam monitor. Using the UWSRC facilities, this consists of adjusting two grazing incidence mirrors located between the storage ring port and the monochromator. Using the tungsten source, the adjustment is made by sliding the lamp along slots in the mounting bracket until maximum intensity is achieved. Alignment of the system from the exit slit to the reflectometer detector is done first visually by adjusting the monochromator to the white point so that the beam is visible in a darkened environment, and then a final fine adjustment to maximize the detector response. First, the position of the aperture plate in the beam monitor is adjusted so that the aperture is in the center of the illuminated region. Next, the sample chamber position is adjusted by means of positioning bolts on the support stand until the light beam from the aperture passes horizontally through the chamber, falling on the sample at the same location as the AES electron beam. This adjustment is critical in order to insure that both measurements are being made on the same region of the sample. Fine alignment of the position may be made just prior to measurement. With the sample removed

from the beam, the reflectometer detector is rotated to intercept the beam. The height of the detector must be adjusted internally for it to completely intercept the beam. Final positioning is completed under vacuum conditions. Once the sample chamber is in proper position, only slight changes in the sample attitude and rotation of detector are necessary when realigning after changing the sample or sample position. This may be accomplished visually, followed by a final fine adjustment to maximize detector output.

Absolute wavelength calibration curves for the monochromators used in this work have been previously established [34,54]; however, the calibration for the GE monochromator was checked using a mercury lamp source and found to be accurate within ±3A. Relative calibration is accomplished by maximizing the monochromator output at the white point (zero angstroms) and entering this value along with the calculated number of steps per angstrom into the computer. The monochromator control software maintains an accurate record of the monochromator position.

The relative calibration of the two detectors is accomplished by lifting the sample clear of the light beam and rotating the reflectometer detector into the beam directly behind the sample position. The incident intensity is then measured as described in Chapter III using the same slit widths, filters, detector voltages, and photon energy ranges as used for the reflectance measurements. The measurements are divided into several segments that collectively span the 2 eV to 25 eV energy range. Segmented measurements are necessary so that filters, slit widths, detectors, and sources may be changed as needed. Table 4-1 shows the parameters for each segment including the photon energy range and

Table 4-1. Reflectance Parameters by Segment

Energy (lower)	Range (eV) (upper)	Step Size (eV)	No. of Steps	Slit Width	Filter	Source	Detector
2.0	3.0	0.02	51	250μ	Glass	Tung-Hal	Hamm.
2.9	6.0	0.05	63	250μ	Quartz	Hydrogen	Hamm.
5.0	7.2	0.05	45	250μ	Quartz	Hydrogen	Chan
7.0	10.5	0.05	71	250μ	LiF	Hydrogen	Chan
6.0	8.0	0.1	21	250μ	LiF	Storage Ring	Chan
7.7	11.0	0.1	34	75μ	LiF	Storage Ring	Chan
10.0	25.0	0.2	76	5μ	--	Storage Ring	Chan

energy step size. These values were established experimentally and minimize higher order interference while maintaining satisfactory photon count rates over the entire range. The overlap between segments is included to insure continuity of the data and provide a region to calculate scaling factors if there is a discontinuity in the data. The large overlapping regions between the UWSRC data and the Georgia Tech data allow better correlation of data taken at different times. The relative detector calibration curve is stored by segments in a computer memory array for recall when calculating reflectances as described in Chapter III. Typically, the upper count limits for the scalers are set at one million counts. With the count rate for both detectors set to an upper limit of 100 KHz, a typical data point will require from 15 to 20 seconds to accumulate. Operational voltages for the detectors are set at 1250 V for the beam monitor PM tube, 900 V for the Hammamatzu detector, and +3000 V on the channeltron anode with -300 V on the photocathode and the cone at ground potential. During measurements, internal light sources are turned off, windows are capped, and the gate valve to the pumps is partially closed to minimize stray ion noise at the detector. Under these conditions, detector noise rates range from less than one count per second in the channeltron to ~100 counts/sec in the beam monitor. The noise compensation procedure is described in Chapter III.

Reflectance measurements are made using the same parameters as those given above and in Table 4-1. The sample is first carefully aligned in the light beam; next the detector is rotated to the near normal incidence position, as close to the incoming light beam as possible without blocking a portion of it; and finally, the sample is rotated and

tilted to direct all of the reflected light onto the detector. At this point the reflectance is measured by first adjusting the parameters in Table 4-1 and then using the appropriate command to the computer which initiates the sequence of events described in Chapter III. The resulting noise corrected reflectance data may then be displayed on a scope, plotted, printed, or punched on paper tape for further analysis.

AES Measurements

AES data is collected prior to each reflectance measurement using a computer controlled synchronously averaged sweep from 0-600 eV. This range includes Auger transitions for titanium and all important contaminants. The data is averaged over 20 sweeps to reduce noise, which is especially a problem at the UWSRC. A complete measurement, which is stored in a 512 point array in the computer memory, requires approximately ten seconds. The data is collected in the normal differential mode to enhance the Auger data with respect to the slowly varying secondary electron background. Typical operating parameters for the Auger system are a primary electron beam energy of 3 KeV at 40 μA, 2 V p-p modulation at 30 KHz for the differential detection, 600 V potential on the CMA electron multiplier and 100 μV sensitivity with a one msec time constant for the lock-in amplifier. These parameters may be varied to enhance signal to noise ratios or reduce excessively strong responses.

The AES system is calibrated by pre-positioning the sample to give an accurate energy for the elastic back-scatter peak from the primary beam. A calibration routine for the computer then calibrates the computer derived sweep voltage to the electron energy as measured by the Auger control unit. The method uses a simple linear interpolation

that provides an energy accuracy of about 0.2% over the entire range.

If greater resolution of an Auger line is desired, a sweep over a limited energy range is possible. By reducing the modulation voltage, the resolution is enhanced to the point where it is limited by the CMA geometry. Noise is reduced until it is insignificant by increasing the number of sweeps averaged. Using this method, very good quality Auger data is collected for use in line shape analysis. A computer routine will numerically integrate the differential data to generate the N(E) distribution normally used for line shape analysis. Care must be taken that the lock-in amplifier is properly adjusted for zero response since a zero offset in the differential data will skew the result in the N(E) data. A proper zero is obtained if the electron beam is turned off and the lock-in zero control is adjusted to provide an unskewed N(E) response from the integration of the resulting background noise. High resolution data of several Auger transition were acquired during the course of this work.

Achievement of Ultra-High Vacuum

The routine production of an ultra-high vacuum environment is crucial to the controlled study of surfaces, especially highly reactive surfaces such as titanium. A commonly used unit of surface exposure is the Langmuir = 10^{-6} Torr-sec. For a material with a sticking coefficient approaching one, approximately a three Langmuir exposure is required to produce a monolayer of surface coverage [1]. That is, a monolayer will form in three seconds in a 10^{-6} Torr-vacuum. A set of reflectance measurements require approximately one hour to complete; therefore, the vacuum must be maintained at a pressure below $\sim 5 \times 10^{-10}$ Torr in order to

insure that less than one monolayer of contamination accumulates during the measurements.

Vacuum considerations of the materials in the sample chamber and a description of the vacuum system is presented in Chapter III. Extreme care must be exercised in the handling of all materials that are used inside the vacuum system to minimize contamination by low vapor pressure materials. All ceramic and metallic components are acid etched, cleaned in a trichloroethylene vapor degreaser, washed in distilled water, rinsed with acetone, and blown dry before being utilized in the vacuum system. When not under vacuum, the system is filled with dry nitrogen.

Starting from atmospheric pressure, approximately 90% of the air is removed by a carbon vane rotary pump. Roughing of the system is completed by two liquid nitrogen cooled sorption pumps operated in tandem which reduce the system pressure to $\sim 5 \times 10^{-4}$ Torr in fifteen minutes. At this point, the roughing valve is closed and the ion pumps are started; within two hours the pressure reaches 5×10^{-7} Torr. In order to significantly reduce the pressure below this level, the system is baked at ~250°C for 24 hours to outgas the walls and components inside the vacuum system. As previously discussed, this step is omitted when the reflectometer PM tube detector is installed, in this case the system is prebaked. During the bakeout period, all filaments within the system are turned on in order to outgas them; they then remain on after the bakeout has ended to insure that they do not reabsorb significant amounts of contaminants. It has been found that approximately 36 hours of filament degassing is required so that they do not contribute to the base pressure of the system. After completion of the bakeout and cooling

of the system, the base pressure is reduced to approximately 2×10^{-10} Torr. Ultimate vacuum is then achieved by cooling the cryogenic shroud with liquid nitrogen and sublimating titanium from the sublimation pump onto the shroud surface. Within an hour the pressure drops to $\sim 5 \times 10^{-11}$ Torr. At this pressure, 16 hours would be required to form one monolayer of surface contamination. Analysis of the residual gas showed that the major constituents were hydrogen (50%) and helium (~20%) with smaller amounts of oxygen, nitrogen, water, carbon monoxide, and argon (~5% each).

Sample Preparation

Samples 12.7 mm in diameter and 2 mm thick were cut from commercially prepared electron beam zone refined polycrystaline titanium rod having a nominal purity of 99.97%. Major impurities included oxygen (~150 ppm) and carbon (~50 ppm). A second set of samples was prepared from the same rod by machining them to 7.8 mm diameter with a 6.2 mm diameter groove cut 0.75 mm deep on one edge. The sample was then cut to a total thickness of 1.5 mm. These samples fit the mount in the Varian flip mechanism.

All of the samples were mechanically polished with an initial grit size of 15μ alumina and a final polish of .05 micron alumina. Mechanical polishing required approximately eight hours per sample. After the final polish, the samples were bright and specular, but exhibited a slight convex shape and other small variations in flatness.

It is generally believed that mechanical polishing destroys the crystal symmetry of the surface region [5]. In an effort to remove the

damaged region, several methods of chemical etching and electropolishing were tried, with limited success in all cases. Through trial and error, two methods were found to give the best results. One is an electropolishing technique of 65% methyl alcohol, 35% butanol, and 5% perchloric acid cooled with liquid nitrogen. Polishing currents of ~1/2 amp at ~45 volts produced a polishing effect. The polishing was very rapid and often was uneven over the surface of the sample. Pitting of the surface would occur if the sample was left in the bath longer than 5-10 seconds. The final result was a bright but uneven surface. A second method was a chemical polishing using a solution of 10% hydrofluoric acid, 60% hydrogen peroxide, 30% water. This etching solution also acted rapidly, leaving the sample hazy and diffuse in appearance if left in the bath longer than 15-20 seconds. Shorter periods left the sample bright and specular; however, the amount of the surface layer removed was not determined. This second method produced more reliable results and was used on most of the samples.

Thus, the procedure followed after the mechanical polishing was to place the sample in a trichloroethylene vapor degreaser for five minutes, wash in acetone, etch as described above, wash in distilled water, and blow dry with nitrogen. The sample was then immediately mounted and placed in the vacuum chamber, and the system pumped down as described in the preceding section. After attainment of vacuum, optical reflectance and AES measurements were made on the samples. The AES spectra showed strong carbon and oxygen lines, while the titanium line was distorted by the possible superposition of a nitrogen Auger line [60]. These spectra will subsequently be referred to as initial surface spectra.

Clean Surface Measurements

Heating and argon sputtering were used to remove contaminants from the titanium surface, with the heating also used to anneal the surface damage produced by the sputtering in the measurements made at Georgia Tech. Sputtering was accomplished by backfilling the system with argon to a pressure of 5×10^{-5} Torr, and bombarding the sample with ions from the Varian ion gun. The ion beam produces a faint blue glow near the surface of the sample that allowed alignment of the gun. The ion beam was defocused so that the entire surface was evenly covered. Using the quadrupole analyzer, it was found that the argon in the system became contaminated within a few minutes due to system outgassing unless the sublimation pump and cryoshroud were in operation. Using this pump and the small 20 ℓ/sec ion pump, while argon continuously leaks into the system through one of the leak valves, the argon would remain pure for several hours. The ion beam energy was set at 3 keV and the ion beam current density, which was difficult to measure due to the defocussed condition of the beam, was estimated at 10 $\mu A/cm^2$. Sputtering alone was unable to remove all of the carbon or oxygen, though AES showed less than one monolayer of oxygen or carbon present.

Using the AES in an automated mode, the peak to peak height of carbon, oxygen, sulfur, chlorine, and titanium Auger lines were monitored every five minutes. Using the sample heater in the mount and monitoring then sample temperature with a thermocouple, the sample was heated slowly. At 520°C the oxygen peak began to reduce, sulfur and chlorine, however, began to appear. At 560°C, the carbon peak began diminishing and at 600°C, the titanium peak began to change shape indicating the

disappearance of nitrogen. It is believed that the carbon, oxygen, and nitrogen diffuse into the bulk at this temperature while the sulfur and chlorine segregate on the surface from the bulk [61]. After ten hours of heating at 600°C, the carbon and oxygen were below the detectable limits of AES (about 1% atomic). A thirty second period of argon sputtering removed the chlorine and sulfur contaminants, leaving the sample clean to the limits of detection. The sample would remain clean for a period of more than one hour in $\sim 1 \times 10^{-10}$ Torr vacuum after which carbon and oxygen lines would begin to reappear. A short heating to 600°C for 30 minutes followed by a 30 second argon sputtering was sufficient to reclean the sample Optical reflectance measurements were made after the initial argon sputtering, after the final cleaning, and after approximately twenty-four hours of "soaking" in the vacuum. Measurements were made on samples that were both mechanically and chemically polished and just mechanically polished. For measurements made at UWSRC, the sample was not annealed following the argon sputtering. All of the results were very similar, with differences less than the calculated error. The best set of measurements are presented in the next chapter as the clean surface spectra.

Oxidized Surface Measurements

A series of optical and AES measurements were made on titanium after exposure to controlled amounts of oxygen. The oxygen was admitted to the sample chamber through a variable leak valve. During exposure, the gate valve between the ion pumps and sample chamber was closed, allowing rapid clearing of the oxygen from the system by opening the valve

since the volume of oxygen was minimized by restricting it to the sample chamber. The oxygen exposure varied from five Langmuir to 10,000 Langmuir, all at room temperature. The sample was initially cleaned as described in the preceding section, and the system base pressure was maintained at $\sim 10^{-10}$ Torr between exposures. Oxygen pressures varied from 5×10^{-7} Torr for the 5L exposure to 1×10^{-5} Torr for the 10,000 L exposure. Between the extreme exposures, four sets of measurements were made at other exposures. Pressure within the vacuum system was measured using a standard nude ionization gauge.

A second series of optical and AES measurements were made as the sample was subjected to oxygen ion bombardment. Again, the ion gun was defocused to cover the entire sample. Ion beam energies used were 1 KeV and 2 KeV while the beam current density was approximately 2 $\mu A/cm^2$. Oxygen pressure in the system was maintained at 1×10^{-5} torr. Bombardment times varied from 30 seconds to one hour with approximately ten complete sets of data taken at different intervals. All bombardments occurred at room temperature. After the final measurements on the oxidized sample, argon sputtering and heating was used to reclean the sample in order to verify the reproducibility of the data. Optical data taken at this point agreed very closely with the original clean surface spectra.

CHAPTER V

RESULTS AND ANALYSIS

The results of the measurements described in Chapter IV are presented in this chapter. The AES data is discussed in terms of the surface chemical environment and energy loss peaks are identified, while optical reflectance data for the initial surface, the clean surface, and several oxidized surfaces are presented. Optical constants are computed from selected reflectance data using a Kramers-Kronig analysis. The resulting optical constants are discussed in terms of the band structure of titanium and titanium oxide. The plasma frequency for both clean and oxidized titanium is determined. The optical constants resulting from our measurements are compared to other results in the literature.

Surface Composition From Auger Spectroscopy

Identification of Auger spectra was accomplished using The Handbook of Auger Electron Spectroscopy [62], which lists not only transition energies, but shows individual spectra for each element since relative peak intensity and line shape are also important in elemental identification. Approximate atomic concentrations in the surface region were calculated by dividing the peak-to-peak heights of the measured differential Auger spectra by the relative transition sensitivities as compiled in The Handbook of Auger Electron Spectroscopy, 2nd ed. [63]. In some cases, the shape of the AES spectra, by emperical comparison with known spectra, was used to determine the chemical bonding state of an

element. In Figure 16, representative AES spectra for the initial surface, clean surface, and oxidized surface of titanium are presented. Auger transitions from five elements are clearly recognized in the initial surface data: the LMM transitions of sulfur at 152 eV, and of chlorine at 181 eV; the KLL transitions of carbon at 272 eV and of oxygen at 503 eV; and the LMM doublet of titanium at 387 and 418 eV. The calculated relative concentrations of these elements are shown in Table 5-1. The broad, asymmetric shape of the carbon line indicates that it arises from elemental carbon rather than titanium carbide which produces a sharper triplet line [50]. A sixth element, nitrogen, is also tentatively indentified. Nitrogen produces a KLL transition at 379 eV which is obscured by the broader titanium transition at 387 eV. The only method of identifying nitrogen is through the change in shape of the titanium line at 387 eV. Shih, et al [60] have estimated the nitrogen concentration by noting that in clean titanium the positive excursion of the 387 eV titanium line is absent, but grew in height with exposure to nitrogen. A linear relationship was found between the nitrogen exposure and the ratio of the positive excursion of the 387 eV line to the 418 eV line of titanium. However, in this work, a positive excursion of the 387 eV peak was found on exposure of clean titanium to oxygen, indicating that this excursion may be due to the change in chemical environment of titanium rather than the superposition of the nitrogen line. This effect is discussed in more detail later in the chapter. The elemental concentrations calculated using relative Auger sensitivities have inherent errors due to dependence of peak to peak height on changes in peak shape caused by chemical effects, and on variations in escape depth and

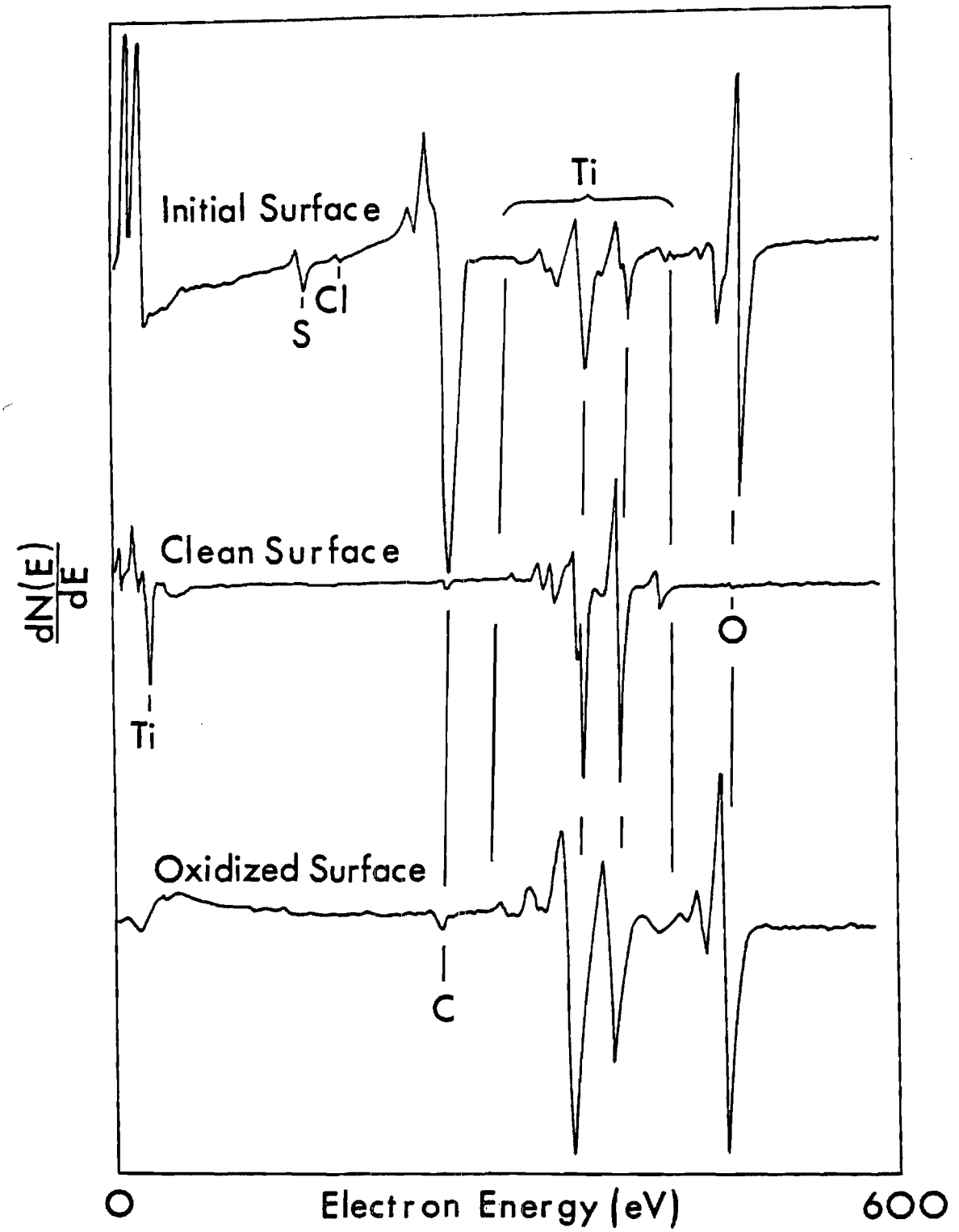

Figure 16. Auger Spectra for Initial, Clean, and Oxidized Titanium Surfaces

Table 5-1. Fractional Surface Composition Calculated From P-P Differential AES Data and Relative Auger Sensitivities.

Element	Initial Surface	Clean Surface	Oxidized Surface
Sulfur	.017	--	--
Chlorine	.001	--	--
Carbon	.675	.05	.09
Oxygen	.243	--	.56
Titanium	.062	.95	.34

backscattering factors in materials of different compositions. Errors of up to ±20% may be expected [63].

Sulfur and chlorine contamination on the surface originate in the bulk, although their concentration in the bulk is only five and ten parts per million, respectively [64]. However, at elevated temperatures, sulfur and chlorine segregate on the surface from the bulk [61], and, in fact, Auger measurements at 600°C indicated that they covered most of the surface. The sulfur and chlorine contamination appearing in the initial surface spectra most likely occurred during the system bakeout period. The principal contaminants, however, were carbon and oxygen. As previously stated, the carbon appeared to be unbounded, merely absorbed on the surface. Ellipsometric measurements by Smith [22] indicate that titanium handled under conditions similar to our sample had a TiO_2 surface layer of approximately 85Å thickness. However, our initial surface data indicate a titanium to oxygen ratio of approximately one to four. The discrepancy is apparently due to an excess of absorbed oxygen at the surface of the oxide layer, since the oxygen to titanium ratio dropped to approximately two to one shortly after beginning argon sputtering.

Only two elements, titanium and carbon, could be identified in the clean surface spectra. The carbon Auger line was very small, and the fractional composition was estimated at 5% or less. Nine different identifiable lines were found in the titanium Auger spectra. In addition to the large LMM doublet at 387 and 418 eV, smaller LMM lines at 330, 354, 364, 383, and 451 eV were observed. No positive excursion appeared on the 387 eV line. Two MNN lines at 28 and 46 eV were also observed; these lines were not clearly observed in the oxidized or initial

surface spectra, most probably due to chemical energy shifts [50].

The oxidized surface spectra of Figure 16 shows a strong oxygen KLL transition line in addition to the titanium lines and small carbon line. Table 5-1 indicates that the oxygen to titanium ratio is 1.7 to one, less than the required two to one ratio of titanium dioxide. The spectral shape of the oxidized surface in the region between the titanium 387 eV and 419 eV peaks is not the same as that of the clean surface; additionally, the positive excursion of the 387 eV peak is greater. Note also that the carbon contamination has increased to a fractional composition near 10%. Differential Auger spectra of the titanium LMM lines for oxygen exposures of zero, 5L, and 20 minutes of oxygen bombardment show an increasing positive excursion of the 387 eV line with oxygen exposure. The differential spectra for the clean surface and for these three exposure levels of the oxidized surface were numerically integrated to generate N(E) curves which are shown in Figure 17. An increase in the strength of the 387 eV peak along with the broadening of the 418 eV peak are seen to occur with oxygen exposure. Since our differential spectra on exposure to oxygen is similar to the behavior on exposure to nitrogen as reported by Shih, et al [60], we believe this effect to be due to chemical processes rather than the simple superposition of a nitrogen line. This view is supported by two recent studies: one by Solomon and Baun [65] on the Auger lineshapes of Ti, TiO, and TiO_2; and the other by Shih and Jona [66] on the oxidation of Ti. Shih and Jona further conclude that a TiO rather than TiO_2 structure forms on the surface with low values of oxygen exposure. Our work supports this view; calculations using relative Auger sensitivities indicates less than two to one oxygen

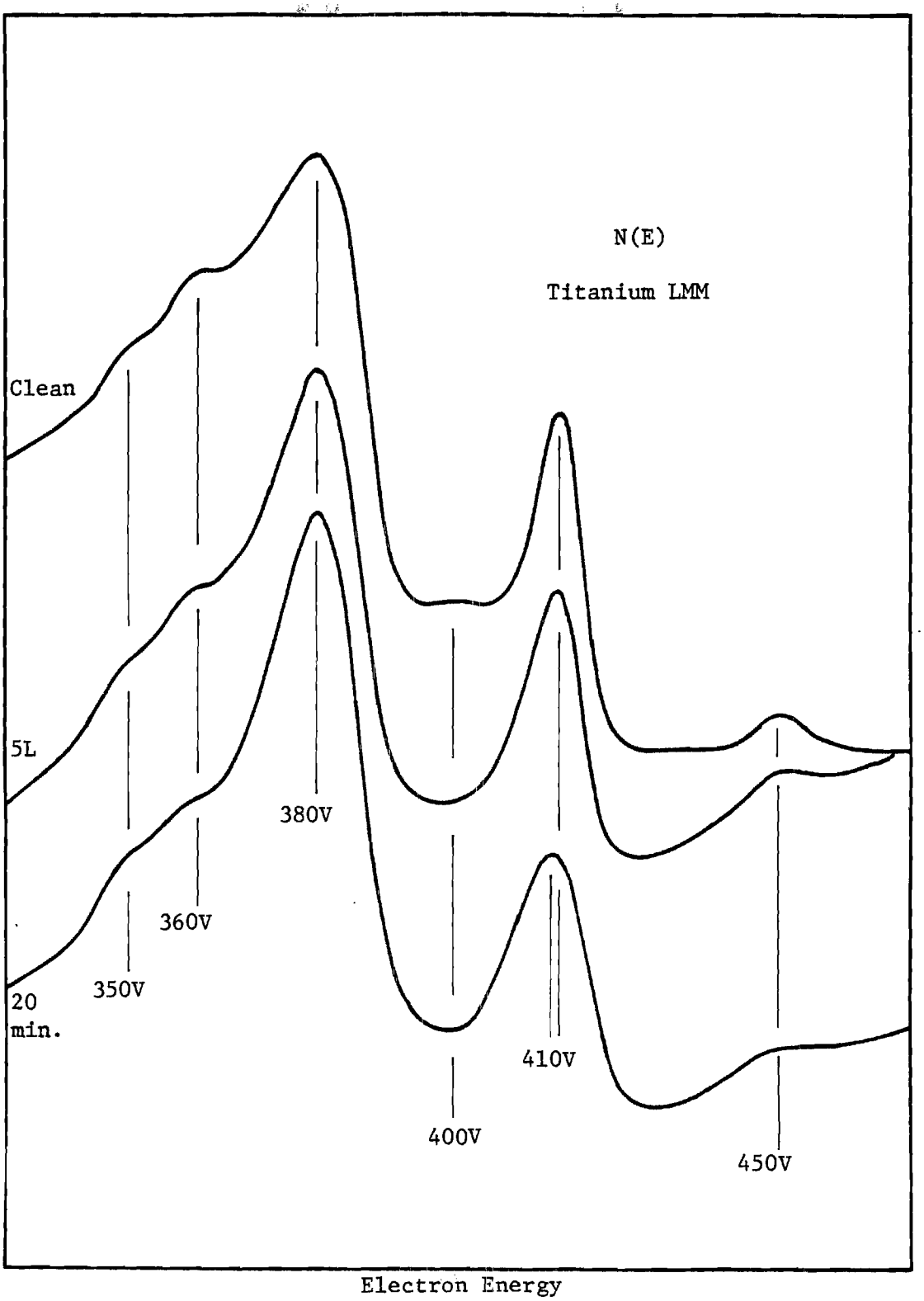

Figure 17. N(E) Spectra for the Titanium LMM Transitions With Oxygen Exposures of Zero, 5L, and 20 min. Oxygen Ion Bombardment

to titanium ratios. Additionally, the titanium Auger line shapes for our oxidized samples compare most closely to Sólomon and Baun's line-shape for TiO, while our initial surface data compares closely to their data for TiO_2. Under oxygen bombardment no change is seen in the relative peak height ratios. We therefore conclude that the oxide layer formed under low oxygen exposure and oxygen ion bombardment is predominantly TiO rather than TiO_2.

One additional measurement using the AES apparatus was made on both the clean and oxidized surfaces: the energy loss spectra from the elastic backscatter peak. Discrete energy losses suffered by the primary electrons result in smaller peaks in the N(E) spectra at these discrete energies below the elastic peak. In addition to losses due to interband transitions, losses due to plasmon excitations should also be visible. In the clean surface spectra, losses were observed at 10.3, 15.5, 50.0, and 63.2 eV; while in the oxidized surface spectra we observed losses of 12.5, 25.0, and 46.9 eV. The loss peak in the oxidized surface at 12.5 eV was identified as the volume plasmon with the 25 eV peak as a double plasmon loss. In the clean surface spectra, the 15.5 eV peak was identified as the volume plasmon while the 10.3 eV peak is identified as a surface plasmon, occuring near the predicted 10.9 eV value. The 10.3 eV peak was extremely sensitive to surface contamination, disappearing within several minutes of sputter cleaning the surface. The peak seen in both spectra at 47-50 eV is attributed to interband absorption between the titanium 3p band, for which the free atom value is approximately 45 eV below the Fermi level, and the conduction band. This result is in disagreement with the X-ray photoemission data of Shirley, et al. [67]

which measured the 3p level to be 37 eV below the vacuum level. The 63.2 eV peak, which was much weaker than the others is attributed to a double absorption: the 50 eV absorption plus a plasmon. The measured values for the surface and volume plasmons disagree with previously reported values, which are listed in Table 5-2. We note that our measurements are the first reported on bulk titanium under closely monitored surface conditions.

Reflectance Results

Reflectance data taken immediately after the Auger data of Figure 16 is shown in Figure 18. The measurements were made in seven segments as shown in Table 4-1, and consequently small discontinuities appeared at the junctions between the segments due to nonlinearities in the reflectometer response and slight errors in positioning of the sample or detector. These discontinuities were removed by scaling each segment such that a smooth curve resulted. No other data manipulation was used. From the magnitude of the discontinuities, we estimate the error in the absolute magnitude of the reflectance to be less than 10%, with the majority of the error originating from scattered light at the sample surface. The relative error in the shape of the curve should be much less, originating mainly from the statistical variation in photon counting and second order contributions to the measurements. The statistical error is calculated at less than 0.5% while the second order contributions are negligible due to the use of filters except in the region above 10 eV where a suitable second order filter did not exist. The blaze of the monochromator minimized the problem and the error was estimated at less

Table 5-2. Reported Plasmon Energies of Titanium (electron volts)

	Bulk	Bulk/$\sqrt{2}$	Surface
Free electron model	17.6	12.4	12.4
This work (optical)	15.3	10.8	--
This work (elec. loss)	15.5	10.9	10.3
Lynch et al. (optical)	13.7	9.7	10.7
	4.3	3.3	4.2
Simmons and Scheibner (elec. loss)	11.5	8.1	5.0
Robins and Swan (elec. loss)	17.6	12.4	--
Best (elec. loss)	25.1	17.7	--

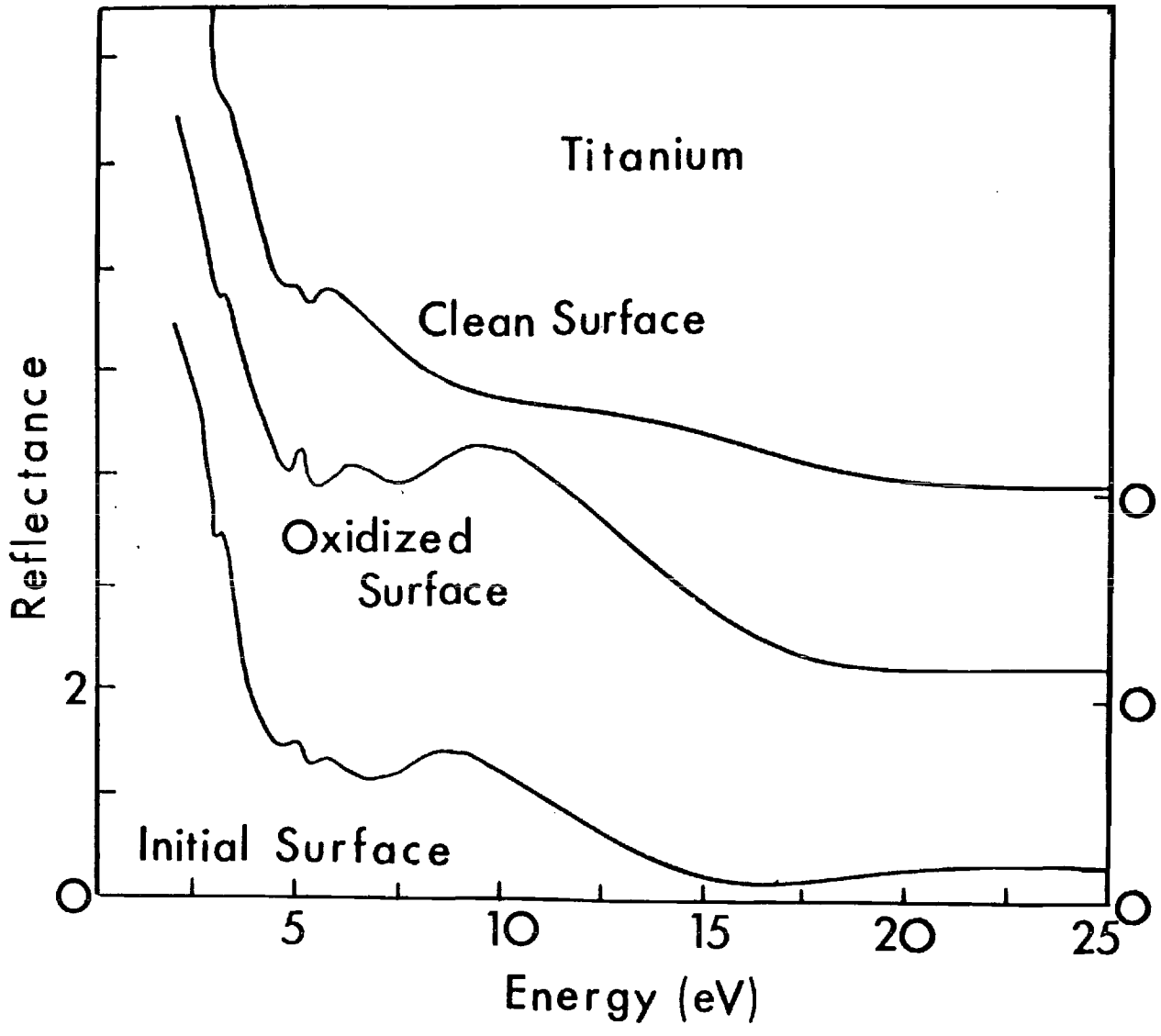

Figure 18. Reflectance of Initial, Clean, and Oxidized Titanium Surfaces

than 3% at 11 eV where the LiF filter was inserted.

The reflectance spectra of the initial surface and oxidized surface appear quite similar, while the clean surface spectra exhibits marked differences from the other two. The reflectance below 5 eV is similar in all three spectra. The most apparent differences are a large peak near 10 eV and a broad peak above 20 eV in the reflectance of the initial and oxidized surface spectra that is completely absent in the clean surface spectra. A closer examination reveals that the 10 eV and >20 eV peaks occur at slightly lower energies in the initial surface spectra than in the oxidized surface spectra.

A more detailed study of the transition from clean surface to oxidized surface was made. Beginning with a clean surface, the reflectance between 5 eV and 25 eV was measured after successive oxygen ion bombardments. The results are shown in Figure 19. The uppermost curve is that of the clean surface; each subsequently lower curve is after a longer oxygen bombardment period. We see from this figure the growth of the peak at 10 eV and a significant reduction in the reflectance at lower energies. The broad structure above 20 eV is seen to shift to lower energies with increasing bombardment time. Note that the peaks at 6 eV and 10 eV do not shift in energy. The oxidized surface spectra from Figure 18 represents an intermediate stage of oxidation, falling somewhere between the second and third curves of Figure 19.

Kramers-Kronig Analysis

As discussed in Chapter II, the complex refractive index and the complex dielectric constant may be calculated from the complex

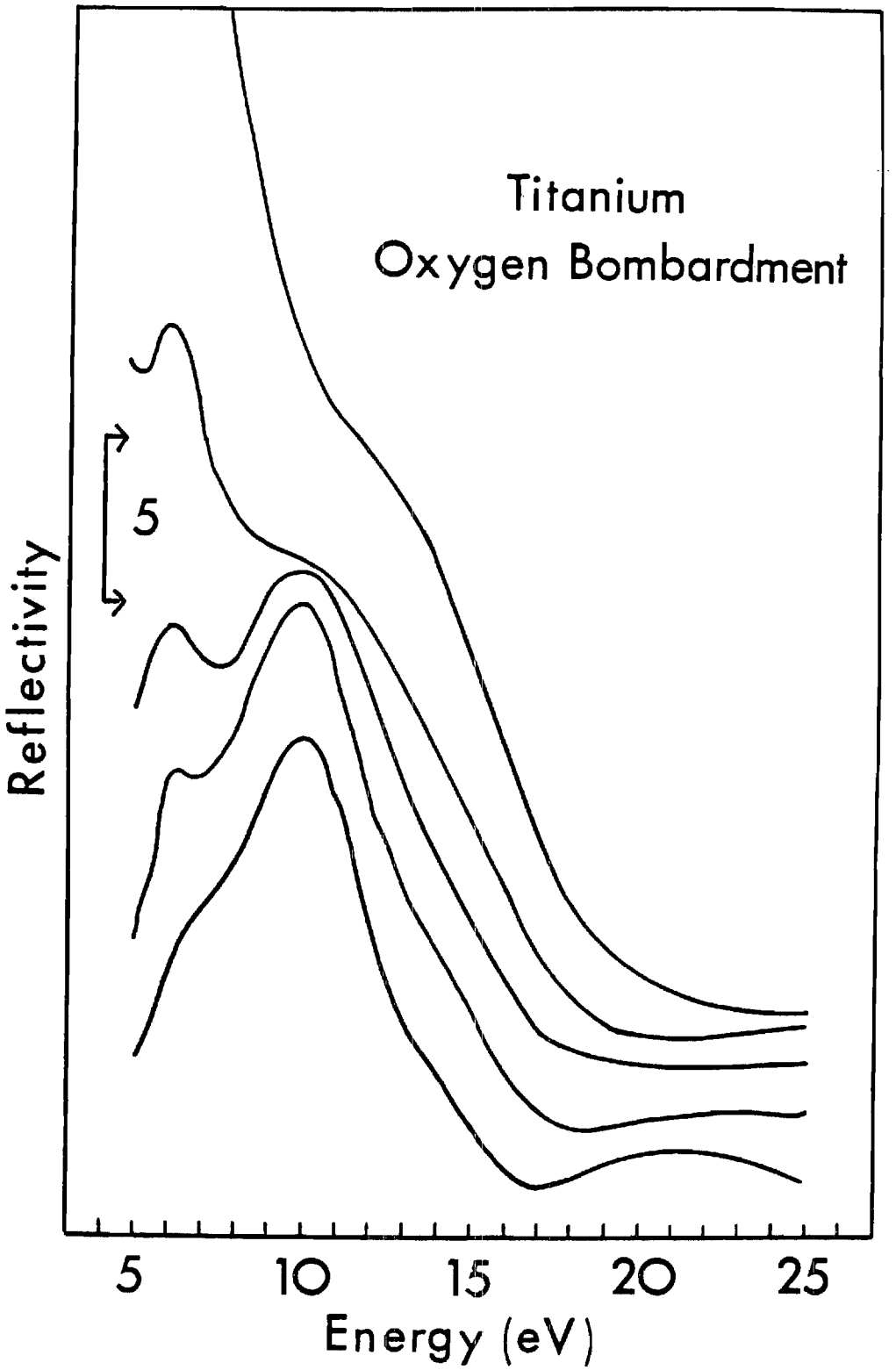

Figure 19. Reflectance of Titanium Under Oxygen Bombardment

reflection coefficient, $r = re^{i\theta}$. The reflection coefficient in turn may be calculated from the reflectance R if the phase factor θ is known. A Kramers-Kronig analysis of R, using Equation (2-24) which we repeat here for convenience, yields the phase factor

$$\theta(\omega) = -\frac{1}{2\pi}\int_0^\infty \frac{d\ \ell n[R(\omega')]}{d\omega'}\ \ell n\ \left|\frac{\omega'+\omega}{\omega'-\omega}\right| d\omega' \quad . \tag{5-1}$$

Numerical integration of this equation for all values of ω in the energy range investigated allows the optical constants to be computed in this range.

Since the integral extends from zero to infinity and our data is over a finite range, suitable extrapolations of the data must be made to calculate the integral. In the region below 2 eV, the measurements of Lynch, et al. [7] provide data to 0.15 eV and a Drude theory extrapolation was used below there. This data was used for all of the analyses made since oxide layers should be relatively transparent in this region, also any low energy approximation will affect mainly the amplitude and not the shape of the high energy results, and finally it was the only data available. The high energy extrapolation presents greater problems since, as our data has shown, oxide layers may have a significant effect on the reflectance in this region. Using the Drude-Zener theory of metals, a simple extrapolation for R may be calculated. At frequencies far above the plasma frequency ω_p, we may set the extinction coefficient $k = 0$; thus Equation (3-11) becomes $\varepsilon_1 \approx n^2$. From Equation (2-40), we have

$$\varepsilon_1 = 1 - \frac{\omega_p^2}{\omega^2} \tag{5-2}$$

or by binomial expansion

$$n = \varepsilon_1^{1/2} \approx 1 - \frac{1}{2}\frac{\omega_p^2}{\omega^2} \quad . \tag{5-3}$$

Substituting into Equation (2-42) yields

$$R = \frac{(-\frac{1}{2}\frac{\omega_p^2}{\omega^2})^2}{(2 - \frac{1}{2}\frac{\omega_p^2}{\omega^2})^2} \approx \frac{1}{16}\frac{\omega_p^4}{\omega^4} \tag{5-4}$$

or, if we normalize the result to the highest measured reflectance R_0 at energy E_0, we have

$$R = R_0(\frac{E_0}{E})^4 \quad . \tag{5-5}$$

This extrapolation, however, does not take into account the possibility of higher energy transitions in the extrapolation region. One method of compensation for these transitions is to make the exponent in Equation (5-5) adjustable and fitting it to obtain results consistant with an independently measured optical constant at a given frequency. If independently measured results are not available, then another method is to fit the exponent such that the sum rules for the optical constants are satisfied. Altarelli, et al. have derived a set of "sum rules" which follow from the dispersion relations and the physical requirement that the

medium must be free-electron-like in the high frequency limit [68]. The two sum rules of interest are

$$\int_0^\infty (n-1)\,d\omega = 0 \tag{5-6}$$

and

$$\int_0^\infty (n-1)\,k\omega\,d\omega = 0 \quad . \tag{5-7}$$

Ellis [52] has found Equation (5-7) converges quicker than Equation (5-6), thus we use this second sum rule to fit the exponent α in the following extrapolation.

$$R(E) = R_0 \left(\frac{E_0}{E}\right)^{\alpha} \quad . \tag{5-8}$$

If all interband terms are at energies below E_0 than we expect $\alpha = 4$ as calculated previously; but if interband terms occur above E_0, then the reflectance must fall off more slowly and $\alpha < 4$. The integral for θ does not converge for $\alpha < 2$ so $2 < \alpha < 4$. In all of our data we have found convergence of the second sum rule for values of α between 3.5 and 3.8. In all cases in which this method was tried, Equation (5-6) also yielded reasonably small values. A highly efficient computer program for solving Equation (5-1) was developed by Gatland [69] and is presented in Appendix C. Once the phase θ is computed, the calculation of the optical constants is straightforward from Equations (2-25), (2-26), and (2-11). The calculated values of the complex dielectric constant, ε_1 and ε_2, for the

three sets of reflectance data of Figure 18 are shown in Figures 20 and 21.

Analysis of the Clean Surface Data

Previously reported values for the optical constants of titanium have, as mentioned previously, varied widely. The most comprehensive optical study of titanium has been that of Lynch, et al. A comparison of their reflectance data for titanium and our clean surface data is shown in Figure 22. The Lynch, et al., data agrees quite closely with our data at energies below 7 eV, though our data has a higher absolute magnitude. Above 7 eV the Lynch et al. data exhibits peaks at 10 eV and 25 eV, which are absent in our clean surface data but are present in our oxidized surface data. From these results we conclude that the Lynch, et al. data represents an oxidized titanium surface. Of the several other optical studies of titanium, only the work of Smith [22] was performed at UHV with attention to surface contamination. However, his ellipsometric measurements were only at two wavelengths in the visible. His values of n and k yield values of ε_1 that are positive while our values for ε_1 are negative in that region; however, the two values of ε_2 were computed to be within 20% of our values. In an attempt to fit our data to his optical constants, we were unable to find a value of the extrapolation coefficient α which would yield a dielectric constant equal to his. The free electron model predicts ε_1 to be very negative in the visible; however, the presence of absorption throughout the region will modify this result. However, it would require a very sharp absorption band at slightly higher energy to produce the value of $\varepsilon_1 \approx 8$

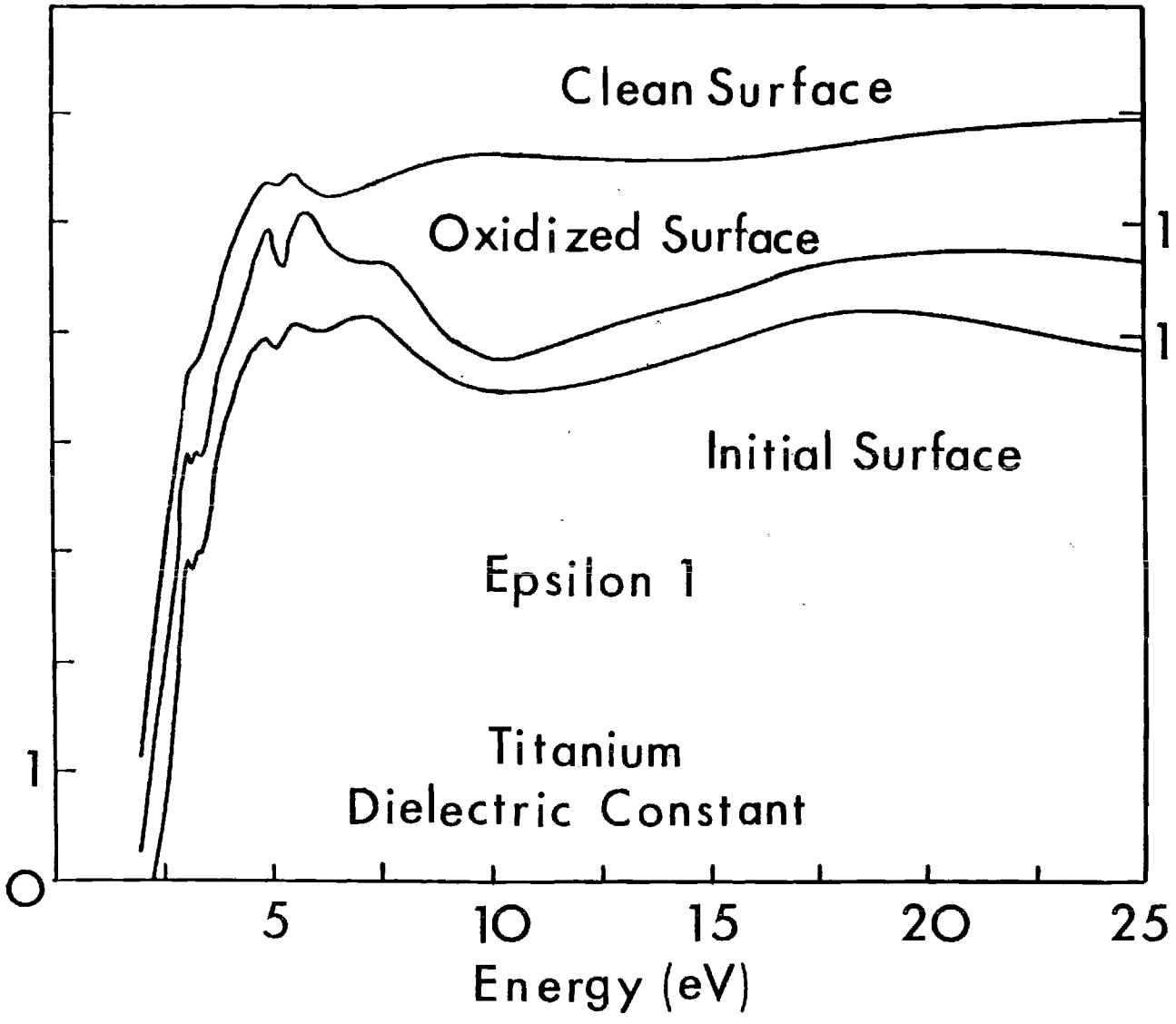

Figure 20. The Real Dielectric Constants for the Initial, Clean, and Oxidized Surfaces of Titanium

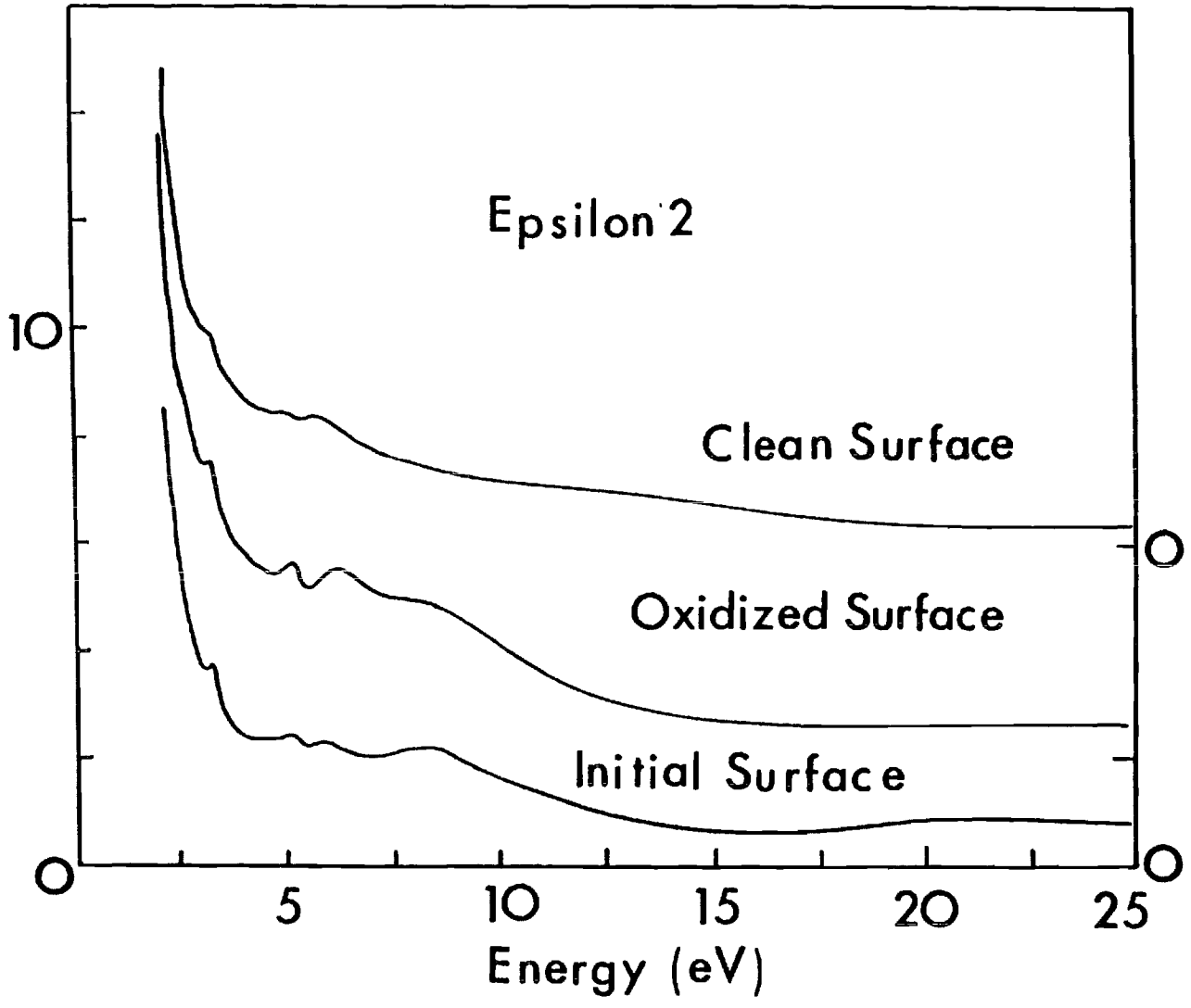

Figure 21. The Imaginary Dielectric Constant for the Initial, Clean, and Oxidized Surfaces of Titanium

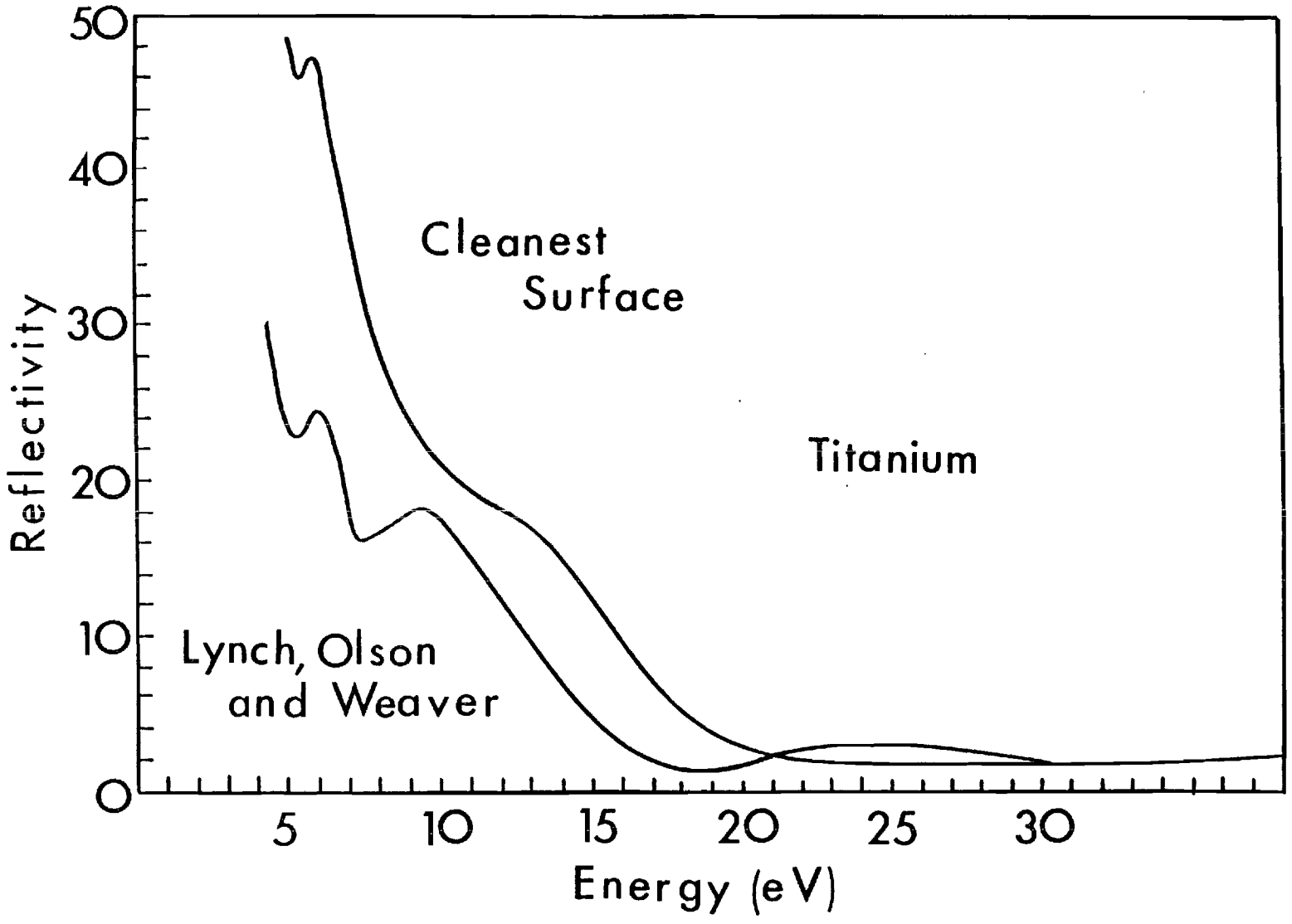

Figure 22. Comparison of Clean Titanium Reflectance With Reflectance of Lynch et al.

measured by Smith. In contrast, the values of Kurcirek [24] for a clean surface agreed to within 10% of ours for ε_1 and 50% for ε_2.

Theoretical studies of titanium are limited, however, recent self consistent band structure calculations have been made by Hygh and Welch [12-14] but have not been fit to any experimental data. From Equations (2-63) and (2-64), we see that for the case of direct transitions, ε_2 is proportional to the joint density of states; or for the case of indirect transitions, proportional to the convolution of the occupied and unoccupied density of states. Joint density of states data was not available from the band structure calculations of Hygh and Welch, but density of states data for calculations using two different exchange parameters were presented. The results of the convolutions of these two sets of data are shown in Figure 23. While the peak structure of the convolved density of states may be very different from the structure of the joint density of states, it does represent an upper limit in both the energy range and number of possible transitions. Therefore, the convolved density of states can, in the case of indirect transitions, directly reflect structure in ε_2; or, in the case of direct transitions simply serve as an upper bound for the absorption structure in ε_2. The band structure calculation show that the relatively flat d bands lie in the same energy range as the s bands, and in fact, the fermi energy falls near the middle of the d bands. Interband absorption thus begins near zero energy and persists very strongly throughout the infrared and visible portions of the spectrum, and as seen in Figure 23 extends more weakly into the ultraviolet due to transitions from lower lying s bands into unoccupied d bands. Comparing our calculated ε_2 with the convolved density of

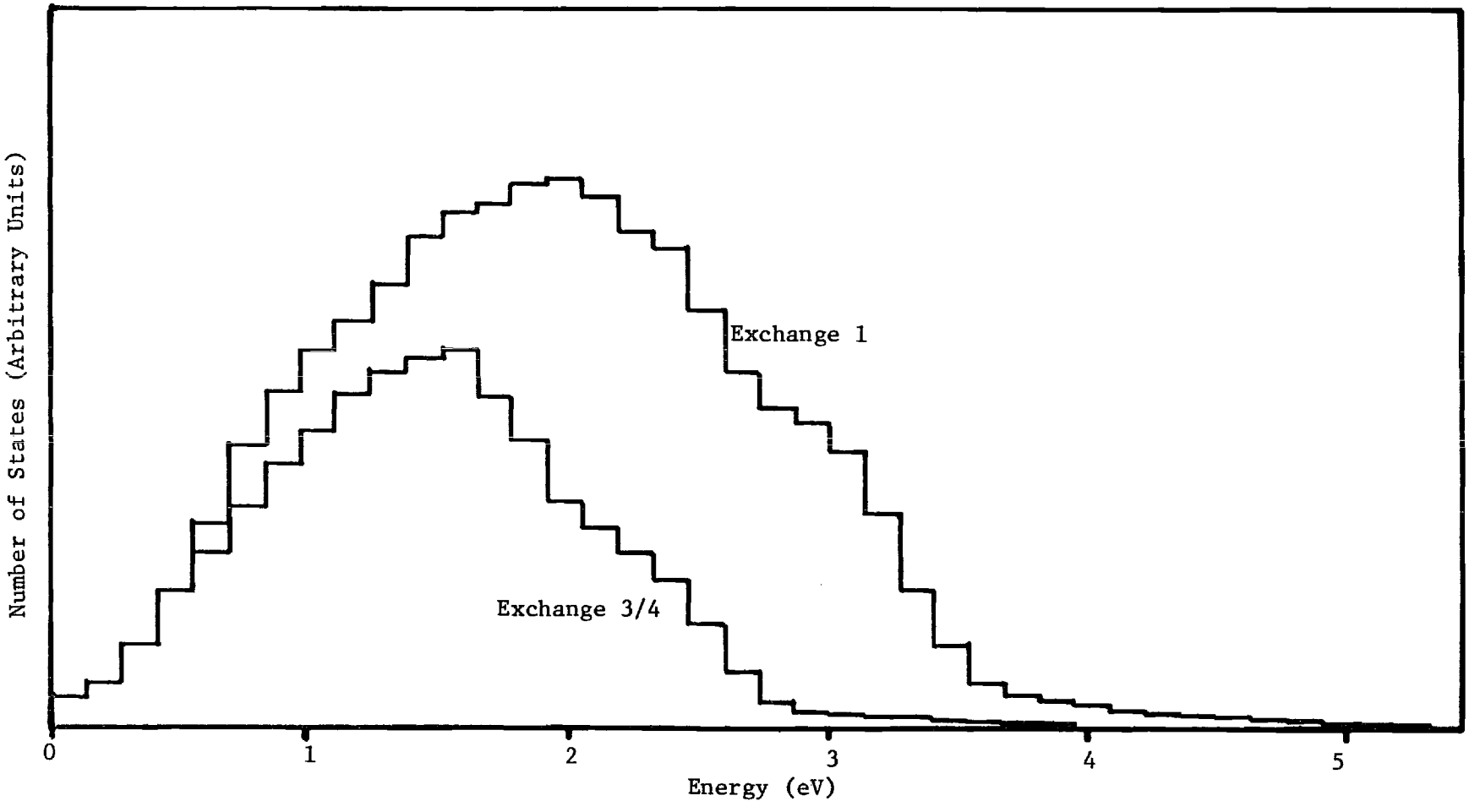

Figure 23. Convolution of the Density of States of Titanium From the Calculations of Hygh and Welch

states, we see general agreement; strong interband absorption at lower energies persisting in a tail extending well into the ultraviolet. However, the structure in the convolved density of states for either exchange coupling is not as wide as the observed structure in ε_2. The band widths and hence the width of the interband absorption region is a relatively sensitive parameter in band structure calculations [15]. Photoemission data of Eastman [16] has measured the d band widths of titanium at nearly twice that predicted in the calculation. Correction of the band calculation to show agreement in the d band widths would do much to improve agreement with our measurements. Finally we note that there are no transitions predicted from the band structure calculations of titanium to explain the large peaks at 10 eV and >20 eV observed in our oxidized surface data and the data of Lynch, et al.

If we assume that the $3d^2 4s^2$ conduction electrons of titanium are free, then the calculated plasma energy $\hbar\omega_p$ for titanium is 17.6 eV. From our calculated values of ε_1 and ε_2, the energy loss function (Equation 2-45) has been calculated. Peaks in this function may be related to both interband losses and plasmon losses, therefore, the plasmon energy may be identified by a peak that cannot be related to structure in ε_2. The calculated loss functions showed broad structure and the calculations for both the clean and oxidized surfaces exhibited only one peak, at 15.3 eV, that could not be related to structure in ε_2. Since this peak was present in both the clean surface and oxidized surface calculations, we identify it as a bulk plasmon loss. This value of $\hbar\omega_p$ is in disagreement with the free electron value but agrees well with the value of approximately 15.5 eV measured by electron backscattering. Other values

of ω_p have been reported in the literature [7,70-72] and are summarized in Table 5-2. As discussed in Chapter II, interband transitions below the plasma frequency such as are present in titanium should tend to raise the plasma frequency above the free electron value, however, most of the reported results and our results are lower in energy. Nozieres and Pines [39] also predict for titanium that ω_p should be greater than the free electron value. A possible explanation for the observed result is to note that the free electron approximation is not valid for titanium since the d bands are quite flat and do not resemble a parabolic free electron band. For a flat band the quantity $\nabla_k^2 H$, where H is the electron energy, will be small and, from Equation (2-46) increase the effective electron mass, thereby lowering the plasma frequency. An alternative explanation is to consider the d bands do not have enough mobility to contribute to the plasmon; with only s electrons contributing, the free electron plasma energy falls to 8.8 eV. The majority of the d interband transitions still fall below this energy and thus tend to raise the plasma frequency to the observed values. The question of which view is correct must be considered in the light of the fact that both approaches acknowledge the lack of freedom of the d electrons and qualitatively produce the same result.

In an attempt to optically verify the interband transition between the 3p band and the conduction band seen in the energy loss spectra, a reflectance spectra was measured to 50 eV. Light intensity was extremely low and resolution poor, but a small peak about 4 eV wide centered at 47 eV was observed. This value is 3 eV lower than that observed in the energy loss spectra of the clean surface, but near the free atom value of 45 eV.

We believe then that a qualitative understanding of the optical properties of titanium has been achieved, and that our measurements can aid in the refinement of band structure calculations leading to quantitative understanding.

Analysis of the Oxidized Surface

Reflectance spectra of the initial surface and oxidized data both seen in Figure 5-3 show considerable structure absent in the clean surface data. The large peak near 10 eV and the broad peak above 20 eV are the two major differences, though an overall reduction in the reflectance below 7 eV is also observed. These effects may be qualitatively understood in terms of Equation (2-72) and the subsequent discussion if we assume that the oxide phases of titanium in the surface layer have strong interband absorption lines at slightly lower energies than the observed reflectance structure at 10 eV and >20 eV. If interband absorption is absent or small at lower energies, then, as discussed in Chapter II, the effect of the oxide layer would be to reduce the reflectance of the metal substrate while generally preserving its shape, as is observed. Furthermore, absorption bands at a certain frequency should produce increases in the reflectance at slightly higher energies as would be expected in the reflectance spectra of the oxides alone.

Optical measurements above the visible range for the oxides of titanium have not been reported, so a direct comparison of the data or a quantitative modeling of the reflectance using Equation (2-72) cannot be made. Instead, we have used a Kramers-Kronig analysis of the reflectance data to generate a set of effective optical constants for the composite layer-substrate system. A simplistic argument could be made

that since absorption is proportional to ε_2, structure present in ε_2 of the clean surface data must be due to absorption in the oxide layer. McIntyre [48], however, has shown that the effect of the surface layer can be to increase the absorbance of the substrate and from Equation (2-72) we see that the relative contributions of the various optical constants are not easily separated. Ribarsky [73] has performed a test calculation using the thin film equations and has shown that peaks in ε_2 of the film are directly reflected in peaks in ε_2 of the composite system. From this background we can attribute the structures in ε_2 of the oxidized and initial surface data at ~9 eV and >20 eV as being associated with the titanium oxide layer rather than the titanium substrate.

Wall, et al. [74] have attributed these peaks to transitions from the oxygen 2p and 2s bands, respectively. Joint density of states calculations based on the band structure calculations for TiO by Jennison and Kunz [31] shown in Figure 24 have been compared with an experimental joint density of states based on our values for ε_2 of the oxidized surface using Equation (2-62) and assuming a constant oscillator strength. Table 5-3 shows a comparison of peak maxima for the calculated and experimentally derived joint density of states as well as ε_2 data of Lynch, et al. The values are in generally good agreement. Examining the contributions to the 9 eV peak in the calculated joint density of states shows that they arise from states of p-like symmetry while the peak around 30 eV arises mostly from oxygen 2s. This discrepancy between the theoretical value for the 2s band and the observed peak may be partly due to final state relaxation; however, the width of the observed peak

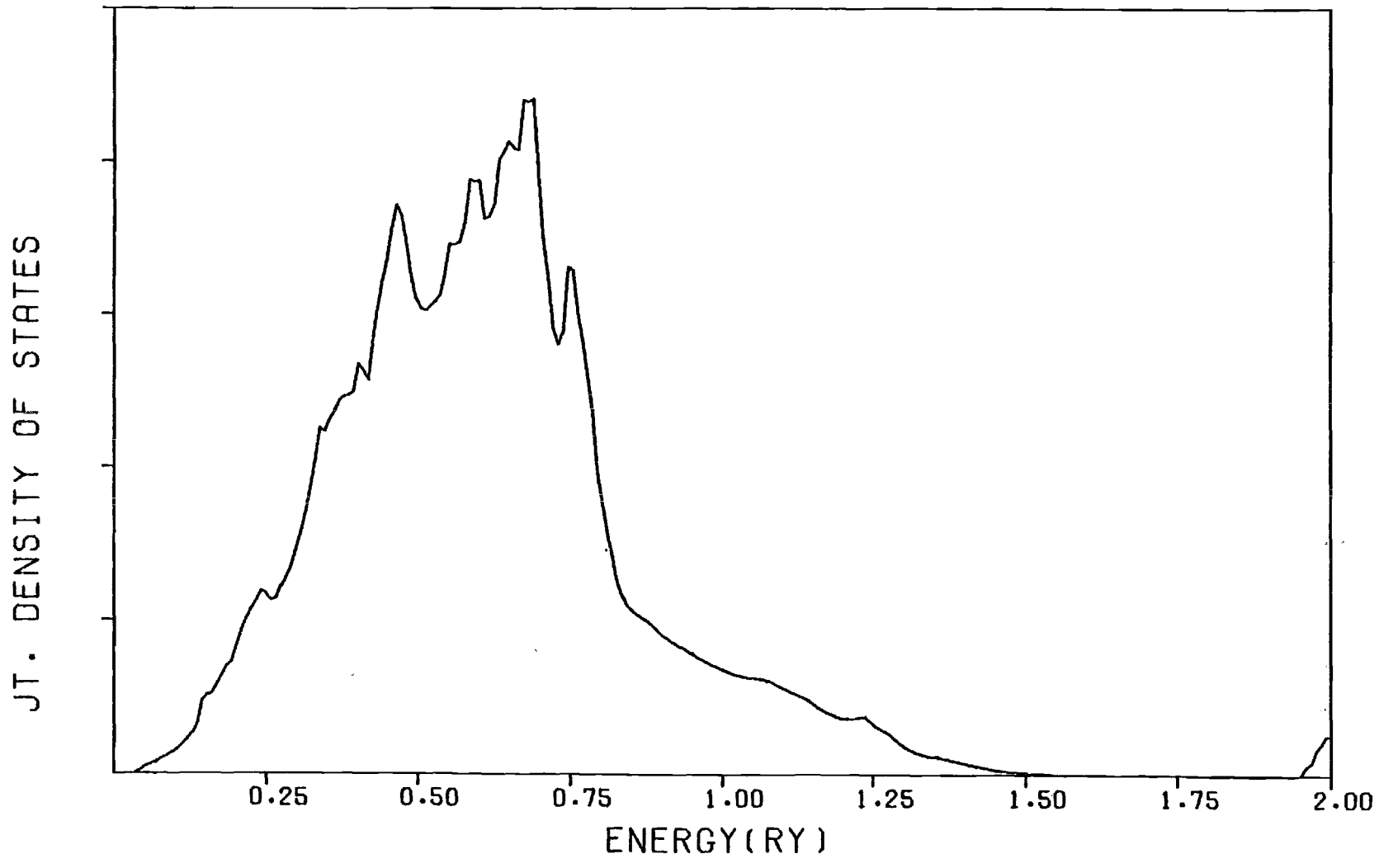

Figure 24. Joint Density of States for TiO Based on the Calculations of Jennison and Kunz

Table 5-3. Comparison of Peak Maxima From the Calculated and Experimental Joint Densities of States, and Lynch's ε_2 Data. All Energies are in eV.

Calculated	Experimental	Lynch et al.
3.28	3.32	3.2
5.44	5.20	5.6
6.34	6.45 (shoulder)	5.6
9.40 (central maximum)	8.78	8.2
31.6	24.5	23.8

is not explained.

Returning to the reflectance spectra of Figure 19, we note successively lower energy of the >20 eV peak with increasing oxygen bombardment while the 10 eV peak remains constant in energy. Remembering that the 10 eV reflectance peak corresponds to a 9 eV peak in the experimental joint density of states, we find very close agreement with TiO UPS measurements [28] which show the oxygen 2p bands to lie ~8 eV below the fermi level. If the unoccupied d bands peak about a volt above ther fermi level as calculated, then our 9 eV peak is explained. The initial surface spectra shows the peak about one eV lower in energy which fits well with the UPS data as the TiO was reduced to TiO_2 showing a shift of the 2p band of about one eV closer to the fermi level. This fact corroborates our earlier conclusion from the AES measurements that the oxidized surface produced through oxygen bombardment is predominantly TiO while the initial surface was TiO_2. The UPS data also showed a depletion of the occupied d band region on going from TiO to TiO_2 which may account for the reduced reflectance in the 5-7 eV range with progressive oxygen exposure. The shift to lower energy of the peak identified with the 2s transitions is yet unexplained except to note that UPS measurements [27] have noted that the separation of the conduction band and 2s band decreases on going from TiO to TiO_2.

Conclusions and Recommendations

The first and most obvious conclusion of this research is that surface contamination, specifically oxide layers, can produce dramatic qualitative, as well as quantitative, changes in the VUV reflectance

spectra of a metal. Experimental methods for measuring the optical properties of a solid must include techniques for the preparation and maintenance of a clean surface, and for monitoring possible contamination of that surface. Auger electron spectroscopy has proved to be a sensitive monitor of surface composition and is highly compatible with the experimental optical apparatus. Ultrahigh vacuum techniques combined with in situ annealing and inert ion sputtering of the sample are found to be satisfactory for producing and maintaining clean surfaces for optical measurements. The use of synchrotron radiation as a light source in the VUV provides superior signal to noise ratios for optical measurements.

Automated acquisition of both optical and AES data allow close correlation of the results, which have permitted the identification of structure in the optical spectra with specific absorbed species on the sample surface. Previously reported unidentified peaks in the reflectance of titanium near 10 eV and 25 eV have been identified as transitions involving the 2p and 2s bands of absorbed oxygen. From shifts in the optical peak positions plus AES lineshapes and relative heights we have concluded that titanium samples prepared in air are covered by a predominantly TiO_2 surface layer, while titanium oxidized at very low oxygen exposures or by oxygen ion bombardment have a predominantly TiO surface layer.

Optical constants generated by Kramers-Kronig analysis of the reflectance of clean titanium are significantly different from previous reported values due to oxide contamination in the latter, and are in qualitative agreement with the band structure calculations of Hygh and Welch. However, assignment of peak structure must await refinements in

the calculations. A volume plasma frequency of ~15.5 eV was measured by both optical methods and energy loss methods; this value, 2 eV lower than the calculated free electron value, may be explained by the reduced mobility of the titanium d electrons. Additionally, the titanium 3p level has been measured to lie ~47 eV below the Fermi level.

The automated data acquisition apparatus developed in this work combined with the use of UHV techniques and synchrotron radiation will allow accurate optical measurements to be made on well characterized surfaces of many types. Most of the previously reported optical studies of metals and semiconductors paid little attention to surface contamination at the atomic level, and new measurements under controlled surface conditions would most likely provide more accurate data. The demonstrated ability to determine electronic structure of surface layers through optical measurements provides a method of studying absorbates on surfaces, especially as the affected surface region thicker beyond the depth normally studied by electron emission techniques.

The apparatus could be improved through two additional modifications. More accurate determinations of the optical constants could be made if a method, such as ellipsometry, for independently determining the optical constants at one or two discrete energies, was incorporated in the apparatus. Further improvement could be realized by the addition of a monochromator and detector to extend the measurements into the infrared. This would not only allow measurements of low energy transitions but also improve the Kramers-Kronig integration.

Finally, in regard to the work on titanium, we would recommend detailed optical measurements of the oxides of titanium, plus further

surface studies using thermal oxidation of titanium. From these studies, one could expect to develop a better understanding of the oxidation process. Through quantitative analysis of the thin film equations, one could determine thicknesses of different oxide species on the surface as the layer grows.

APPENDIX A

COMPUTER INTERFACES

The coupling of the DEC PDP-8/L to the various instruments in the apparatus is accomplished through individual interface units designed for each instrument. The interface units connect in parallel to the positive logic input-output bus of the computer and are designed to provide the proper input or output signals to each instrument. The input-output bus consists of an input data bus, an output data bus, a control bus; a program interrupt line and a skip line. The three buses consist of 12 bit parallel lines. A detailed description of the computer and bus structure may be found in the PDP-8/L Users Handbook [75].

Each interface unit must recognize its own two digit octal device select code that is placed on the control bus when the computer needs to address it. Additionally, a third octal digit must be decoded to determine the specific requested operation. Each individual instruction to the interface consists of a four digit octal word consisting of a six (indicating the word is an interface instruction); the two digit device select code, and the single digit operation code.

If an interface needs the attention of the computer, it requests it by grounding the common program interrupt line. The computer acknowledges the interrupt by polling each interface unit; the one requesting the interrupt responds to the poll by grounding the skip line. Data is transferred to or from the interface on the output or input bus when the

proper command is given by the computer.

All of the interfaces are constructed on printed circuit boards using wire-wrap techniques. All components are TTL or TTL compatible logic elements. The interfaces are mounted on a common panel that connects to the computer bus. Each interface will be described briefly with a logic diagram and instruction set presented afterwards.

Scaler Interface

The Ortec 715 dual scaler is equipped with output and control circuitry for use with an Ortec 432A printout control. The scaler interface emulates the printout control by providing the proper prinout initiation command sequence to the scalers, reads the scalers digit by digit providing a print advance command after reading each digit, and provides reset and grating signals as needed. In order to begin a printout sequence, the scalers must receive a "print" command followed by a "previous module finished" command at least 250 μsec later. The delay is necessary to allow the scaler logic to settle. This sequence is generated in the interface after it receives a "start read cycle" command from the computer. Data is then read digit by digit, buffered through the interface, by the computer. The interface produces an "advance digit" signal for the scalers after each "read digit" command. A single "start count" command from the computer initiates both a "reset" signal and "enable gates" signal to the scalers. When either scaler reaches its present maximum count, both scalers are disabled and a "system gate" signal from the scaler to the interface causes the interface to generate a program interrupt signal to the computer. The computer acknowledges the interrupt by

polling the interfaces as described. The instruction set and logic diagram for this interface is presented in Table A-1 and Figure 25, respectively. This interface was designed and constructed by Samuel K. Formby and the author.

Stepping Motor Interface

The stepping motor interface provides either a "step forward" or "step backward" pulse of ~1 μsec duration to the stepping motor controller. Since we wish to limit the maximum stepping rate of the motor to one thousand steps per second, the computer must command the interface to step only once every millisecond. So that we may eliminate the time-keeping task from the computer, a 1 msec timer has been built into the interface. The timer starts at the receipt of a step command and then sigals the computer via the program interrupt when the time period has elapsed, allowing the next step command to be given. This interface, also designed by S. K. Formby and the author, is constructed on the same printed circuit board as the scaler interface and utilizes some common command decoding circuitry. The logic diagram is shown with the scaler interface, while the instruction set is presented in Table A-2.

Clock Interface

The interface is the simplest possible real time clock. A Schmidt trigger toggled by a full-wave rectified A.C. line voltage provides an output pulse every 120^{th} of a second (every 8.33 msec). When the clock is enabled by command from the computer, the output pulse from the Schmidt trigger creates a program interrupt every 8.33 msec. The computer may keep track of time intervals by counting the number of interrupts caused by the clock. An inherent error of one time interval

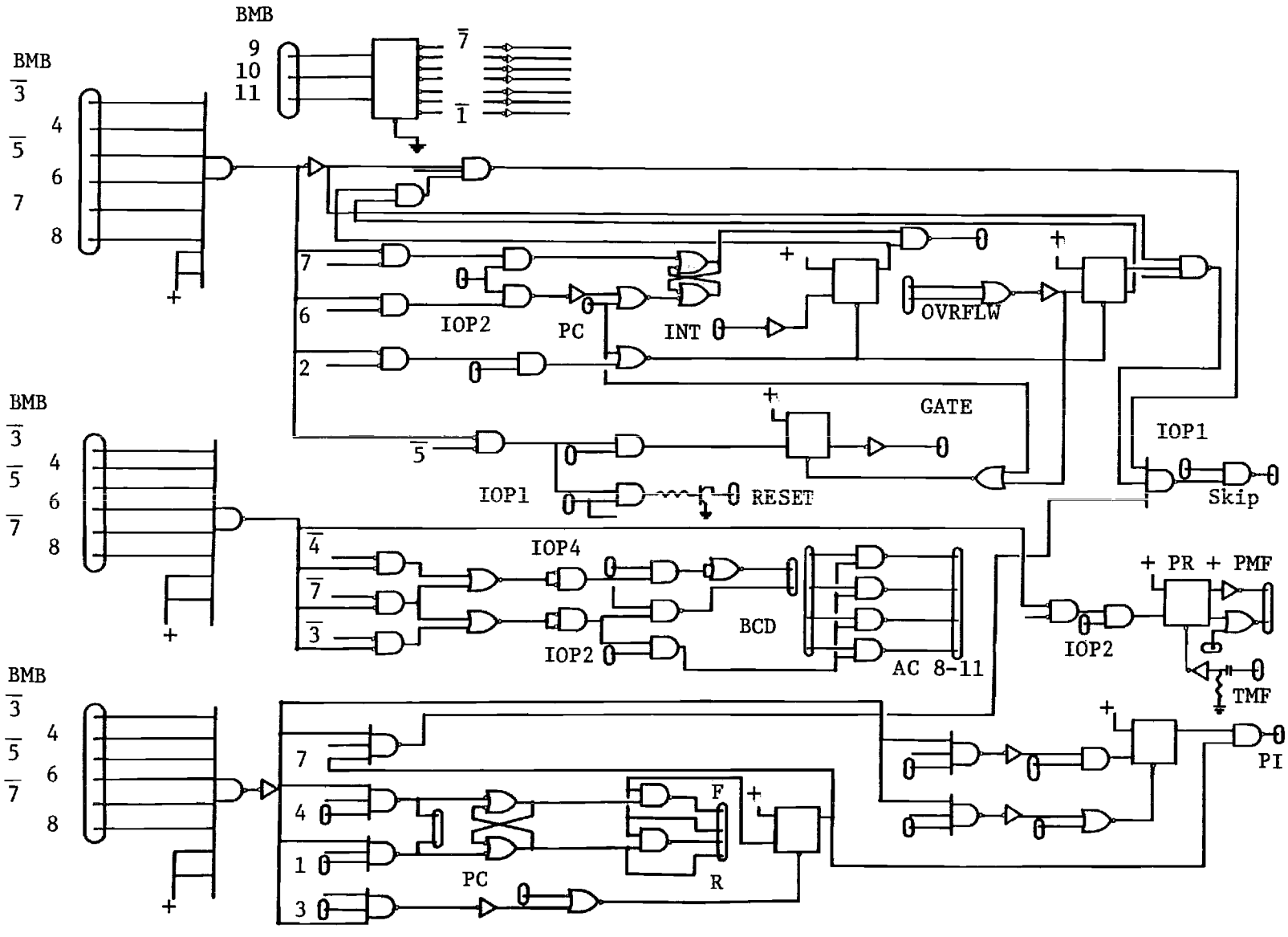

Figure 25. Scaler and Stepping Motor Interface Logic Diagram

exists in the clock since the length of the first interval after enabling the clock but before a pulse occurs is unknown. This error is insignificant over the time period of seconds that is measured while collecting optical data. We note that the relatively simple decoding and interrupt structure of this interface is the same as that used on more complex interfaces. The logic diagram is shown in Figure 26 while the instruction set is provided in Table A-3.

Auger Control Interface

The Auger control interface provides an analog control voltage to the CMA control unit that determines the passband energy of the CMA. The interface also converts the analog output of the lock-in amplifier to a digital number that can be read by the computer. The CMA control voltage is generated by an Analog Devices (DAC-16 QG) 16 bit digital to analog converter. Since the word length and output bus of the PDP 8/L is only 12 bits wide, a separate 4 bit register is contained on the interface to hold the four most significant bits. This register is loaded by a separate command prior to loading the lower 12 bits. In normal operation the control voltage is scanned by sequentially incrementing the voltage after a certain time interval has elapsed; therefore, a timer similar to that used in the stepping motor interface generates an interrupt when a fixed interval has elapsed after the load command. While this interval is adjustable, a period of approximately 1 msec has proved a good compromise among data acquisition time, signal to noise ratio, and processor utilization time.

The analog to digital conversion is done by an Analog Devices

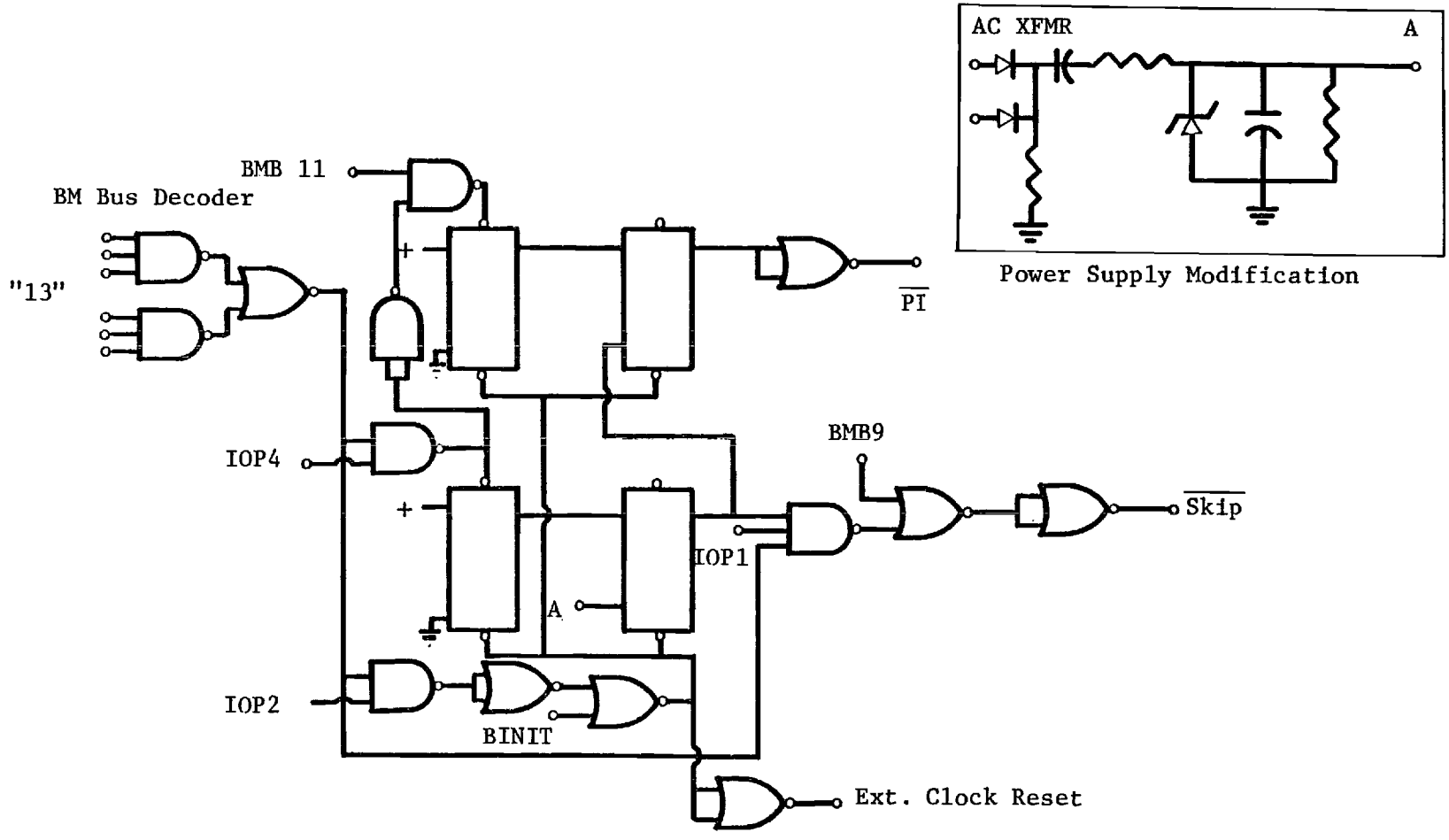

Figure 26. Clock Interface Logic Diagram

(ADC 1103) 12 bit converter. A "conversion" command starts the conversion process which takes a maximum time of 3-5 μsec. This number is held in the converter until a "read" command is received. Additional circuitry allows an external signal to start the conversion process and also generate an interrupt so that the computer starts the "read" sequence. This feature was incorporated in the design to allow the addition of an automated rotating ellipsometer where timing signals generated by the rotating polarizer would produce measurements at specific angles of the polarizer. This interface was designed and constructed by Bruce Biskey and the author. The logic diagram and instruction set are presented in Figure 27 and Table A-4, respectively.

Display Interface

The display interface, which will drive both a scope display and an x-y plotter is based on two ten bit digital-to-analog converters. Two ten bit registers allow loading of the value of each axis separately. An "intensify" command provides a signal that will intensify the scope display for ~3 μsec after a 10 μsec delay for the ADC's to settle. Using this method, a graph is displayed point by point at rates of up to 30 thousand points per second, giving an apparently continuous display. The interface is also used with an x-y plotter of the type that provides a signal when it has completed plotting a point. A "plot" command after the x and y values are loaded instructs the plotter to plot that point. Upon completion, the plotter returns a signal to the interface which generates an interrupt. After the computer acknowledges the interrupt, the interface may be connected to both output devices simultaneously.

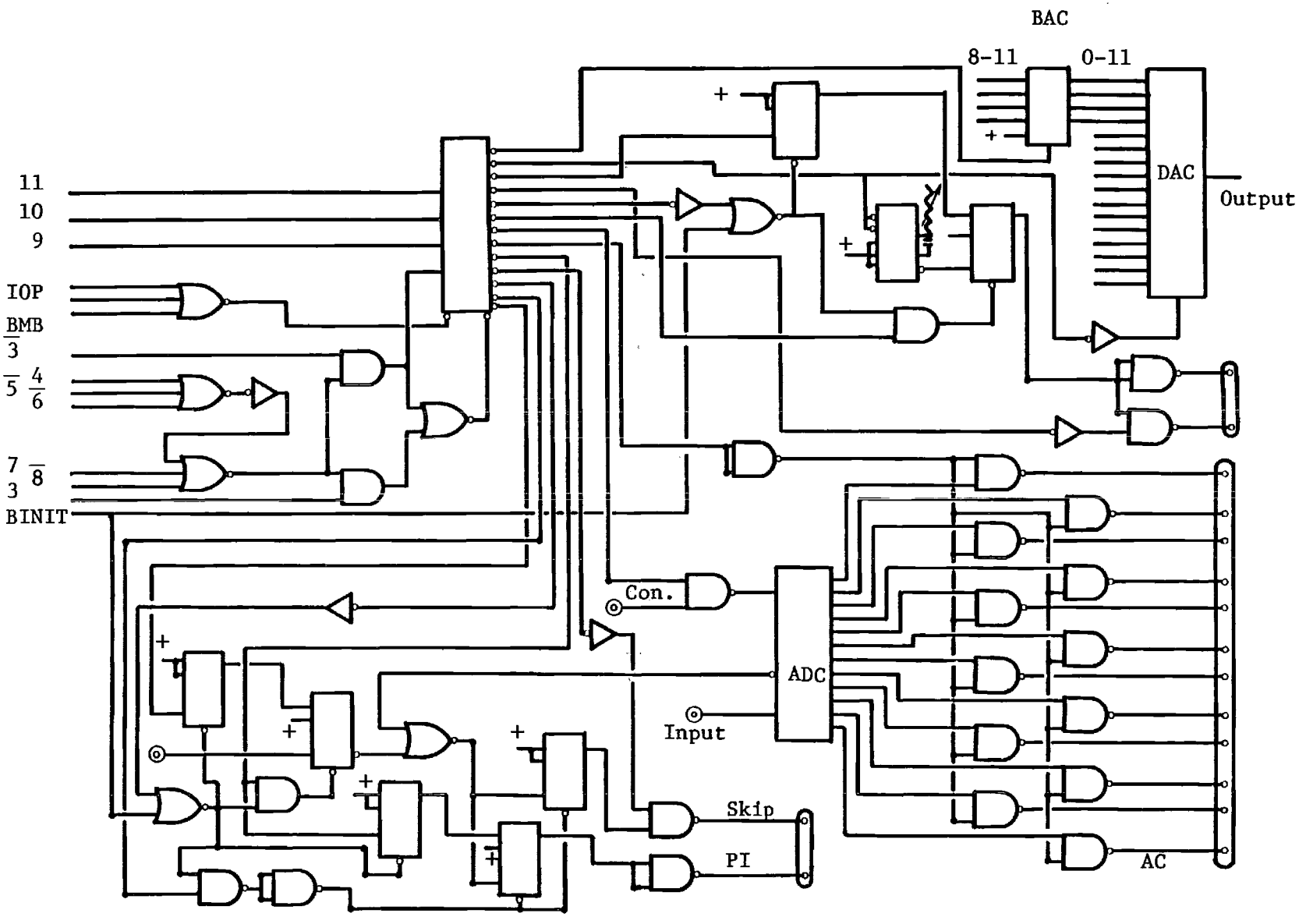

Figure 27. Auger Control Interface Logic Diagram

The design also incorporates commands for operation of a storage scope including commands for turning the storage function on and off plus erase command. This interface was designed and constructed by Bruce Biskey. The logic diagram is presented in Figure 28 and the instruction set in Table A-5.

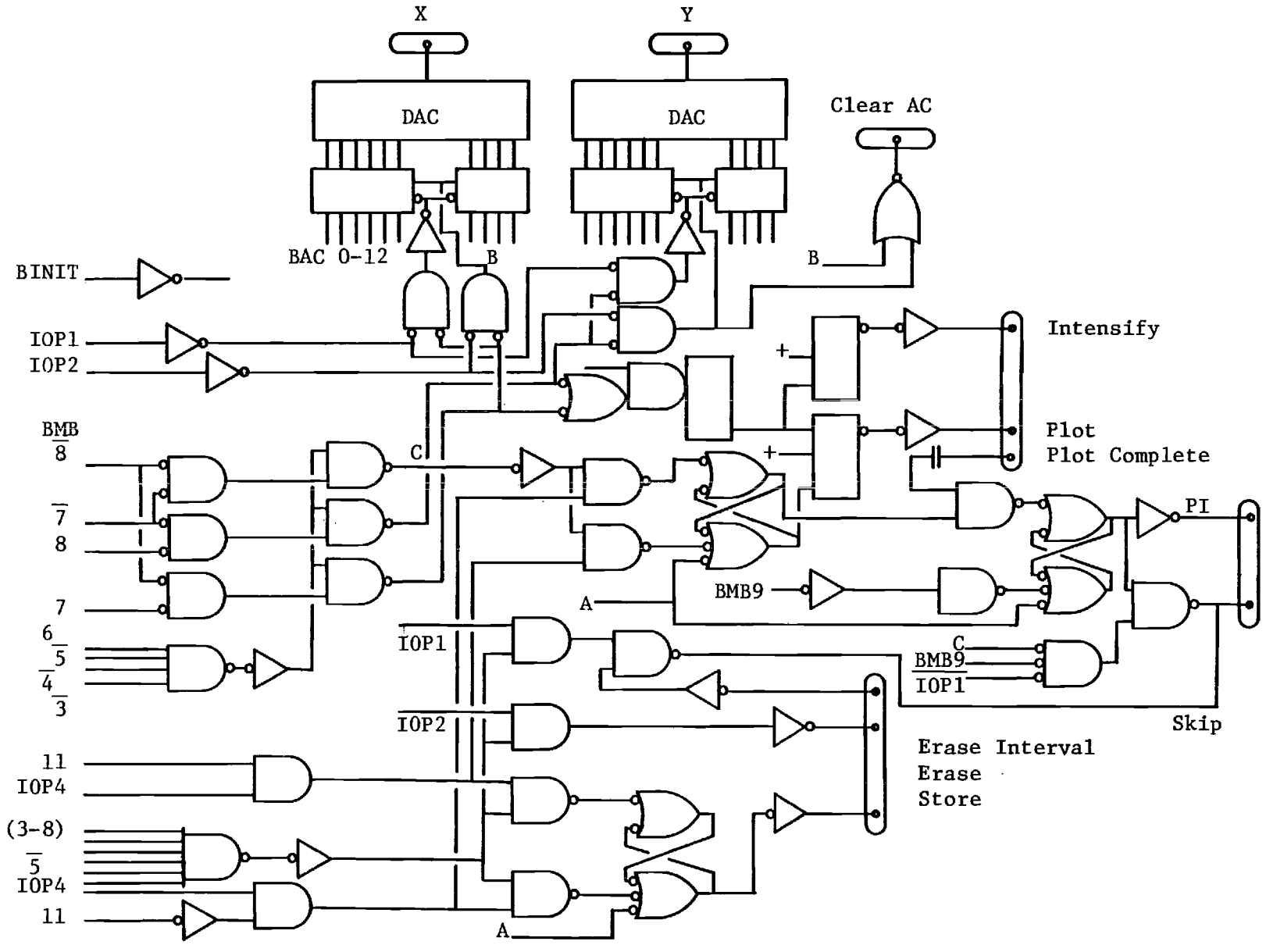

Figure 28. Display Interface Logic Diagram

Table A-1. Scaler Interface Instruction Set.

6522	Start read cycle
6523	Clear AC • Read digit
6524	Advance digit
6527	6523 • 6524
6531	Skip on counter maximum
6532	Clear flag
6535	Clear scalers • Start count
6536	Program interrupt disable
6537	Program interrupt enable

Table A-2. Stepping Motor Interface Instruction Set

6511	Step backward
6513	Clear flag
6514	Step forward
6515	Program interrupt enable
6516	Program interrupt disable
6517	Skip on finished flag

Table A-3. Clock Interface Instruction Set

6132	Clear flags • Disable clock and program interrupt
6136	Clear flags • Reset and enable clock
6137	6136 • Program interrupt enable
6133	Skip on clock • Clear flags • Disable

Table A-4. Auger Interface Instruction Set

6551	Load 4 MSB into DAC register
6552	Load DAC • Start timer
6553	Program interrupt enable (DAC)
6554	Skip on delay time out
6555	Program interrupt disable (DAC)
6556	Clear flags (DAC)
6151	Convert ADC
6152	Read ADC
6153	Program interrupt enable (ADC)
6154	Skip on external convert command
6155	Program interrupt disable (ADC)
6156	Clear flags (ADC)
6157	Enable skip (ADC)

Note: On the ADC a skip or program interrupt will occur on an external convert command only after first being enabled and then receiving an external "Get Ready" pulse.

Table A-5. Display Interface Instruction Set

6051	Clear x buffer
6052	Load x
6053	6051 • 6052
6054	Intensify point
6055	6051 • 6054
6056	6052 • 6054
6057	6051 • 6052 • 6054
6061	Clear y buffer
6062	Load y
6063	6061 • 6062
6064	Intensify point
6065	6061 • 6064
6064	6062 • 6064
6067	6061 • 6062 • 6064
6071	Skip on plot complete
6072	Clear flags
6073	6071 • 6072
6074	Plot enable
6075	Plot disable
6101	Skip on erase interval
6102	Erase
6103	6101 • 6102
6104	Storage off
6105	Storage on
6106	6102 • 6104
6107	6101 • 6102 • 6104

APPENDIX B

COMPUTER SOFTWARE

General Description

The software for the PDP 8/L is written completely in assembly language since the entire control program and data arrays must be contained in 8K of memory. The memory limitation also forced the simplification of some programs and elimination of some desired features. The final result is an operating system that controls both the reflectometer and Auger spectrometer, but provides little in the way of data analysis.

PDP 8/L assembly language is described fully in the DEC publications Introduction to Programming [76] and Small Computer Handbook [77] and will not be discussed here. Instead, we will give a general description of the operating system and show the relationship of the software to the hardware. The software that directly controls some of the hardware will be presented, and program execution of the principal tasks is discussed.

The operating system is written as a group of modular interrelated subroutines, and is constructed so that the computer can perform a number of specific "tasks" consisting of one or more subroutines. One particular task is the display task which is a single subroutine that reads data point by point from a memory array and displays it on an oscilloscope. This task executes continuously until another task is activated. In Chapter III, we described the system as command initiated and device

interrupt driven. The meaning of this description can be seen if we follow the sequence of events leading to the execution of a specific task. With the system in a standby condition, that is only the display task active, typing a command on the keyboard generates a program interrupt (PI) halting the display task and transferring control to the PI polling subroutine. This routine identifies the keyboard as the source of the PI and transfers control to the "keyboard monitor" subroutine. If this routine is not expecting a character for some data input routine, control is then transferred to the command decoder. The command decoder checks to see that it is a valid command, identifies the command, and transfers control to the appropriate task, for instance the "reflectance" task. In the reflectance task, the monochromator must be adjusted to the proper wavelength. This value is calculated from previously stored parameters and control is passed to the "run motor" subroutine which decides which direction and how many steps the motor must move. A command to the stepping motor interface from the "run motor" subroutine steps the motor one step and starts the interface timer. Control is then passed from the "run motor" subroutine back to the display subroutine which takes up where it was interrupted. The time elapsed from the receipt of the PI to return to the display routine is ~200 μsec, not enough to cause even a flicker on the display. When the stepping motor interface timer times out ~1 msec later, a PI is generated; control again passes to the polling subroutine which determines that the motor interface caused the PI, and transfers control to the stepping motor interrupt service routine, which again checks to see how many motor steps remain. The "next step" command is given and control passes again back to the display with the

time to service this routine reduced to ~40 μsec. This process continues until the monochromator is correctly positioned; at that time the motor service routine passes control back to the "reflectance" task which initiates the "start count" routine for the scalers, and then control reverts back to the display. The PI generated later when the scalers reach maximum count is identified by the polling routine, the scalers are read, reflectance calculated, and the entire process starts over for the next data point. We see from this description that all tasks except the display are initiated by a command, but that all depend on program interrupts for their execution. Figure 29 shows the flow sequence for the overall operating system, including the relationship of the command decoder and program interrupt to the various tasks.

All of the tasks operate in a manner similar to that described above, except for the computational and data manipulation tasks which do not produce any interrupts of their own. Once they are initiated by the command decoder they execute to completion and then return control to the display routine. Flow diagrams for the most important tasks are shown in Figures 30, 31, and 32. Some of the tasks require relatively precise numerical calculations which cannot be handled by simple 12 bit single precision calculations on the PDP 8/L. To accomplish these calculations, a floating point double precision computational software package developed by DEC was incorporated in the operating system. This package requires relatively long computational time (300-600 μsec per operation) and was used only where necessary.

The 8K of memory was organized so that all of the software including the floating point package resided in the lower 4K of memory,

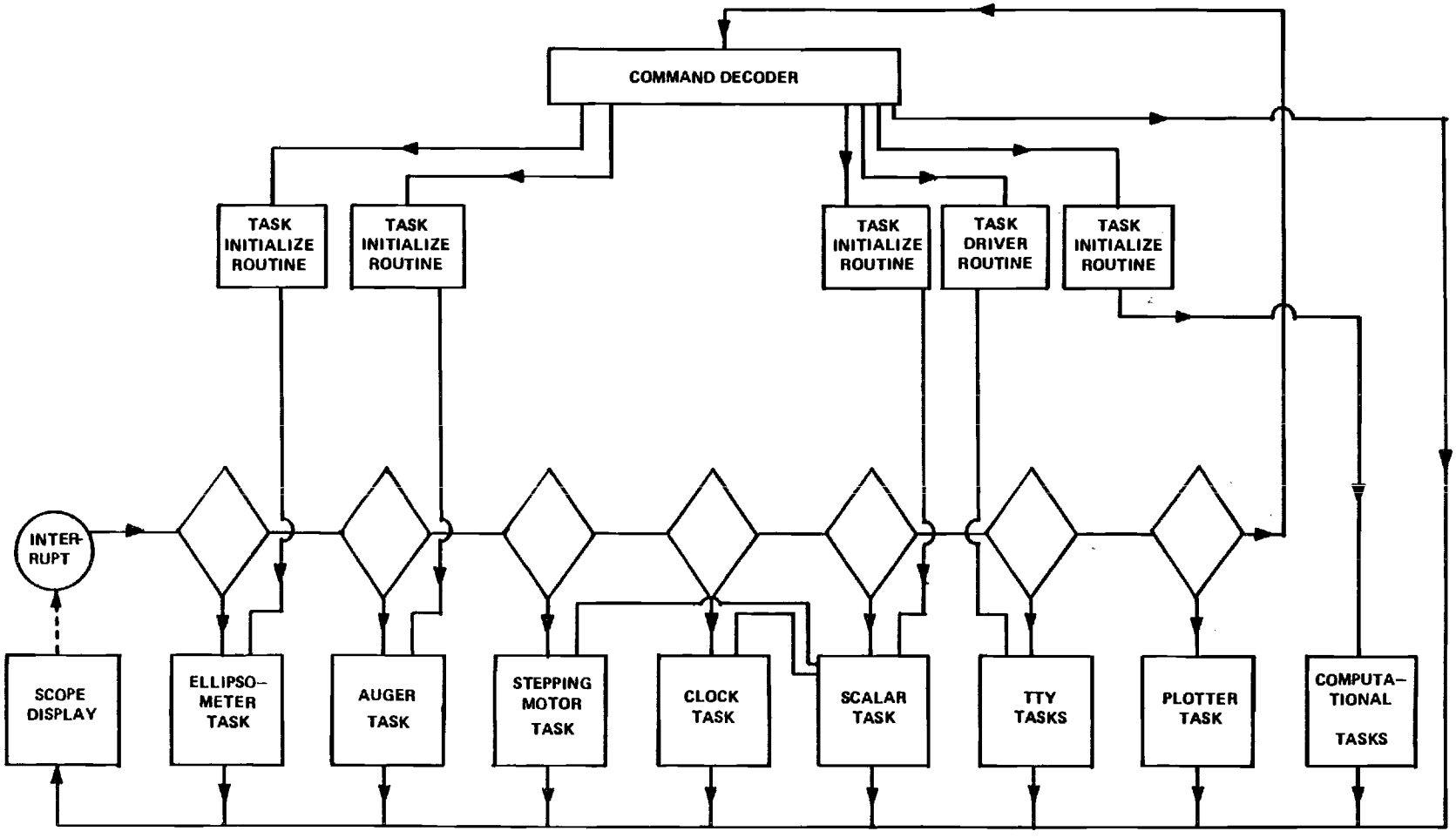

Figure 29. Operating System Flow Diagram

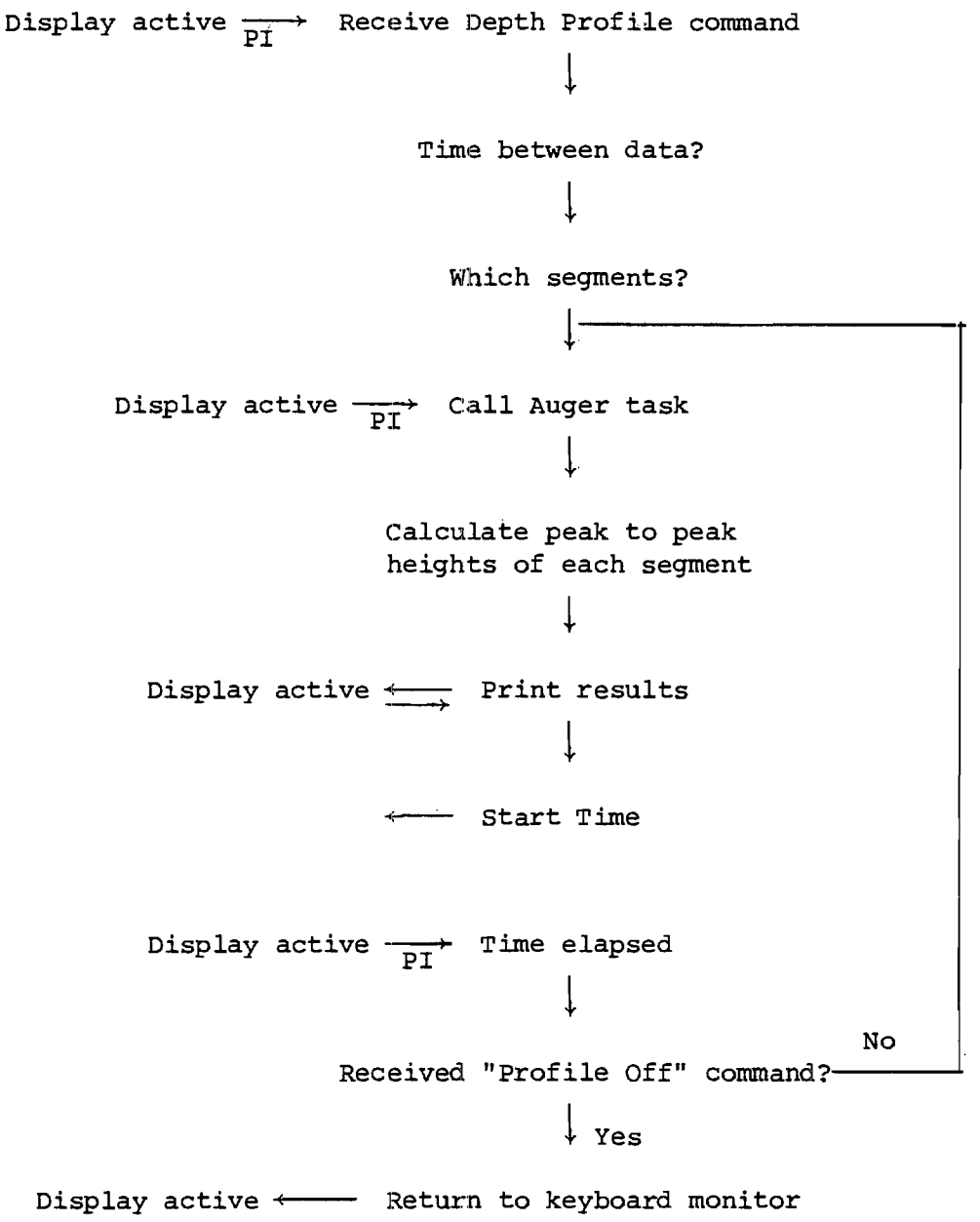

Figure 30. Depth Profile Task Flow Chart.

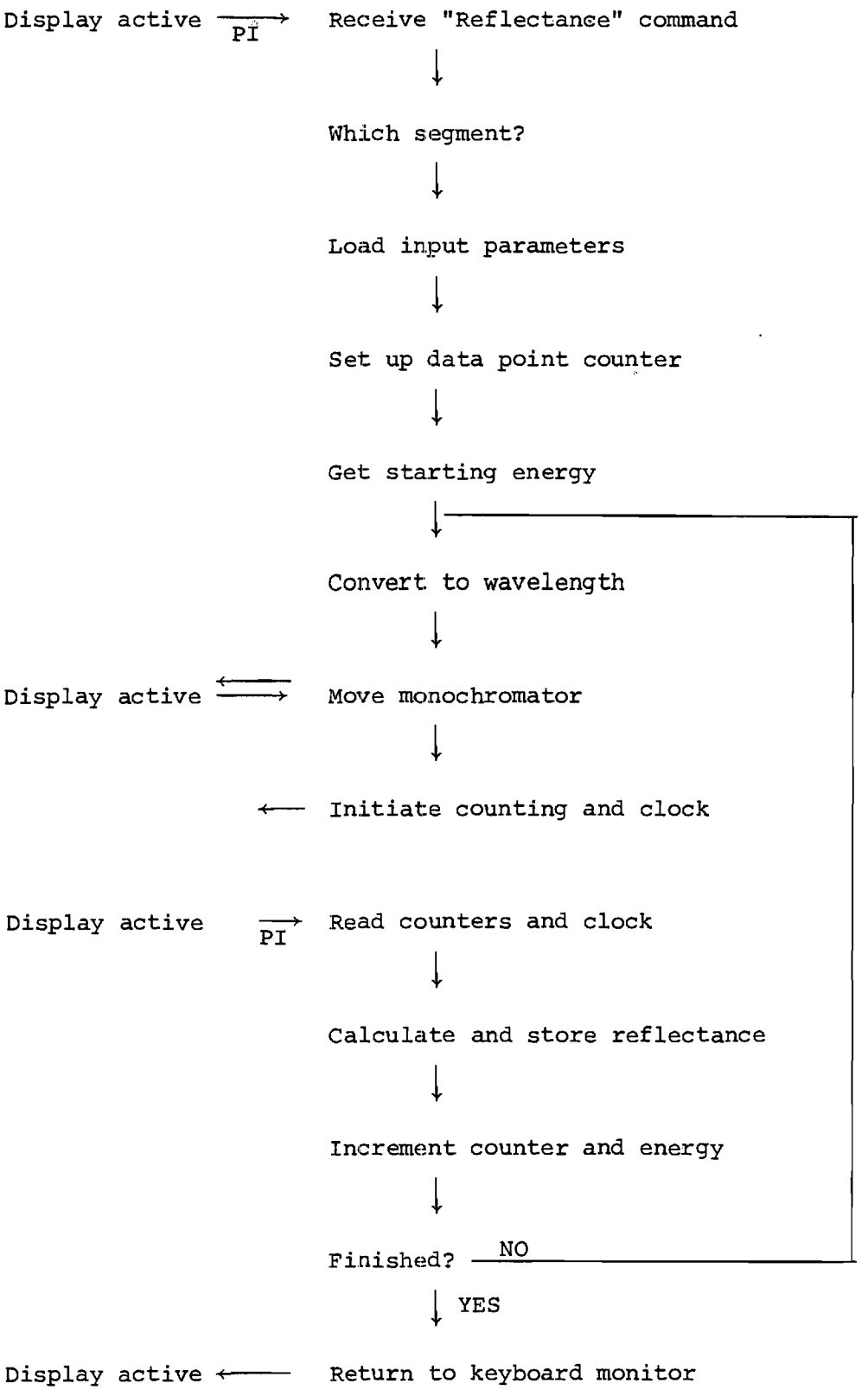

Figure 31. Reflectance Task Flow Chart.

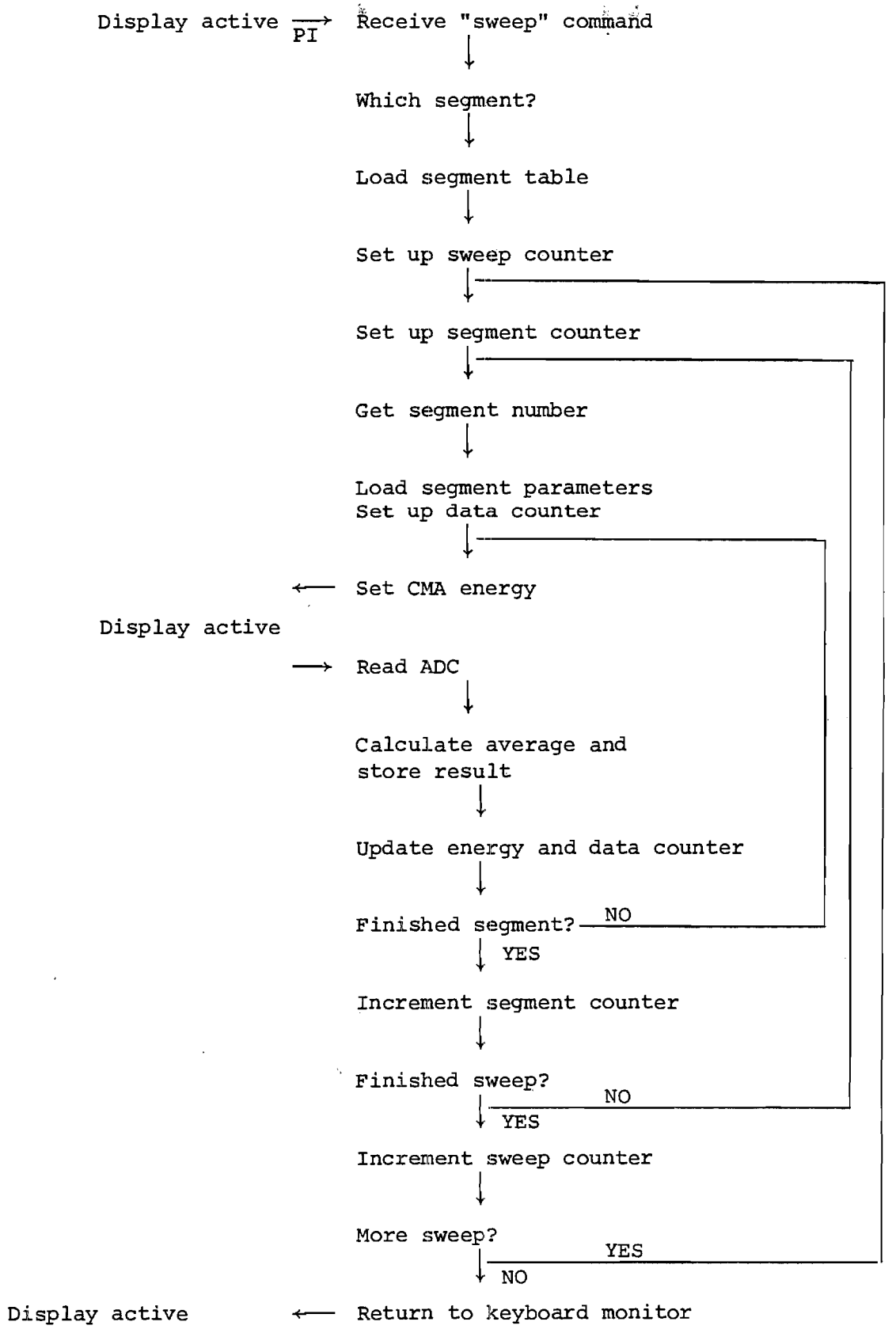

Figure 32. Auger Task Flow Chart.

reserving the upper 4K for data storage. DEC memory is organized into 32 pages of 128 words each per 4K field of memory. The page allocations for the lower 4K are shown in Table A-6. The upper 4K of memory contains six data arrays, two of which are general data storage arrays, M1 and M2, containing 511 data points each. Another array of 511 points, called the buffer array, is used for all the data manipulation and analysis routines. All calculation commands are directed towards this array. Two arrays are used for data accumulation: one for the Auger data and one for the reflectance data. Data may be accumulated in these arrays while other data is being examined or analyzed in the buffer array. The last array is a floating point array requiring 1536 words of memory to store the reflectometer calibration curve.

Operation

The operating system, even though it is kept very basic to conserve memory, is designed to minimize operator inconvenience and operator errors. The command decoder checks only the first two letters of a command, so that all commands may be abbreviated. The system types an asterisk to indicate that it is ready to accept a command; during the execution of a task, the operator may re-enter the command mode by typing an asterisk. Tasks requiring lengthy execution, such as a reflectance run, automatically re-enter the command mode when execution begins. New commands may then be given while the current task is executing; both tasks will execute simultaneously unless they interfere with each other. If an invalid command is entered, or if a command interferes with an executing task, an error message is returned to the operator. A list of the

Table A-6. Memory Allocations For the Operating System
(Page and Core Address Are in Octal)

Page	Core Address	Routine
0	0-177	Common variables
1	200-377	Display, Teletype control
2	400-577	Interrupt polling, Keyboard monitor
3	600-777	Command decoder
4	1000-1177	Calibration, Scaler input
5	1200-1377	Parameter
6-7	1400-1777	CMA sweep
10-11	2000-2377	Arithmetic functions
12	2400-2577	Command list, Parameter list
13	2600-2777	Reflectance, Incidence, Noise count
14	3000-3177	Housekeeping routines
15	3200-3377	Monochromator control
16	3400-3577	Clock control
17-20	3600-4177	Data printout
21	4200-4377	Data array manipulation
22	4400-4577	Depth profile
23	4600-4777	Data array commands
24	5000-5177	Numerical integration
25	5200-5377	(vacant)
26-36	5400-7577	Floating point package
37	7600-7777	Binary Loader

error codes is shown in Table A-7. The commands, their formats, and function are listed in Table A-8. Note that a command will not be executed until a space or carriage return is typed.

Table A-7. Operating System Error Codes

An error message consists of a single digit followed by a question mark.

Code	Error
0	Invalid command
1	Invalid termination after numerical input
2	Operation interferes with a previous command
3	Data array limits exceeded
4	Monochromator limits exceeded
5	Inappropriate data for current command

Table A-8. Table of Operating System Commands

A. Data Manipulation Commands

1. LOOK - AUGER
   - REFLEC
   or BUFFER

Directs scope display to desired array. If array is a reflectivity array, a colon is printed requesting segment to be displayed. Respond with 0-3 for those segments. Larger digit yields all segments.

2. CURSOR: _____

   Places cursor at point _____ on display. Cursor may be moved forward or backward using > or < keys on TTY

   CURSOR↵ Turns off cursor

3. EXPAND: _____

   Expands portion of display beginning at cursor by factor _____

4. PRINT — Prints buffer. If array in buffer is segmented, asks which segments you want printed.

5. PLOT — Plots data shown on scope.

6. GET — AUGER, REFLEC, M1, M2 — Gets contents of desired array and places in buffer

7. STORE — M1, M2 — Places contents of buffer in memory M1 or M2.

8. ADD — AUGER, REFLEC, M1, M2 — Adds desired array to contents of buffer

9. SUB — AUGER, REFLEC, M1, M2 — Subtracts desired array from contents of buffer

10. PEAK — Prints peak to peak height of each segment in buffer (only works on Auger data).

11. QUAD — Integrates contents of buffer, replacing buffer with scaled integral. Prints scaling factor (only works on Auger data).

B. Calibration and Parameter Commands

The calibration command must be executed before the parameter command.

1. CALIBRATION CMA
MONOCHR

When CMA is entered the CMA is first set to zero volts. Enter the energy observed on the CMA control energy readout (change signs from that read).

The CMA is then set to a high energy. Again enter minus the reading observed on the CMA control.

(Note the CMA control unit must be set to multiplex)

When MONO is entered, the current wavelength setting (in Å) is entered. Then the number of steps per Å (40 for the .3M MacPherson, 5 for the 1M GE) and the upper limit (10,000 for the MacPherson, 6000 for the GE).

(Note: After initial calibration, an abbreviated form may be used in which a CR is typed after the current location, the remaining data is then omitted.)

(Note: In general, a space after a number indicates more input coming, a CR indicates end of input. The machine ignores incorrect replies if they don't make sense.)

2. PARAMETER CMA
MONO
SWEEP

This command inputs operational parameters for the Auger and Reflectivity data taking routines.

CMA mode inputs data for Auger. The format is

```
: X      :      XXX.X      :    XXXX     space or CR
  ↑             ↑              ↑
segment     low starting     high
number        energy         energy
```

Data may be taken in segmented or continuous mode. Parameters for continuous mode are placed in segment 0.

Up to 7 segments may be used with varying resolution.

segment	number of points
1	128
2	128
3	64
4	64
5	64
6	32
7	32

Energy inputs are in free field form. A space after high energy indicates another segment to be inputed. A CR returns to command mode.

MONO mode inputs data for incident and reflectivity runs. The format is

```
: X      :    XXX.X     :   XX.XX    :   XXX.XX
  ↑             ↑             ↑            ↑
segment     low energy    increment    high energy
number        (eV)          (eV)         (eV)
```

There are four segments of 128 points maximum size (0-3).

The number of points are determined by the increment size. If there are more than 128 points, an error message is given as a warning, but it may be used by running over into the next segment. This destroys data in this segment but can be done. This will not work on segment 3.

SWEEP mode enters the number of Auger sweeps to be averaged over (15 is a good number).

C. Auger Data Taking Commands

1. SWEEP _____, _____, _____

   Sweeps segments _____, _____, _____

   This may be 1 to 7 segments (or segment 0 included).

   If the segment numbers are omitted, that is a SW, the previous argument is used.

2. DP Depth Profile

   This routine takes Auger data as in a SWEEP command, computes P-P height of each segment, waits an interval and repeats. This continues until the PO (Profile Off) command is given.

   (Note: To give PO command, an asterisk must first be typed to get to command mode.)

D. Reflectometer Commands

1. NOISE Does background noise count for one minute. Prints results.

   (Note: Light source should be shut off.)

2. INCID _____ Does incident data run on segment _____?

3. REFLEC _____ Does reflectivity data run on segment _____?

4. MOVE:_____ Moves monochromater to energy _____ in EV. If you enter _____A, it interprets it as wavelength in angstroms.

   (Note: A NOISE measurement should be made before the start of each reflectivity or incident run for best results.)

APPENDIX C

KRAMERS-KRONIG ANALYSIS PROGRAM

The following program, developed by I. R. Gatland and modified by Ronald Yanda, calculates the phase angle θ of the complex reflection coefficient $\tilde{r} = re^{i\theta}$ given the reflectance $R = |r|^2$ over a broad spectral range. The program uses the Kramers-Kronig relationship (Equation 2-24) for θ. From the calculated values of $\tilde{r}$, the complex index of refraction (n,k) and the complex dielectric constant ($\varepsilon_1, \varepsilon_2$) are computed. Additional quantities such as the joint density of states, the electron loss function and the sum rules (Equation 5-6 and 5-7) are then computed from the optical constants. The high energy extrapolation for R given in Equation (5-8) is integrated analytically to infinity and the correction added to θ. A similar procedure is used in computing the sum rules, eliminating the error caused by terminating the integral. The program computes the sum rules for a range of values of the extrapolation coefficient α. By narrowing this range, one can find the value that satisfies the sum rules.

The program requires the following input parameters: N, the number of points computed in the integral; EB, the high energy limit on the computation of the optical constants; EA, the low energy limit of the computation; K, a parameter of the quadratic fit of the reflectance data, usually 1; and M, the number of data points in the reflectance spectrum. The reflectance spectrum is entered energy first and then reflectance. The listing of the program follows.

```
MAIN
      PROGRAM MAIN(TAPE1,TAPE2,INPUT,OUTPUT,TAPE5=INPUT,TAPE6=OUTPUT)
      DIMENSION E(1000),RR(1000),R(1000),T(1000),S(1000),TT(1000)
      DIMENSION E1(1000),E2(1000),DST(1000),ELF(1000),EFFN(1000)
      DIMENSION RI1(1000),RI2(1000)
      DATA PI/3.14159265359/
      DATA CO/.2483946/
  100 FORMAT (A7)
  101 FORMAT (1X,7E10.3)
  102 FORMAT (1X,2I5,4E10.3)
  103 FORMAT (1X,4E10.3)
  104 FORMAT ("GOOD",3F10.5)
  105 FORMAT ("BAD",3F10.5)
  120 FORMAT (1X,A10,"ENERGY(EV)REFLECT")
  121 FORMAT (1X,A10,"ENERGY(EV)THETA")
  122 FORMAT (1X,A10,"ENERGY(EV)N")
  123 FORMAT (1X,A10,"ENERGY(EV)K")
  124 FORMAT (1X,A10,"ENERGY(EV)E1")
  125 FORMAT (1X,A10,"ENERGY(EV)E2")
  126 FORMAT (1X,A10,"ENERGY(EV)DENS STATE")
  127 FORMAT (1X,A10,"ENERGY(EV)ELECT LOSS")
  128 FORMAT (1X,A10,"ENERGY(EV)EFF")
      REWIND 1
      REWIND 2
      READ(1,100)NAME
      READ(1,*)N,EB,EA,K,M,(E(I),R(I),I=1,M)
      IF (EOF(1).NE.0.) STOP
      IF (E(1).LT.E(M)) GO TO 2
      M2=M/2
      DO 1 I=1,M2
      I1=M+1-I
      W=E(I)
      E(I)=E(I1)
      E(I1)=W
      W=R(I)
      R(I)=R(I1)
    1 R(I1)=W
    2 PRINT*,"M=",M," N=",N," EA=",EA," EB=",EB
      G=2.
      CALL PHASE(M,E,R,T,S,N,EA,EB,G,K,CK1C,2)
      PRINT*,CK1,CK2
   98 PRINT*,"SBS,SBF,SBI"
      READ*,SBS,SBF,SBI
      SB=SBS
   22 G=SB/2.
      S1=0.
      SX=0
      KNK=0
      S2=0
      DO 3 I=1,N
      TT(I)=T(I)+G*S(I)
```

```
      X=R(I)*COS(TT(I))
      Y=R(I)*SIN(TT(I))
      IF (R(I).GT.1.)R(I)=.999
      RR(I)=R(I)**2
      RI1(I)=(1-RR(I))/(1+RR(I)-2*X)
      RI2(i)=2.*Y/(1.+RR(I)-2.*X)
      IF ((RI1(I).LT.0.).OR.(RI2(I).LT.0))KNK=1
      S1=S1+(RI1(I)-1.)*E(I)
      S2=S2+(RI1(I)-1.)*RI2(I)*E(I)**2
      E1(I)=RI1(I)**2-RI2(I)**2
      E2(I)=2*RI1(I)*RI2(I)
      DST(I)=(E(I)**2)*E2(I)
      ELF(I)=E2(I)/((E1(I)**2)+(E2(I)**2))
      SX=SX+DST(I)
    3 EFFN(I)=SX*CO*ALOG(E(2)/E(1))
      S1=S1*ALOG(E(2)/E(1))+2.*R(N)*E(N)*COS(PI*G/2.)/(G-1.)
      S2=S2*ALOG(E(2)/E(1))+(R(N)*E(N))**2*SIN(PI*G)/(G-1.)
      IF (INK.EQ.1)GO TO 44
      WRITE (6,104(SB,S1,S2
   45 IF (SBI.EQ.0)GO TO 4
      IF (SB.GT.SBF)GO TO 98
      SB=SB+SBI
      TO TO 22
   44 WRITE (6,105)SB,S1,S2
      GO TO 45
    4 WRITE (2,'00)NAME
      WRITE (2,*)180
      WRITE (2,120)NAME
      WRITE (2,102)N,-1,EA,EB,0,1.
      WRITE (2,101)(E(I),RR(I),TT(I),RI2(I),E1(I),E2(I),I=1,N)
      WRITE (2,121)NAME
      WRITE (2,102)N,-2,EA,EB,0,3.2
      WRITE (2,122)NAME
      WRITE (2,102)N,-3,EA,EB,0,60.
      WRITE (2,123)NAME
      WRITE (2,102)N,-4,EA,EB,0,60.
      WRITE (2,124)NAME
      WRITE (2,102)N,-5,EA,EB,-10000.,10.
      WRITE (2,125)NAME
      WRITE (2,102)N,-6,EA,EB,0,1000.
      WRITE (2,126)NAME
      WRITE (2,102)N,0,EA,EB,0,0
      WRITE (2,126)NAME
      WRITE (2,102)N,-1,EA,EB,0,1000.
      WRITE (2,103)(E(I),DST(I),ELF(I),EFFN(I),I=1,N)
      WRITE (2,127)NAME
      WRITE (2,102)N,-2,EA,EB,0,10.
      WRITE (2,128)NAME
      WRITE (2,102)N,-3,EA,EB,0,1000.
      END
```

PHASE

```
      SUBROUTINE PHASE(M,E,R,T,S,N,EA,EB,G,K,CK1,CK2)
      DIMENSION E(1000),R(1000),T(1000),S(1000)
      DATA PI/3.14159265359/
      D=ALOG(EB/EA)/N
      C=ALOG(EA)-D/2.
      DO 1 I=1,M
      E(I)=ALOG(E(I))
1     T(I)=ALOG(R(I))/2.
      CALL QFIT(M,E,T,C,D,N,R,S,W,K)
      DE=EXP(D)
      W=1.
      E(1)=ALOG(4./D)+1
      CK1=.5*(S(N))
      CK2=.5*E(1)
      DO 2 I=2,N
      W=W*DE
      E(I)=ALOG((W+1.)/(W-1.))
      CK1=CK1+S(I)
2     CK2=CK2+E(I)
      CK1=CK1*D-(R(N)-R(1))
      CK2=CK2*D/PI+DILOG(EXP(C+D)/EB)-PI/4.
      DO 4 J=1,N
      W=0.
      DO 3 I=1,N
3     W=W+E(IABS(I-J)+1)*S*I)
4     T(J)=-W*D/PI
      W=EXP(C)
      DO 5 I=1,N
      W=W*DE
      E(I)=W
      R(I)=EXP(R(I))
5     S(I)=DILOG(E(I)/EB)
      RETURN
      END
```

QFIT

```
      SUBROUTINE QFIT(M,XV,YV,S0,DX,N,Y,S,C,K)
      DIMENSION XV(1000),YV(1000),Y(1000),S(1000)
      J=K+1
      DO 4 N1=1,N
      X=X0+N1*DX
1     IF (XV(J).GE.X.OR.J.GE.(M-K)) GO TO 2
      J=J+1
      GO TO 1
2     IF (ABS(X-XV(J-1)).LT.ABS(X-XV(J)).AND.J.GT.(K+1)) J=J-1
      S0=S1=S2=S3=S4=T0=T1=T2=0.
      J1=J-K
      J2=J+K
      DO 3 I=J1,J2
      XJ=XV(I)-X
      XJ2=XJ**2
      YJ=YV(I)-YV(J)
```

```
          S0=S0+1.
          S1=S1+XJ
          S2=S2+J2
          S3=S3+J*XJ2
          S4=S4+XJ2**2
          T0=T0+YJ
          T1=T1+YJ*XJ
      3   T2=T2+YJ*XJ2
          D=S1*(S2*S3-S1*S4)+S2*(X0*S4-S2*S2)+S3*(S1*S2-S0*S3)
          Y(N1)=(T0*(S2*S4-S3*S3)+T1*(S2*S3-S1*S4)+T2*(S1*S3-S2*S2))/D
          S(N1)=(T0*(S2*S3-S1*S4)+T1*(S0*S4-S2*S2)+T2*(S1*S2-S0*S3))/D
          C=(T0*(S1*S3-S2*S2)+T1*(S1*S2-S0*S3)+T2*(S0*S2-S1*S1))/D
      4   YN(1)=Y(N1)+YV(J)
          RETURN
          END
DILOG
          FUNCTION DILOG(X)
          DATA PI/3.14159265359/
          Y=ABS(X)
          DILOG=SIGN(PI/4.,X)
          IF (Y.EQ.1.) RETURN
          IF (Y.GT.1.) Y=1./Y
          S=0.
          IF(Y.LT.0.5) GO TO 1
          S=PI**2/8.+.5*ALOG((1.+Y)/(.1-Y))*ALOG(Y)
          Y=-(1.-Y)/(1.+Y)
      1   Y2=Y*Y
          DO 2 M=1,31,2
          S=S+Y/M**2
      2   Y=Y*Y2
          DILOG=S*2./PI
          IF(ABS(X).GT.1.)DILOG=PI/2.-DILOG
          IF (X.LT.0.) DILOG=-DILOG
          RETURN
          END
```

BIBLIOGRAPHY

1. M. Prutton, Surface Physics, Oxford Univ. Press, Oxford (1975).

2. T. L. Loucks, Augmented Plane Wave Method, (Benjamin, New York, 1967).

3. L. F. Mattheiss, Phys. Rev. B 1, 373 (1970).

4. J. M. Ziman, Principles of the Theory of Solids, (Cambridge Univ. Press, London, 1972).

5. J. H. Weaver, D. W. Lynch, and C. G. Olson, Phys. Rev. B 7, 4311 (1973).

6. J. H. Weaver, D. W. Lynch, and C. G. Olson, Phys. Rev. B 10, 501 (1974).

7. D. W. Lynch, C. G. Olson, and J. H. Weaver, Phys. Rev. B 11, 3617 (1975).

8. C. R. Hammond, in Handbook of Chemistry and Physics, 57th ed., (CRC Press, Cleveland, 1976).

9. J. B. Cotton, in Titanium Science and Technology (Plenum, New York, 1973).

10. A. O. E. Animalu, Bull. Am. Phys. Soc. 21, 432 (1976).

11. L. F. Mattheiss, Phys. Rev. 134 A970 (1964).

12. E. H. Hygh and Ronald M. Welch, Phys. Rev. B 1, 2424 (1970).

13. E. H. Hygh and Ronald M. Welch, Phys. Rev. B 4, 4261 (1971).

14. R. M. Welch and E. H. Hygh, Phys. Rev. B 9, 1993 (1974).

15. S. L. Altman and C. J. Bradley, Proc. Phys. Soc. 92, 764 (1967).

16. D. E. Eastman, Solid State Commun. 7, 1697 (1969).

17. G. A. Bolotin, A. N. Voloshinskh, M. M. Kirillcva, M. M. Noskov, A. V. Sokolov, and B. A. Charikov, Phys. Met. Metallogr. 13, No. 6, 24 (1969),

18. M. M. Kirillova and B. A. Charikov, Phys. Met. Metallogr. 19, No. 4, 13 (1969).

19. I. D. Mash and G. P. Motulevich, Sov. Phys. JEIP 36, 516 (1973).

20. G. Hass and A. P. Bradford, J. Opt. Soc. Am. 47, 125 (1957).

21. P. B. Johnson and R. W. Christy, Phys. Rev. B 9, 5056 (1974).

22. T. Smith, J. Opt. Soc. Am. 52 427 (1962).

23. T. Smith, Surface Sci. 38, 292 (1973).

24. J. Kucirek, Czech J. Phys. B 23, 1382 (1973).

25. F. Gervais and B. Piriou, Phys. Rev. B 10, 1642 (1974).

26. S. M. Lu, F. H. Pollak, P. M. Raccah, Bull. Am. Phys. Soc. 21, 366 (1976).

27. K. Ichikauri, O. Terasaki, and T. Sagawa, J. Phys. Soc. Japan 36, 706 (1974).

28. V. E. Henrich, H. J. Zeiger, and T. B. Reed, Phys. Rev. B (to be published).

29. D. W. Fischer, J. Appl. Phys. 41, 3561 (1970).

30. V. Ern and A. C. Switendick, Phys. Rev. 137 A1927 (1965).

31. D. R. Jennison and A. B. Kunz, Phys. Rev. Lett. 39, 418 (1977).

32. G. R. Fowles, Introduction to Modern Optics, (Holt, Rinehart, and Winston, New York, 1968).

33. M. Zivitz, Doctoral Thesis, Georgia Institute of Technology (1973).

34. F. C. Brown, The Physics of Solids, (Benjamin, New York, 1967).

35. W. Jones and N. H. March, Theoretical Solid State Physics Volt2, (Wiley, New York, 1973).

36. F. Seitz, The Modern Theory of Solids, (McGraw-Hill, New York, 1940).

37. D. Bohm and D. Pines, Phys. Rev. 82, 625 (1951); 85, 338 (1952); 92, 609 (1953).

38. A. J. Dekker, Solid State Physics, (Prentice-Hall, New Jersey).

39. P. Nozieres and D. Pines, Phys. Rev. 109, 1062 (1958).

40. P. Nozieres and D. Pines, Phys. Rev. 113, 1254 (1959).

41. M. H. Cohen, Phil. Mag. 3, 762 (1958).

42. F. Bassani and G. P. Parravicini, Electronic States and Optical Transitions in Solids (Pergamon, Oxford, 1975).

43. J. C. Sutherland, Doctoral Thesis, Georgia Instititue of Technology (1967).

44. R. H. Ritchie, Surface Sci. 34, 1 (1973).

45. J. M. Elson and R. H. Ritchie, Phys. Rev. B 4, 4129 (1971).

46. J. G. Endriz and W. E. Spicer, Phys. Rev. B 4, 4144 (1971).

47. G. Rusigni, M. Rasigni, and J. P. Palmari, Phys. Rev. B 14, 4235 (1976).

48. J. D. E. McIntyre, in Optical Properties of Solids--New Developments, (North Holland, Amsterdam, 1976).

49. H. Raether, Surface Sci. 8, 233 (1967).

50. C. C. Chang, in Characterization of Solid Surfaces, (Plenum, New York, 1974).

51. A. Joshi, L. E. Davis, and P. W. Palmberg, in Methods of Surface Analysis, (Elsevier, Amsterdam, 1975).

52. H. Ellis, Doctoral Thesis, Georgia Institute of Technology (1974).

53. J. A. R. Samson, Vacuum Ultraviolet Spectroscopy, (Wiley, New York, 1967).

54. C. H. Pruett, N. C. Lien, and J. D. Stebben, Third Int. Conf. on Vacuum Ultraviolet Radiation Physics, Tokyo, Japan, 30 August - 2 September 1971.

55. M. Windholz, ed., The Merck Index, (Merck, Rahway, NJ, 1976).

56. M. Baldwin and J. Pope, SSRP User Specifications for Vacuum Systems, (Stanford University, 1973).

57. J. Carden, F. Ferrandino, J. Larsen, W. Wall, and J. R. Stevenson, in Proceedings of the IV International Conference on Vacuum Ultraviolet Radiation Physics (Pergamon, Oxford, 1975).

58. A. N. Zaidel and E. Ya. Shreider, Vacuum Ultraviolet Spectroscopy, (Halsted Press, New York, 1970).

59. Princeton Applied Research Corp., Photon Counting (PARC, Princeton, NJ, 1975).

60. H. D. Shih, K. O. Legg, and F. Jona, Surface Sci. 54, 355 (1976).

61. H. D. Shih, F. Jona, D. W. Jepsen, and P. M. Marcus, J. Phys. C: Solid State Phys. 9, 1405 (1976).

62. D. W. Palmberg, G. E. Riach, R. E. Weber, N. C. MacDonald, Handbook of Auger Electron Spectroscopy, (Phys. Elec. Ind., Edina, Minn., 1972).

63. L. W. Davis, N. C. MacDonald, P. W. Palmburg, G. E. Riach, R. E. Weaver, Handbook of Auger Electron Spectroscopy 2nd Ed., (Phys. Elec. Ind., Edina, Minn., 1976).

64. From analysis provided with the sample material supplied by Materials Research Corporation.

65. J. S. Solomon, W. L. Baun, Surface Sci. 51, 228 (1975).

66. H. D. Shih and F. Jona, J. Appl. Phys. 12, 311 (1977).

67. D. A. Shirley, R. L. Martin, S. P. Kowalezyk, E. R. McFeely, and L. Ley, Phys. Rev. B 15, 544 (1977).

68. M. Alterelli, D. L. Dexter, H. M. Nussenzveig, and D. Y. Smith, Phys. Rev. B 6, 4502 (1972).

69. I. R. Gatland, private communication.

70. P. E. Best, Proc. Phys. Soc. (London) 80, 1308 (1962).

71. J. L. Robins and J. B. Swan, Proc. Phys. Soc. (London) 76, 857 (1960).

72. G. W. Simmons and E. J. Scheibner, J. Appl. Phys. 43, 693 (1972).

73. M. W. Ribarsky, private communication.

74. W. E. Wall, M. W. Ribarsky, J. R. Stevenson, Surface Sci., to be published.

75. PDP-8/L Users Handbook (Digital Equipment Corp., Maynard, Mass., 1968).

76. Introduction to Programming (Digital Equipment Corp., Maynard, Mass., 1975).

77. Small Computer Handbook (Digital Equipment Corp., Maynard, Mass., 1967).

VITA

William Edgar Wall, Jr., the oldest of two sons of William E. and Sarah H. Wall, was born December 23, 1947 in Columbia, South Carolina. Mr. Wall attended public schools in Columbia, graduating from A. C. Flora High School in 1966. Entering the Georgia Institute of Technology in fall of 1966, he received his B.S. in Physics in June 1970.

Following graduation, he entered the United States Army and served three years in the Signal Corp, including a tour of duty in South Vietnam.

Mr. Wall entered graduate school at the Georgia Institute of Technology in 1974. During his graduate education he has served as both a teaching and a research assistant in the School of Physics, and in 1977 was appointed to an ERDA Traineeship. Mr. Wall was awarded the M.S. degree in Physics in 1976. He is a member of Sigma Pi Sigma.

In April 1977 Mr. Wall was married to Laura Carruth Royston of Jonesboro, Georgia.